ABSTRACT

Title of dissertation: HIGH PURITY SINGLE PHOTONS ENTANGLED WITH BARIUM IONS FOR QUANTUM NETWORKING

Clayton Crocker, Doctor of Philosophy, 2019

Dissertation directed by: Professor Christopher Monroe
Joint Quantum Institute,
University of Maryland Department of Physics and
National Institute of Standards and Technology

Increasing the number of qubits that can be controlled in a quantum system represents an essential challenge to the field of quantum computing. Quantum networks consisting of nodes for local information processing and photonic channels to distribute entanglement between different nodes represent a promising modular approach to achieve this scaling. Trapped atomic ions are an ideal candidate for quantum network nodes, with long-lived identical qubit memories that can be locally entangled through their Coulomb interaction and remotely entangled through photonic channels. In this work I will first discuss our established toolkit for using $^{171}Yb^{+}$ and $^{138}Ba^{+}$ ions individually or together within a quantum node. Next I will show how the $^{138}Ba^{+}$ toolkit has been extended to allow for quantum operations in the $5^2D_{3/2}$ manifold. I will then demonstrate how we can generate ion-photon entanglement as a resource to connect separate nodes with a focus on some important improvements which will allow us to implement it as part of a larger network. These

improvements include first the use of separate memory ($^{171}Yb^{+}$) and photon generating ($^{138}Ba^{+}$) ions. Additionally, the use of separate atomic lines within $^{138}Ba^{+}$ for excitation and collection allows us to preserve integrity of this photonic interface by ensuring the purity of the single photons that are produced. To this end I demonstrate a single-photon source for quantum networking based on a trapped $^{138}Ba^{+}$ ion with a single photon purity of $g^2(0) = (8.1 \pm 2.3) \times 10^{-5}$ without background subtraction. Trade-offs between the photonic generation rate and the memory-photon entanglement fidelity for the case of polarization photonic qubits are also examined and optimized by tailoring the spatial mode of the collected light. These techniques should be useful in constructing larger ion-photon networks.

HIGH PURITY SINGLE PHOTONS ENTANGLED WITH BARIUM IONS FOR QUANTUM NETWORKING

by

Clayton Crocker

Dissertation submitted to the Faculty of the Graduate School of the
University of Maryland, College Park in partial fulfillment
of the requirements for the degree of
Doctor of Philosophy
2019

Advisory Committee:
Professor Christopher Monroe, Chair/Advisor
Professor Alexey Gorshkov
Professor Mohammad Hafezi
Professor Steven Rolston
Professor Ian Spielman

Dedication

To Mom and Dad

Acknowledgments

During my time here at the JQI I have had the privilege of working with many people who have been not only talented researchers but also skilled mentors who have guided me throughout my graduate work. I would like to thank Chris Monroe for being a fantastic advisor. He has provided guidance when necessary while granting the autonomy to direct the lab and grow as a researcher.

Additionally, I recognize his behind-the-scenes work to build and foster a strong sense of community within the large group. As with quantum systems, the high connectivity and strong many-body interactions with other group members has facilitated many unique dynamics. The strongest of these interactions have been within the ion-photon subgroup. When I joined the group in 2013, the other members were Susan Clark, Dave Hucul, and Volkan Inlek. Susan was tremendously helpful in teaching me some of the fundamentals of the experiment and helped kick-start my career in the lab. Dave brought to the lab an infectious aura of passion and enthusiasm for the work at hand and for life in general. As the senior graduate student on the project, he taught me a lot about both the experiment and the attitude necessary to succeed in grad school. Volkan provided the lab with a quieter diligence. His unwavering perseverance even through hard times proved invaluable, and his artistic skills brightened the group environment.

Soon, Grahame Vittorini joined the group as a post doc, bringing both a wealth of ion-trapping experience and a jovial attitude to the lab. Never afraid to speak his mind, he was constantly challenging and pushing me to become a better

researcher. After that, Ksenia Sosnova joined the lab and immediately applied her expertise in AMO theory to solve several important questions as we moved towards trapping barium. Since then she has fully embraced the experimental focus of our lab, and one piece of equipment at a time has developed a commanding grasp of our experiment's hardware and operation. After Grahame left, Marty Lichtman came aboard as the lab's post-doc. His expertise with control systems, his eagerness to engage with critical projects, and his engineering perspective towards integrated and refined systems have been essential for achieving the results presented here and should be important moving forward as well. Allison Carter has been the most recent grad student to join the group. She has quickly developed a tremendous skill at taking ownership of important projects, and seems to have inherited Volkan's resolve in persisting through adversity. Our lab has also had a number of talented undergraduate students join throughout the years, and I would like to thank Hannah Ruth and Sophie Scarano for their contributions designing and building various pieces of experimental hardware.

I have also had the opportunity to work with and learn from many other members of the Monroe group as well as the growing UMD ion trapping community. The culture of being able to ask questions to anyone in the group has been tremendously beneficial, and so I would like to thank everyone else who has been in the group with me. This list includes Jonathan Mizrahi, Chenglin Cao, Andrew Manning, Taeyoung Choi, Crystal Senko, Phil Richerme, Brian Neyenhuis, Aaron Lee, Jake Smith, Kale Johnson, Shantanu Debnath, Jason Amini, Ken Wright, Paul Hess, Kai Hudek, Steven Moses, David Wong-Campos, Caroline Figgatt, Jiehang

Zhang, Drew Risinger, Jessica Hankes, Laird Egan, Kate Collins, Wen Lin Tan, Patrick Becker, Daiwei Zhu, Antonis Kyprianidis, Harvey Kaplan, Kevin Landsman, Michael Goldman, Kristin Beck, Marko Cetina, Guido Pagano, and Norbert Linke. During my career here, the ion-trapping community at UMD has started to grow beyond the Monroe group, and so I would like to thank the other local ion-trappers who have also contributed to our community. I have specifically interacted with Qudsia Quraishi, James Siverns, John Hannegan, Edo Waks, Youngmin Martin Kim, Joe Britton, and Connor Goham.

Despite this wonderful community, grad school has been a difficult time for me. Fortunately, I have had a great deal of support from friends and family spread far and wide, who have remained close to heart. For helping me become the person I am today and filling my life with joy I would like to thank Team Kenny, and I would like to thank all of the wonderful friends with whom I have shared adventures, large or small. Finally, for their constant love and encouragement I would like to thank my family.

Table of Contents

List of Tables

List of Figures

List of Abbreviations

AOM	Acousto-Optic Modulator
APD	Avalanche Photo Diode
AWG	Arbitrary Waveform Generator
CG	Clebsch-Gordan
CZ	Cirac-Zoller
DDS	Direct Digital Synthesizer
EIT	Electromagnetically Induced Transparency
EOM	Electro-Optic Modulator
HWP	Half-Wave Plate
IR	Infrared
MS	Mølmer-Sørensen
NA	Numerical Aperture
NV	Nitrogen Vacancy
PBS	Polarizing Beam Splitter
PMT	Photo Multiplier Tube
QWP	Quarter-Wave Plate
RF	Radio Frequency
RSA	Riverst-Shamir-Adleman
UV	Ultraviolet

Chapter 1: Introduction

1.1 Quantum Computing

The field of quantum computing has received tremendous interest over the past couple of decades. In the early 1980s, Richard Feynman introduced the notion of using a quantum system to process information that would be impossible to efficiently simulate on a classical computer [1]. It was over a decade, though, before a pair of seminal works ushered in an age of immense support and activity in the field. First, in 1994, Peter Shor demonstrated an algorithm for efficiently factoring large integers [2]. This was not the first quantum algorithm presented with an exponential speedup over the best known classical counterpart [3], and, but for a historical quirk of cryptographic standards, this algorithm might have gone largely unnoticed. As it happened, though, this exact task of factoring large integers lay at the heart of breaking the common RSA encryption that was (and often still is) used to protect user data throughout the world. This result sparked both academic and governmental interest in the field, and in rapid succession, the first quantum logic gate was proposed and then demonstrated on a trapped ion system [4, 5].

Nonetheless, valid questions remained about the viability of realizing a quantum computer given the sensitivity of necessary quantum coherences to external

noise [6]. Specifically, it was noted that if a single qubit error can spoil a quantum algorithm, then the exponentially small error rates required to reliably perform even modest calculations may be unobtainable. These concerns were addressed by another result presented by Peter Shor [7] and Andrew Steane [8] which proposed a method for implementing fault-tolerant error correction on quantum bits. For the cost of redundantly encoding a single quantum bit of information in many different physical qubits, this result showed that long algorithms may be performed without the exponential sensitivity to single-qubit noise.

These results provided a concrete (if distant) motivation for developing large-scale quantum information processors and demonstrated that such a device is achievable, at least in principle. Since then, considerable effort and progress has been made in the field towards the twin goals of increasing the size of the system and increasing the fidelity of operations on that system. These two goals, however, have consistently shown an antagonistic relationship. With each new step in system size, great effort must be made to ensure that fidelities are not sacrificed. Similarly, fidelity records are typically set on small systems, and much additional effort is required before they can be applied to more qubits. For instance, today researchers on state-of-the-art quantum computers on a number of platforms are working hard to extend the successes of smaller systems of 5-7 qubits [9,10] to perform algorithms on larger processors with 10's of qubits. These larger systems threaten to perform certain calculations faster than their classical counterparts [11]. An approach to alleviate this struggle between system size and fidelity by using a modular architecture will be discussed later this chapter and provides much of the motivation for this work.

1.2 Quantum Communication

Whereas quantum computing attempts to process quantum information, quantum communication seeks to distribute quantum information over macroscopic distances, typically through a photonic link. Because they rely on the same fundamental principles and often leverage similar hardware, these two fields have developed in parallel with one another. In 1984, a decade before Shor published his algorithm which threatened to eventually shake the foundation of modern cryptography, Charles Bennett and Gilles Brassard proposed a method for using a quantum channel to securely send and receive classical information [12]. Unlike most methods for secure communications, this quantum cryptography protocol and others that followed [13] rely on the principles of quantum physics rather than on the mathematical complexity of certain tasks to guarantee protection against eavesdroppers.

Another area of interest for quantum communication is the development of quantum repeaters. Light propagating through an optical fiber suffers loss that scales exponentially with path length. Even for low-loss telecom wavelength photons, this loss becomes prohibitive for networks $\sim$ 100 km. Classical communication overcomes this by including repeater nodes at regular intervals along the path to amplify the signal. It has been shown to be impossible, however, to make a copy of an unknown quantum state [14], meaning that this kind of amplification is impossible for a quantum repeater. Instead, a quantum repeater can break the communication channel into smaller sections and verify the entanglement between each stage [15]. This reduces efficiency scaling to polynomial in channel length and in principle

allows for quantum communication over arbitrarily long distances.

Today there exist many large scale experimental implementations of quantum communication, distributing entanglement from 10's to 1000's of kilometers [16–19]. The largest of these networks require quantum repeater nodes to mitigate the exponential attenuation of photons through optical fibers. Recently, entanglement has been demonstrated between photons from a satellite at two ground-based labs 1203 km apart [20].

1.3 Quantum Networks

At the intersect of quantum computing and quantum communication is the field of quantum networking. A quantum network is comprised of two components: nodes, where quantum information is generated, stored and processed, and channels where quantum information is distributed node to node [22, 23]. Many of the quantum communication applications already discussed can utilize quantum networks. For example, quantum repeater nodes typically require memory qubits and the ability to perform local operations in order to carry out the necessary entanglement purification [24]. Thus, a quantum communication system typically is a long-distance 1-D quantum network, with nodes at the end points and the repeater locations, and with channels connecting them in a nearest-neighbor architecture (see Fig. 1.1(a)). By contrast, other applications of quantum networks such as quantum meteorology often use networks with more dense connectivity such as the graph shown in Fig. 1.1(b) [21].

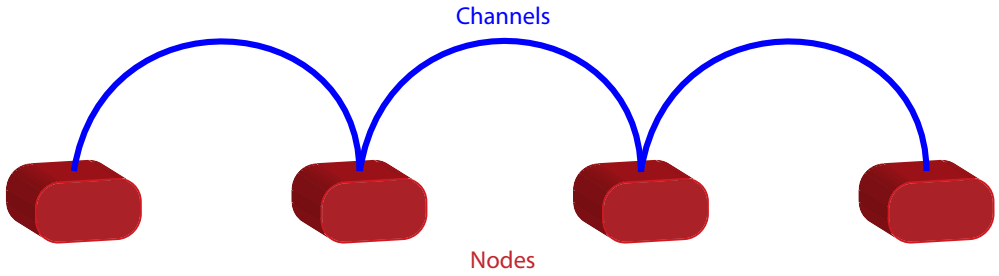

(a)

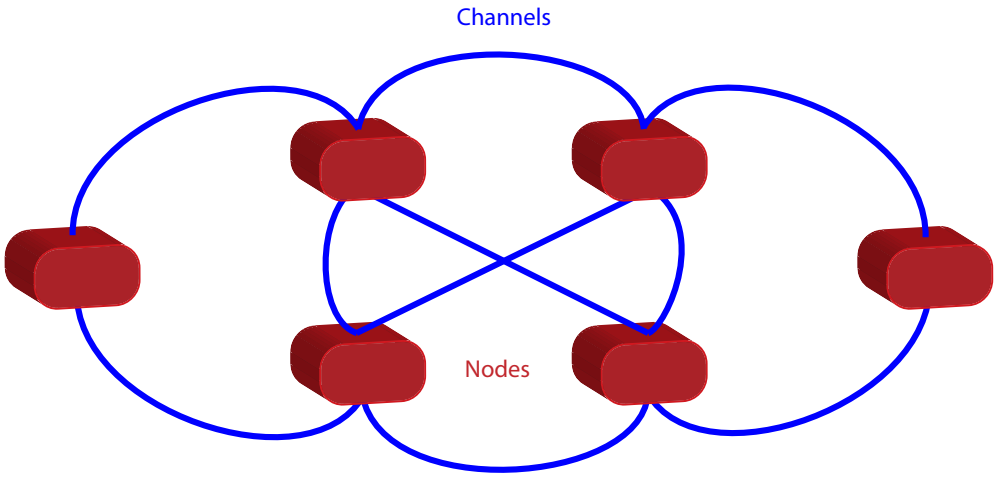

(b)

Figure 1.1: (a) Network diagram of a quantum communication network with two repeaters in the middle. Nodes of the network are shown in red and quantum channels (edges of the network) are shown in blue. (b) Quantum network with a higher connectivity. This network was proposed for quantum sensing applications [21].

Another important application of quantum networking is distributed quantum computing [25–28], which will serve as the focus for much of this dissertation. As discussed at the start of this chapter, increasing the number of qubits in a physical system without sacrificing performance is an arduous task. This difficulty suggests that a networked architecture may be key to scaling quantum processors [25]. In this approach, instead of increasing the number of qubits per system ad infinitum, one constructs a large number of modules (nodes), each with a manageable number of qubits (likely in the 50-100 range for trapped ions [29]). These modules can then be connected via photonic interfaces (channels) to effect a single, larger quantum processor. This approach has a large up-front cost in added complexity, but promises to provide a way around many of the scaling issues present in trapped ion quantum computers [30]. Later chapters will focus on ways these complexities have been addressed and on how each element of a modular trapped ion quantum network has been demonstrated and refined.

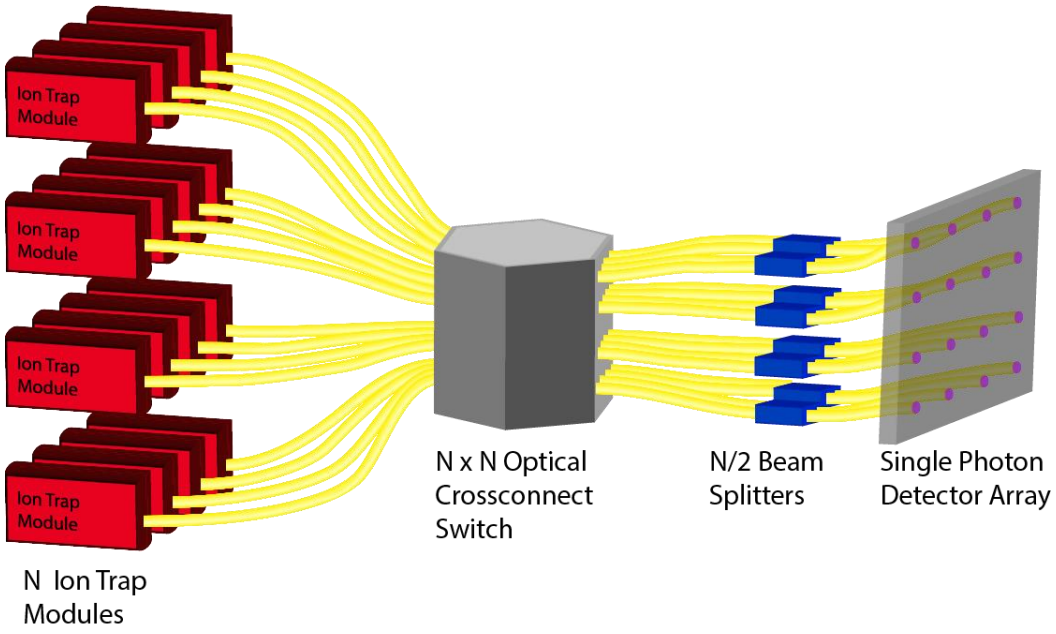

Figure 1.2: Modular quantum network for trapped ion quantum computing. Each module contains some manageable number of trapped ions and has the ability to perform local operations within the module. Each module also possesses at least one communication qubit that can be probabilistically entangled with the communication qubit in another module through a photonic link mediated by the optical fibers (yellow), beam splitters, and SPD array. For many quantum computing applications, greater connectivity can lead to improved performance [31]. It has therefore been proposed that arbitrary pairwise connectivity could be achieved between nodes by using an NxN optical cross-connect switch [30] such as the one presented in Ref. [32].

Chapter 2: Basic Ion Trapping Toolkit: Yb

Eighteen years ago, DiVincenzo proposed a set of five criteria necessary for a physical implementation of a quantum computer [33]:

1. A scalable physical system with well characterized qubits
2. The ability to initialize the state of the qubits to a simple fiducial state
3. Long relevant decoherence times, much longer than the gate operation time
4. A "universal" set of quantum gates
5. A qubit-specific measurement capability

These criteria are not meant to capture the full range of issues facing the field today, but nonetheless they serve as a useful framework for thinking about some of the basics tools required for performing quantum computing experiments. This chapter will discuss some of the basic tools used on the $^{171}Yb^{+}$ atom, framed in the context of these criteria.

2.1 The $^{171}Yb^{+}$ Atom as a Physical System

The first of Divincenzo's criteria calls for a physical system that is scalable and well characterized. While "scalable" is a common claim in the field [34–43], it is a notoriously tricky term to define. A scalable system is typically understood to

refer to a system whose required recourses, in principle, scale at most linearly with the number of qubits [44]. There is ambiguity, however, in the phrase "in principle," since it can be difficult to distinguish challenges to scalability that are fundamental from those that are simply hard. In this section I will not attempt to demonstrate that Yb ions or trapped ions in general are fundamentally scalable, except to cite a number of works on methods for scaling the ion trap quantum processor [29, 45, 46], including this thesis in its entirety.

"Well-characterized" is a much less nebulous concept, and represents one of the great strengths of the trapped-ion platform. Unlike artificial qubits such as superconducting circuits, each trapped $^{171}Yb^{+}$ ion is fundamentally identical, and thus the full set of energy levels are known and many of the required "calibrations" can be simply looked up in advance with high precision (Fig. 2.1). We use the two $m_F = 0$ hyperfine "clock" states in the ground level of $^{171}Yb^{+}$ as our qubit, defining $^2S_{1/2}\,|F = 1, m_F = 0\rangle \equiv |\Uparrow\rangle$ and $^2S_{1/2}\,|F = 0, m_F = 0\rangle \equiv |\Downarrow\rangle$. For every $^{171}Yb^{+}$ ion, splitting between these states is $12642812118.466 \pm 0.002$ Hz at zero magnetic field [47].

Moreover, precise measurements have been made on other transitions in $^{171}Yb^{+}$ [48, 49], including one of the most precise clock measurements ever performed [50]. The fact that each qubit is identical and defect-free, as well as the first order magnetic field insensitivity of the transition, also contributes to the unrivaled coherence times of trapped ions [51]. Our group has shown a coherence time of 2.5 s [52] and other groups using $^{171}Yb^{+}$ have demonstrated coherence times of over 15 minutes [47]. These timescales are much longer than modern quantum experiments,

satisfying DiVincenzo's 3rd criterion.

2.1.1 Photoionization

In addition to the general quality of the $^{171}Yb^{+}$ atom as a physical platform, the particulars of how it is trapped, cooled, and prepared for quantum operations in our lab are also important. Inside our vacuum chambers, there is a small stainless steel tube open at one end and filled with enriched ^{171}Yb which serves as an atomic source oven. The opening points towards the center of the ion trap and the oven is grounded to the chamber at one end and connected to an electrical feedthrough at the other end. A current can be run through the oven to resistively heat the Yb inside and produce a small atomic flux directed at the trapping region. The required currents vary dramatically based on the size of the oven and the amount of heat-sinking the support structure provides, but a typical value is around 3.6 A.

Once this atomic flux is established, a 399 nm beam from a CW laser is sent through the trapping region to excite neutral Yb population from the $^1S_0$ ground state to the $^1P_1$ excited state [52]. When setting the frequency of this laser, consideration must be given to the geometry of the trapping setup to account for Doppler shifts, as the angle between the atomic beam and the 399 nm beam can change the required lock frequency by ~ 1 GHz.

A 399 nm photon, however, lacks sufficient energy to excite the electron from $^1P_1$ to the continuum, so laser light from another CW source at 369 nm must also be applied in order to liberate the electron and produce an ion.

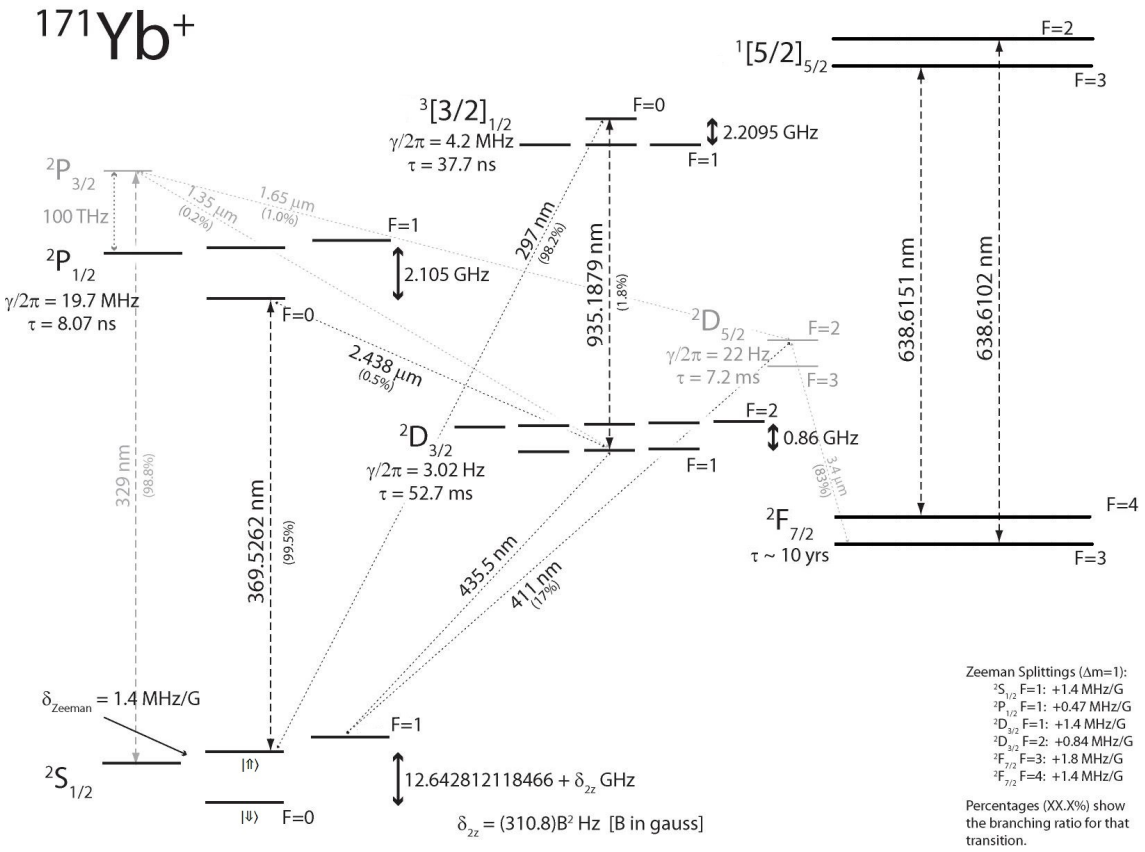

Figure 2.1: Energy level diagram for $^{171}Yb^{+}$. Levels that we directly address are shaded darker. Additional levels that we off-resonantly couple to are included in lighter shading.

2.1.2 Doppler Cooling

In order to be well localized and useful for quantum experiments, the ions must be Doppler cooled to near their ground state of motion. The principle behind Doppler cooling is to apply light that is red detuned from a given atomic transition. This causes the atom to preferentially absorb photons with momentum opposite of its own, and because the subsequent spontaneous emission is isotropic, this leads to an average net reduction in the atom's momentum per scattering event.

A short discussion of the limits of this cooling scheme will introduce some useful principles of light-matter interactions. Consider a two-level system with an energy splitting $\hbar\omega$ driven by monochromatic light of frequency ω_0. The photon scattering rate (R_{scatt}) is given by [53]:

$$R_{\text{scatt}} = \frac{\Gamma}{2}\frac{I/I_{\text{sat}}}{1 + I/I_{\text{sat}} + 4\delta^2/\Gamma^2}. \tag{2.1}$$

where $\delta = \omega - \omega_0 - kv$ is the detuning of the laser with the Doppler shift on an ion moving at velocity v taken into account, Γ is the linewidth of the transition, I is the intensity of the applied light, and I_{sat} is the saturation intensity for the transition. The saturation intensity for a given transition with resonance wavelength λ is

$$I_{\text{sat}} = \frac{\pi}{3}\frac{hc\Gamma}{\lambda^3}. \tag{2.2}$$

This is a useful parameter for many atomic physics calculations, and the saturation intensities for a few of our common transitions in the lab are listed in Table 2.1.

Because each photon carries momentum $\hbar k$, there is a force imparted on the

Species	Transition	Resonance Frequency (THz)	I_{sat} (mW/cm^2)
^{171}Yb	$^1S_0 \rightarrow\ ^1P_1$	751.52639	60
^{171}Yb$^+$	$^2S_{1/2} \rightarrow\ ^2P_{1/2}$	811.2890	51.0
	$^2S_{1/2} \rightarrow\ ^2P_{3/2}$	911.1361	95.1
	$^2D_{3/2} \rightarrow\ ^2[3/2]_{1/2}$	320.5692	37.5
^{138}Ba	$^1S_0 \rightarrow\ ^3D_1^o$	725.25890	0.44
^{138}Ba$^+$	$^2S_{1/2} \rightarrow\ ^2P_{1/2}$	607.42630	16.4
	$^2S_{1/2} \rightarrow\ ^2P_{3/2}$	658.11648	35.7
	$^2D_{3/2} \rightarrow\ ^2P_{1/2}$	461.31192	28.9

Table 2.1: Resonance frequencies and saturation intensities for common transitions in our lab. Yb data from Ref. [52], Ba data from Ref. [54].

ion $F_s = \hbar k R_{scatt}$. For small velocities, this force can be approximated as:

$$F_s(\delta) = F_s(\omega - \omega_0 - kv) \approx F_s(\omega - \omega_0) - kv\frac{\partial F}{\partial \omega} \tag{2.3}$$

The first term on the right, $F_s(\omega - \omega_0) \equiv F_0$, is constant in v and can be considered as simply applying a small offset of the ion position in the trapping potential. If $\frac{\partial F}{\partial \omega}$ is positive, the second term acts as a damping force. Taking the derivative of equation 2.1 gives $F_s = F_0 - \alpha v$ where

$$\alpha = \hbar k^2 \frac{I}{I_{\text{sat}}} \frac{-4\delta/\Gamma}{[1 + I/I_{sat} + (2\delta/\Gamma)^2]^2} \tag{2.4}$$

is the damping coefficient. In order to cool the ions rather than heat them, this value must be positive, meaning that the detuning must be negative, i.e. we must be red detuned. The damping coefficient is maximized at $\delta = -\Gamma/2$ giving a value of $\alpha_{\max} = \hbar k^2/4$.

At low temperatures, this damping force is primarily opposed by heating from the random walk of the recoil force of spontaneous emissions. We can define the energy per recoil event as $E_r = \hbar\omega_r$. Noting that each spontaneous emission event involves two random kicks (one for absorption and one for emission) this gives a heating rate of $2\hbar\omega_r R_{\text{scatt}}$ [55]. At equilibrium, this is equal to the cooling rate, $-\alpha v^2$, and so plugging in equation 2.1 gives the temperature as

$$k_B T = \frac{\hbar\Gamma}{4} \frac{1 + (2\delta/\Gamma)}{-2\delta/\Gamma}. \tag{2.5}$$

This is again minimized at $\delta = -\Gamma/2$, producing a Doppler cooling temperature

limit of $T_D = \frac{\hbar\Gamma}{2k_B}$. For the $^2S_{1/2} \leftrightarrow ^2 P_{1/2}$ transition in Yb^+, $\Gamma = 2\pi \times 19.6$ MHz, giving a Doppler limited temperature of 470 μK.

We implement Doppler cooling on $^{171}Yb^+$ using a 369 nm diode laser tuned red of the transition from the F=1 manifold of the $^2S_{1/2}$ level ($|\Uparrow\rangle$) to the F=0 manifold of the $^2P_{1/2}$ level as in Fig. 2.2(a). Off resonant pumping to the $^2P_{1/2}$ F=1 manifold can result in decays to $|\Downarrow\rangle$. The primary cooling beam is 14.7 GHz detuned from any transitions from this state, meaning that the ion goes dark once population ends up here. Therefore, 14.7 GHz sidebands are added to our cooling beam to pump the ion out of this dark state and back into the cooling cycle (Fig. 2.2(b)). These sidebands are actually the second sideband of a resonant EOM driven at 7.37 GHz.

The ion can also decay from the cooling cycle into the $^2D_{3/2}$ F=1 level. To avoid population trapping in this state, a CW laser at 935nm is applied to drive the $^2D_{3/2} \rightarrow {}^2[3/2]_{1/2}$ transition. Population in the $^2[3/2]_{1/2}$ level quickly decays back to the cooling cycle. Additionally, the same off-resonant pumping to the $^2P_{1/2}$ F=1 manifold that populates the $|\Downarrow\rangle$ state can also decay to the $^2D_{3/2}$ F=2 level. This requires that we apply 3.07 GHz sidebands to this 935 nm light using an in-fiber EOM.

Finally, there exists a low-lying $^2F_{7/2}$ state in $^{171}Yb^+$ with a lifetime of 5.4 years. Though there are no dipole allowed transitions from our cooling cycle into this state, population is occasionally driven there by either collisions with background gas or decays from population off-resonantly driven to the $^2P_{3/2}$ level and then decaying there via $^2D_{5/2}$. This F-state population is returned to the cooling cycle using a 638 nm CW laser which excites the atom to the $^1[5/2]_{5/2}$ level where it can

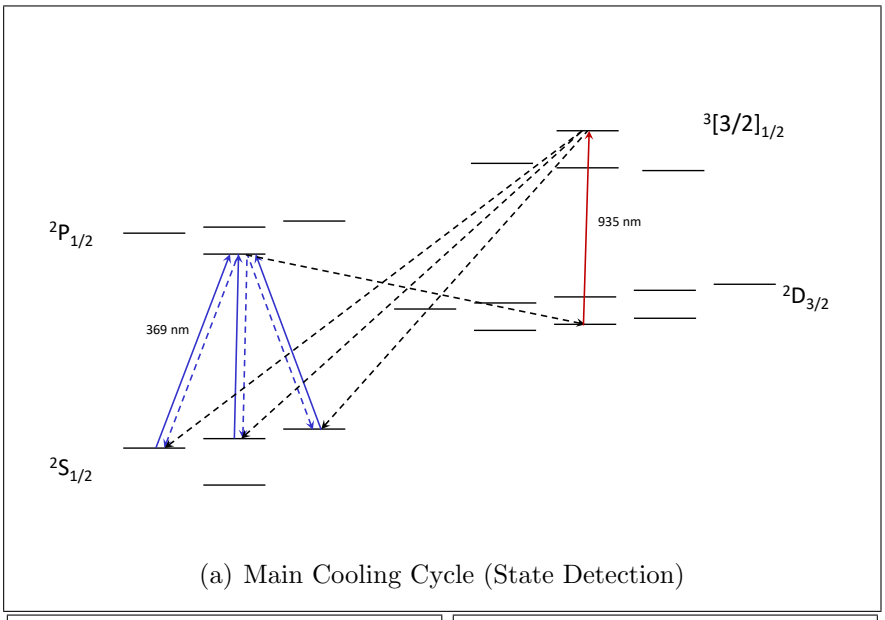

(a) Main Cooling Cycle (State Detection)

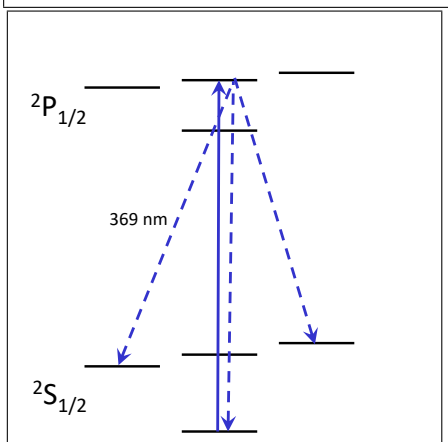

(b) Cooling Sidebands

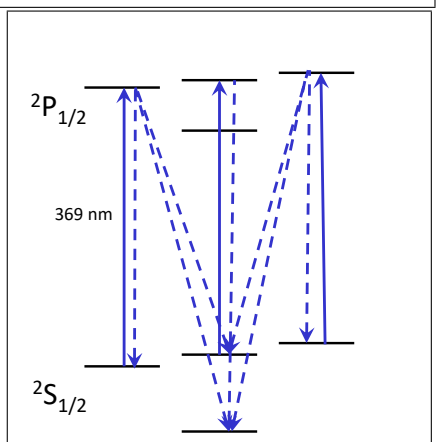

(c) Pumping Sidebands

Figure 2.2: (a) Closed cooling cycle allows no excitations or decays to take ion out of the cycle. Because this cycle includes the $|\Uparrow\rangle$ state and not the $|\Downarrow\rangle$ state, application of this light without any sidebands can serve as state detection as well. (b) 14.7 GHz cooling sidebands are added to the light shown in (a) when Doppler cooling the ion in order to return light from the $|\Downarrow\rangle$ state to the cooling cycle. (c) 2.1 GHz pumping sidebands are added to the light shown in (a) in order to initialize the light in the $|\Downarrow\rangle$ state.

decay back to the $^2D_{3/2}$ manifold [49]. Because F-state events are rare ($\sim$ 1/hour) we sweep the frequency of this laser to span the hyperfine states rather than apply sidebands to the light.

2.2 State Initialization and Readout

In this section, I will discuss how we realize DiVincenzo's 2nd and 5th criteria in Yb ions. Though this may seem an odd ordering, the hardware used for these implementations are very similar to each other and to the Doppler cooling just discussed. State initialization is performed by switching off the 7.37 GHz EOM on the 369 nm light and turning on a 2.1 GHz EOM. This drives population from $|\Uparrow\rangle$ to the $^2P_{3/2}$ F=1 manifold, where it can decay back to the $|\Downarrow\rangle$ state and become trapped as in Fig. 2.2(c). This efficiently pumps the ion into the $|\Downarrow\rangle$ state in ~ 1 μs.

For state readout, the 369 nm light can be applied to the ion without any sidebands. If the ion is in $|\Uparrow\rangle$, this will drive a cycling transition on $|\Uparrow\rangle \leftrightarrow {}^2P_{1/2}\,|F=0, m_F=0\rangle$. If the ion is in the "dark" $|\Downarrow\rangle$ state, however, it will be trapped and scatter no light. This allows for efficient state-detection by discrimination of the number of photons collected on a photomultiplier tube (PMT) during a detection cycle. For optimal detection fidelities, we must detect long enough that the Poisson distributions of photon counts from bright and dark states have minimal overlap, but not so long that off-resonant pumping mixes the bright and dark states. The optimal detection time will vary based on background count rates and the size of the imaging objective. For our current setup this is about 250 μs.

2.3 Single Qubit Rotations

DiVincenzo's fourth criterion is by far the most complex to implement in $^{171}Yb^{+}$. In fact, in most quantum computing platforms, it is gate errors rather than coherence times, initialization, or readout that limit the complexity of computations that can be performed. In this section, I will discuss ways we can implement single qubit rotations, which constitute only one part of a universal gate set. Later this chapter I will discuss how we complete our universal gate set with a two-qubit entangling gate.

2.3.1 Microwave Rotations

One way to perform qubit rotations is to apply resonant 12.6 GHz microwave radiation directly to the ions to drive coherent dipole transitions between hyperfine levels. This signal is generated by mixing a 12.450 GHz clock output with a signal near 200 MHz from a direct digital synthesizer (DDS). This mixed signal is then put through a filter to ensure that only the sum frequency component passes. It is then amplified and applied to a microwave horn located just outside one of our vacuum windows. Transitions from $|\Downarrow\rangle$ to different Zeeman sub-levels of the $^2S_{1/2}$ F=1 level can be frequency selected by changing the output frequency of the DDS.

When setting up the microwave horn, it is important to check different Zeeman transitions to ensure the microwave intensity and polarization at the ion location can efficiently drive the different lines. If one of the transitions is too slow, physically moving or rotating the horn may be required.

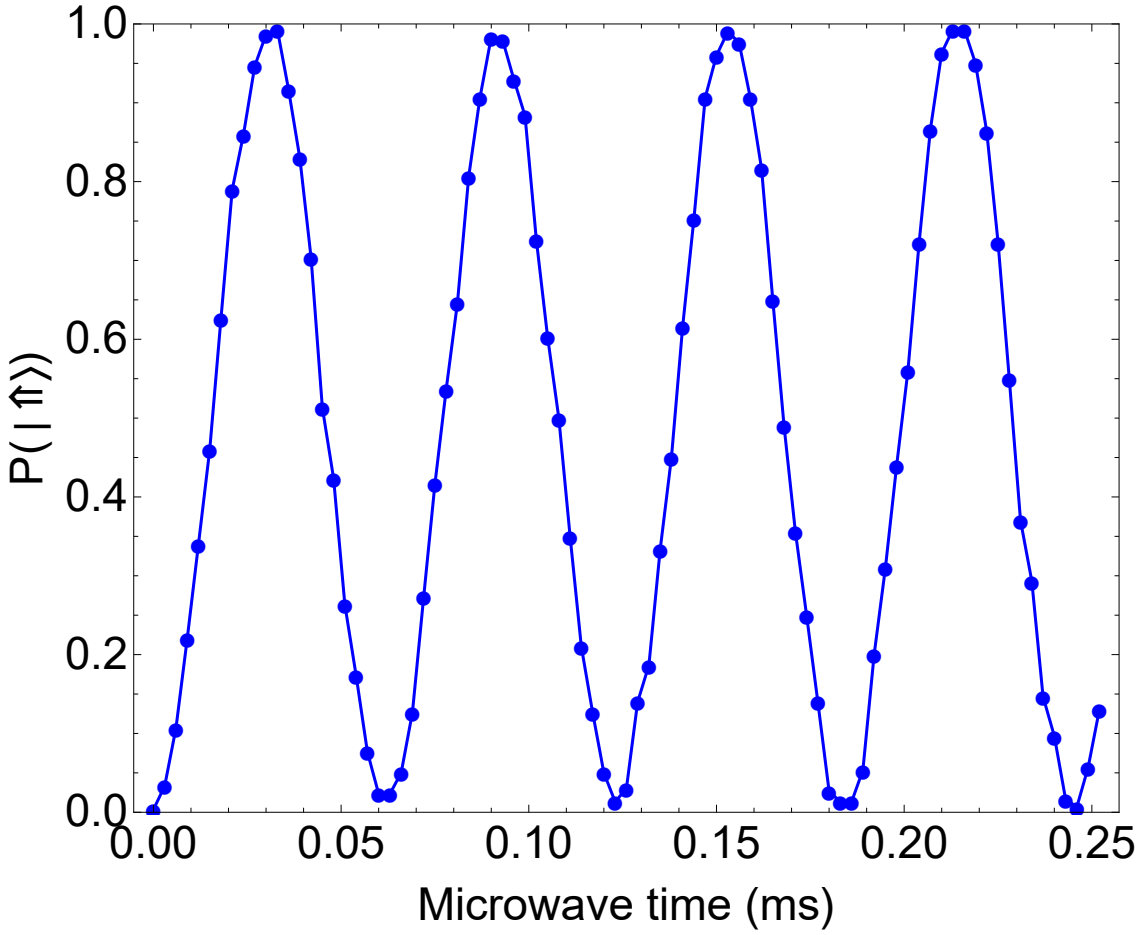

Figure 2.3: Microwave Rotations on a single $^{171}Yb^{+}$ ion. Probability of finding the ion in the $|\Uparrow\rangle$ is plotted as a function of applied microwave time.

2.3.2 Raman Beams

In addition to applying the 12.6 GHz radiation directly to the atoms in the form of microwaves, coherent rotations can also be driven by applying this frequency as a beatnote on a pair of 355 nm beams to drive Raman rotations. The 355 nm light comes from a mode-locked, frequency tripled Nd:YVO_4 laser. Common AO frequency shifters tend to operate at <1 GHz, so in order to span the 12.6 GHz frequency splitting, we utilize the large bandwidth of this laser. In frequency space, a mode-locked laser is a frequency comb, with comb teeth separated by the repetition rate of the laser ν_r [56]. We can impart a relative frequency offset between the two beams by putting them through AOMs with bandwidth of at least $\nu_r/2$, allowing us to achieve arbitrary frequency splittings between separate comb teeth up to the bandwith of the laser. For Nd:YVO_4, this bandwidth is hundreds of GHz [57], easily allowing us to span the hyperfine structure of Yb. If we apply a relative frequency shift of δ_0 to the two beams, then, we can drive carrier Raman transitions if $\delta_a + n\nu_r \equiv \delta_n = \nu_{HF}$ (see Fig. 2.4(a)) where n is some integer and ν_{HF} is the hyperfine energy splitting. For our laser, $\nu_r \approx 80$ MHz, so typically n=158.

2.3.3 Beatnote Lock

There is no active stabilization on the repetition rate of this laser, so it is susceptible to noise from drifts in cavity length. Unfortunately, since the beat note that we use is equal to $\delta_a + n\nu_r$, this noise is amplified by a factor of n=158, making some form of beat note locking necessary [58]. To implement this, first a

small portion of the light from the laser is picked off and measured on an Aplhalas UPD-30-VSG-P fast photodiode. The photodiode puts out a signal at ν_r and its harmonics, and it is important that the bandwidth of the photodiode be at least 13 GHz so that the 158th harmonic at 12.65 GHz is produced. All other harmonics are removed by a narrow filter and then this signal is mixed with our 12.450 GHz clock output. The difference frequency from this mixer is then mixed again with the output of an HP 8640B signal generator at near 200 MHz. This output is near DC and is used as the error signal on a PI loop that feeds back onto the frequency modulation port of the 8640B. This $\sim$ 200 MHz signal from the 8640B is also applied to the AOM for one of the 355nm beams (AOM 1 in figure 2.4(b)).

This circuit locks the beatnote between the un-shifted beam and the beam shifted by AOM1 to exactly the clock frequency (12.450000 GHz). This ensures that δ_n is constant throughout our experiments, independent of changes in ν_r.

2.3.4 Raman Rotations

The 355 nm beams couple the ground state levels to both the $^2P_{1/2}$ and $^2P_{3/2}$ manifolds, and the interplay between these levels is important to consider when finding the rate of the transitions [55]. Much of the important physics of this interaction, though, can be obtained by considering a simplified example where the two ground levels $|\Uparrow\rangle$ and $|\Downarrow\rangle$ only couple to a single excited state $|e\rangle$ in a Λ configuration where $|e\rangle$ is seperated from $|\Downarrow\rangle$ by a frequency of ω_e. Additionally, the mode-locked laser behaves as two CW lasers driving these transitions [59] with frequencies ω_1

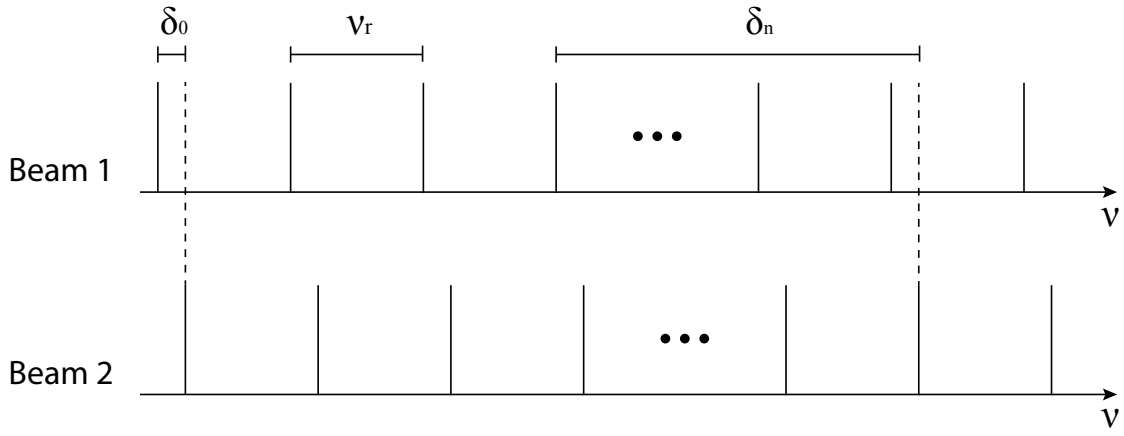

(a)

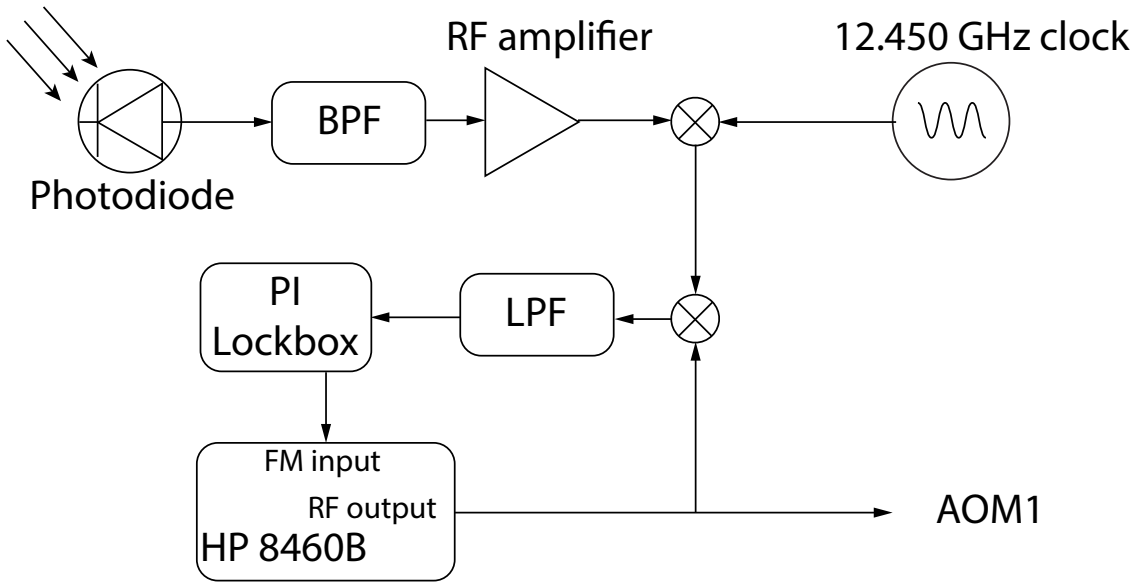

(b)

Figure 2.4: (a) Beatnote between two 355 nm beams used to drive carrier Raman transitions in $^{171}Yb^{+}$ (b) Schematic of the circuit used to lock the beatnote.

and ω_2 and a frequency difference $\omega_1 - \omega_2 = \delta_n = \delta_\omega + \omega_{HF}$. In a frame rotating at ω_1 and setting $\hbar = 1$, the Hamiltonian of this system can be written as

$$H_I = \Omega_1 \left|e\right\rangle \left\langle\Downarrow\right| + \Omega_1^* \left|\Downarrow\right\rangle \left\langle e\right| + \Omega_2 \left|e\right\rangle \left\langle\Uparrow\right| + \Omega_2^* \left|\Uparrow\right\rangle \left\langle e\right| + \Delta_1 \left|e\right\rangle \left\langle e\right| \tag{2.6}$$

where $\Delta = \omega_1 - \omega_e$, and Ω_1, Ω_2 are the one-photon Rabi frequencies for the transitions $|\Downarrow\rangle \leftrightarrow |e\rangle$ and $|\Uparrow\rangle \leftrightarrow |e\rangle$ respectively. This leads to the following equations of motion for the population amplitudes:

$$\dot{c}_\Downarrow = i\Omega_1^* c_e \tag{2.7}$$

$$\dot{c}_\Uparrow = i\delta_n c_\Uparrow + i\Omega_2^* c_e \tag{2.8}$$

$$\dot{c}_e = i\Delta c_e + i\Omega_1 c_\Downarrow + i\Omega_2 c_\Uparrow. \tag{2.9}$$

If we assume $\delta\omega \ll \Delta$ and $\Delta \gg \gamma_e$ where γ_e is the excited state decay rate, then we can adiabatically eliminate the excited state population $c_e = \frac{-1}{\Delta}(\Omega_1 c_\Downarrow + \Omega_2 c_\Uparrow)$, and the equations of motion become

$$\dot{c}_\Downarrow = i\frac{|\Omega_1|^2}{\Delta} c_\Downarrow - i\frac{\Omega_1^* \Omega_2}{\Delta} c_\Uparrow \tag{2.10}$$

$$\dot{c}_\Downarrow = i(\delta_\omega - \frac{|\Omega_2|^2}{\Delta}) c_\Uparrow - i\frac{\Omega_1^* \Omega_2}{\Delta} c_\Downarrow. \tag{2.11}$$

Thus the system evolves between $|\Downarrow\rangle \leftrightarrow |\Uparrow\rangle$ exactly as a driven 2-level system with a Rabi frequency

$$\Omega_R = -\Omega_1 \Omega_2^* / \Delta. \tag{2.12}$$

If we take into account the phase and momentum components of the driving fields, this system is governed by the Hamiltonian [60]:

$$H_I = \frac{1}{2}\left(\Omega_R e^{-i\Delta\mathbf{k}\cdot\mathbf{r}-\delta_\omega t-\Delta\phi} \left|\Uparrow\right\rangle \left\langle\Downarrow\right| + \text{h.c.}\right) \tag{2.13}$$

where $\Delta\phi$ is the phase difference between the two driving fields and $\Delta\mathbf{k}$ is the difference in the momentum vectors for the two separate Raman beams, arising from the fact that a photon is absorbed from one arm and emitted into the other arm.

2.4 Addressing Ion Motion

A single trapped ion's motion is governed by the harmonic trapping (pseudo)potential [61], and when there are multiple ions in a single trapping potential, they are coupled to each other via Coulomb repulsion. For small deviations from equilibrium, this system behaves like a system of coupled harmonic oscillators and produces a series of collective eigenmodes of motion [62]. All of our local, multi-qubit gates rely on coupling the atom's spins through this shared degree of freedom of their motional modes. Though microwave 12.6 GHz photons lack sufficient momentum to effectively address these motional modes [55], by aligning our Raman beam such that their $\Delta\mathbf{k}$ vector has a projection along one of the motional modes, we can drive spin flips in the atom while also adding or subtracting vibrational quanta from this motional mode. These transitions are known as blue and red vibrational sidebands respectively (see Fig. 2.5).

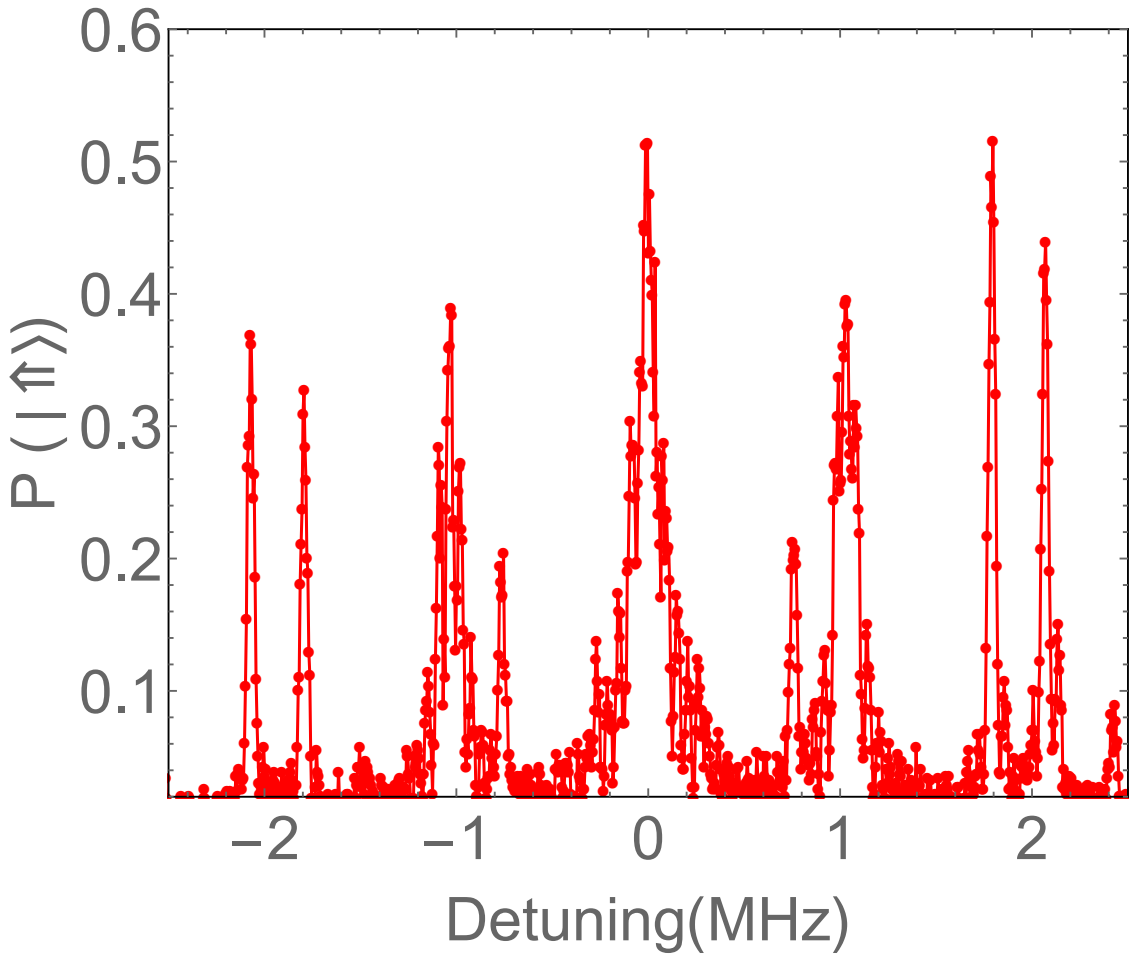

Figure 2.5: Raman frequency scan on two-ion chain with a non-copropogating beam geometry. Here we plot the probability of finding an ion in the $|\Uparrow\rangle$ state as a function of detuning from the hyperfine carrier transition. The beams are aligned so that δK is in the axial direction, so in addition to the carrier at $\delta = 0$, strong blue and red vibrational sidebands are present at $\delta\omega = \pm 0.85$ MHz for the COM mode and $\delta\omega = \pm 1.05$ MHz for the tilt mode. Second order sidebands are also visible at twice these frequencies.

First we will consider the case of addressing the motion of a single atom. By setting the detuning $\delta_n = \omega_{HF} - \omega_m$ where ω_{HF} is the qubit splitting and ω_m is the frequency of one of the trap modes, we produce a red sideband transition. The Hamiltonian for this interaction is a modified version of Equation 2.13 in the interaction picture that accounts for the changing phonon number [63]

$$H_I^{RSB} = \Omega_R \cdot \exp(i[\eta(ae^{-i\omega_m t} + a^\dagger e^{i\omega_m t}) - \delta_\omega t + \Delta\phi]) + h.c. \tag{2.14}$$

Here, a and $a^\dagger$ are the phonon annihilation and creation operators for the mode being addressed.

$$\eta = \Delta k \sqrt{\frac{\hbar}{2m\omega_m}} \tag{2.15}$$

is known as the Lamb-Dicke parameter. This important parameter quantifies the coupling between the atom's spin and motional degrees of freedom, and can also be thought of as representing the spatial extent of the vibrational mode relative to the wavelength of the driving light. From this perspective, Equation 2.15 can also be written as $\eta = \Delta k x_0$ where $x_0 = \sqrt{\frac{\hbar}{2m\omega_m}}$ is the RMS radius of the ion in the ground state of a harmonic oscillator of frequency ω_m.

With this interpretation of the Lamb-Dicke parameter in mind, one can see that if η is large, then the atom's spatial extent causes it to sample over the phase of the driving field. If the spatial density matrix is in a thermal distribution, this leads to decoherence. To avoid this, we impose the condition that we operate in the Lamb-Dicke regime: $\eta\sqrt{2\overline{n}+1} \ll 1$ where $\overline{n}$ is the average vibrational occupation

mode of the atom. In this regime, equation 2.14 can be expanded to the first power in η to give [63]

$$H_I^{RSB} = \eta\Omega_R(\sigma_+ a e^{i\Delta\phi} + \sigma_- a^\dagger e^{-i\Delta\phi}). \tag{2.16}$$

where $\hat{\sigma}_+$ is the spin raising operator on the ion. Likewise, the blue sideband Hamiltonian can be written as

$$H_I^{BSB} = \eta\Omega_R(\sigma_+ a^\dagger e^{i\Delta\phi} + \sigma_- a e^{-i\Delta\phi}). \tag{2.17}$$

2.5 Mølmer Sørensen Interaction

In this section, I will give a brief discussion on how we can address these red and blue sidebands to drive Mølmer-Sørensen gates on trapped Yb ions. For a more detailed derivation, see references [59, 60, 63, 64]. The Mølmer-Sørensen interaction is produced by simultaneously applying red and blue sidebands of Raman light with symmetric detunings of $-\delta$ and δ from the motional mode. From Eqns. 2.16 and 2.17, this produces the Hamiltonian [65]:

$$\begin{aligned} H_{MS} &= \eta\Omega_R\sigma_+(a e^{-i(\delta t-\phi_r)} + a^\dagger e^{i(\delta t+\phi_b)}) + \text{h.c.} \\ &= \eta\Omega_R(\sigma_+ e^{i\phi_S} - \sigma_- e^{-i\phi_S})(a e^{i\phi_M} e^{-i\delta t} + a^\dagger e^{-i\phi_M} e^{i\delta t}) \end{aligned} \tag{2.18}$$

Here ϕ_r, ϕ_b are the relative phases for the red, blue sideband beams. $\phi_S = (\phi_r + \phi_b)/2$ is the spin phase and $\phi_M = (\phi_r - \phi_b)/2$ is the motional phase. When this interaction is applied to two ions in a single trapping potential, it is useful to think about the

evolution of the system in terms of the available transition paths [66]. Consider a pair of ions both prepared in the spin state $|\Downarrow\rangle$ with a shared oscillator mode of phonon number n. The state of the system can be written as $|\Downarrow\Downarrow\, n\rangle$. There are four paths for exciting both spins $|\Downarrow\Downarrow, n\rangle \leftrightarrow |\Uparrow\Uparrow\, n\rangle$: two with a red sideband followed by a blue sideband and two with a blue sideband followed by a red sideband. Because of the symmetric detunings, each of these paths has a total energy $\hbar\omega_m$, meaning that they are all resonant. There are, however, no resonant paths for single spin excitations (see figure 2.6).

If δ is larger than Ω_R, this behaves as a Raman system, allowing us to adiabatically eliminate population from the single spin excitation states. From Eqn. 2.12 we can find the effective Rabi frequencies for the two paths. First we will look at the path where the red sideband acts on $|\Downarrow\Downarrow, n\rangle$ [67]

$$\begin{aligned}\Omega_{path1,2} &= \frac{\Omega_{|\Downarrow\Downarrow,n\rangle\rightarrow|\Downarrow\Uparrow,n-1\rangle}\Omega_{|\Downarrow\Uparrow,n-1\rangle\rightarrow|\Uparrow\Uparrow,n\rangle}}{-4\delta} \\ &= \frac{(\eta\Omega_R\sqrt{n})(\eta\Omega_R\sqrt{n})}{-4\delta} \\ &= -n\frac{(\eta\Omega_R)^2}{4\delta}\end{aligned} \tag{2.19}$$

The n dependence in this equation comes from the creation and annihilation operators from the sideband Hamiltonians in Eqns. 2.16 and 2.17 acting on the vibrational mode: $a\,|n\rangle = \sqrt{n}\,|n-1\rangle$ and $a^\dagger\,|n-1\rangle = \sqrt{n}\,|n\rangle$. Obviously the $|\Downarrow\Downarrow, n\rangle \rightarrow |\Uparrow\Downarrow, n-1\rangle$ path behaves the same, so next we can find the rate for the paths where the blue sideband acts on $|\Downarrow\Downarrow, n\rangle$.

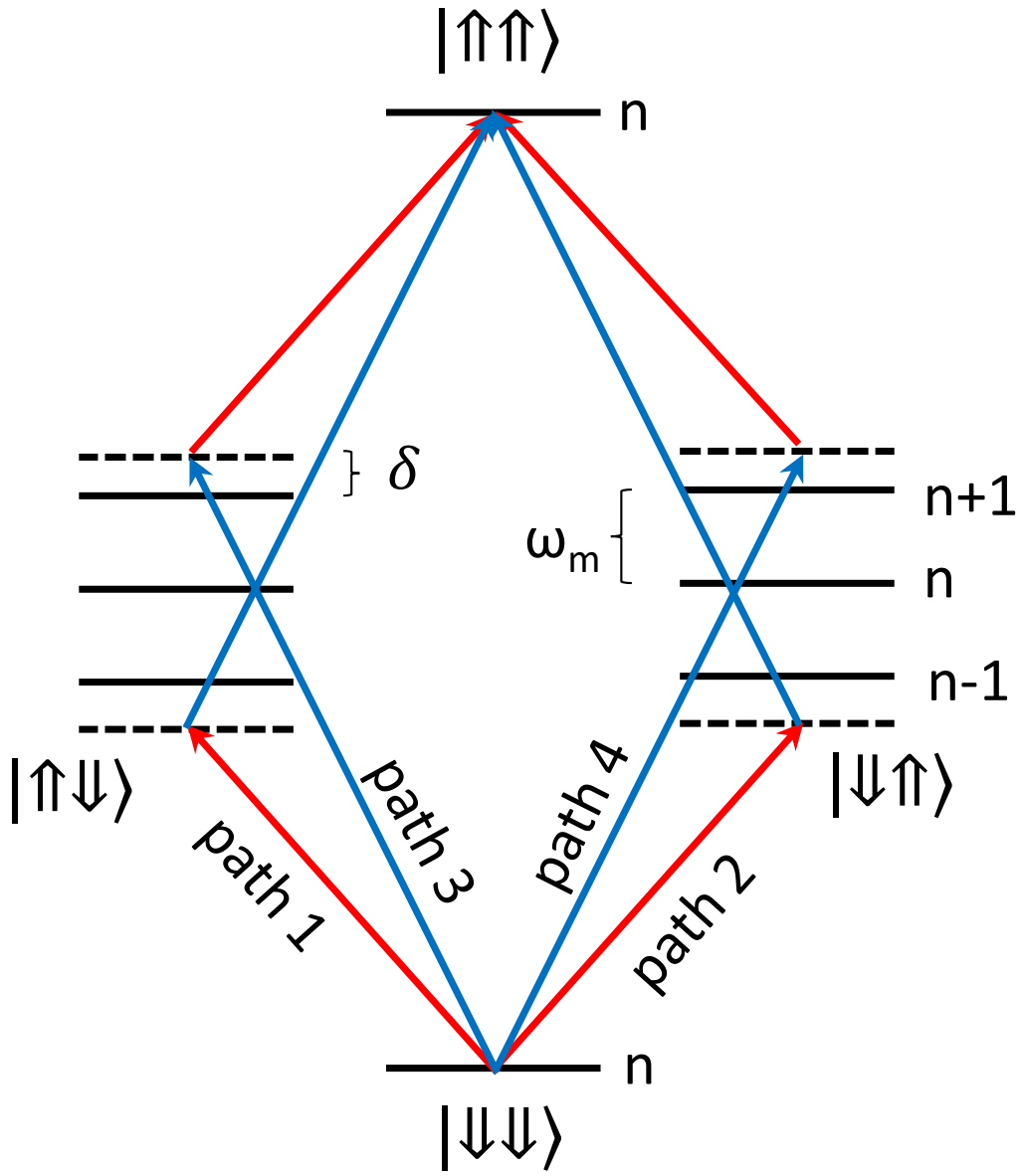

Figure 2.6: Resonant paths for two spin flips in MS interaction. Red and blue sidebands are both detuned by δ giving four resonant paths to excite both spins. Because there are no resonant paths for exciting a single spin and $\delta > \Omega_R$ we do not drive population into the intermediate $n = \pm 1$ states in the middle of the figure, and population is driven on $|\Downarrow\Downarrow, n\rangle \leftrightarrow |\Uparrow\Uparrow, n\rangle$. The rate of this transition is determined by the interference between the four paths.

$$\begin{aligned}\Omega_{path3,4} &= \frac{\Omega_{|\Downarrow\Downarrow,n\rangle\rightarrow|\Downarrow\Uparrow,n+1\rangle}\Omega_{|\Downarrow\Uparrow,n+1\rangle\rightarrow|\Uparrow\Uparrow,n\rangle}}{4\delta} \\ &= \frac{\eta\Omega_R\sqrt{n+1})(\eta\Omega_R\sqrt{n+1})}{4\delta} \\ &= (n+1)\frac{(\eta\Omega_R)^2}{4\delta}\end{aligned} \tag{2.20}$$

Likewise, the $|\Downarrow\Downarrow, n\rangle \rightarrow |\Uparrow\Downarrow, n+1\rangle$ path is identical.

The total transition rate comes from the sum over these four transition paths:

$$\Omega_{MS} = -n\frac{(\eta\Omega_R)^2}{2\delta} + (n+1)\frac{(\eta\Omega_R)^2}{2\delta} = \frac{(\eta\Omega_R)^2}{2\delta}. \tag{2.21}$$

The "miracle" [66] of the MS interaction is shown in Eqn. 2.21. Given that we go slowly enough as to not drive the single spin flip operations, the effective Rabi rate is independent of n. This means that the spin states can evolve independently from the motional state, and the gate does not rely on ground-state cooling. Population in the $|\Downarrow\Uparrow\rangle$ and $|\Uparrow\Downarrow\rangle$ states undergo a similar interaction, and the evolution of the system can be described by [64]:

$$\begin{aligned}|\Downarrow\Downarrow\rangle &\rightarrow \cos(\Omega_{MS}t/2)\,|\Downarrow\Downarrow\rangle + i\sin(\Omega_{MS}t/2)\,|\Uparrow\Uparrow\rangle \\ |\Uparrow\Uparrow\rangle &\rightarrow \cos(\Omega_{MS}t/2)\,|\Uparrow\Uparrow\rangle + i\sin(\Omega_{MS}t/2)\,|\Downarrow\Downarrow\rangle \\ |\Downarrow\Uparrow\rangle &\rightarrow \cos(\Omega_{MS}t/2)\,|\Downarrow\Uparrow\rangle - i\sin(\Omega_{MS}t/2)\,|\Uparrow\Downarrow\rangle \\ |\Uparrow\Downarrow\rangle &\rightarrow \cos(\Omega_{MS}t/2)\,|\Uparrow\Downarrow\rangle - i\sin(\Omega_{MS}t/2)\,|\Downarrow\Uparrow\rangle\end{aligned} \tag{2.22}$$

By choosing $t = \pi/\Omega_{MS}$, we can evolve from a basis state to a maximally entangled Bell state. This interaction serves as an entangling 2-qubit gate, completing our universal set of gates and satisfying the last of DiVincenzo's criteria.

Chapter 3: Networking Experiments with $^{171}Yb^{+}$

As discussed in Chapter 1, the creation of quantum networks of trapped ions and emitted photons is of great interest for quantum meteorology [68,69], quantum communication [70,71], and quantum computing [30] applications. As discussed in Chapter 2, trapped $^{171}Yb^{+}$ ions serve as excellent qubits and are ideal memories for the nodes of these quantum networks. Optical photons can travel macroscopic distances through fibers, are compatible with room temperature operation, and possess a number of degrees of freedom that can carry quantum information, making them a natural candidate for channels in a quantum network [72–76].

3.1 Ion-Photon Entanglement

Foundational to an ion-photon network architecture is the ability to generate entanglement between the spin state of an ion and the state of an emitted photon. There are several methods for generating this ion-photon entanglement. In this section, I will give a brief overview of many of these methods and an in-depth discussion of the methods used in this work. Where necessary, I will also discuss how this ion-photon entanglement is used to generate ion-ion entanglement, but a full explanation of how that is done in our experiments will be given in the next

section.

All of these methods require an energy scheme with a short-lived excited state $|e\rangle$ with decays to one or both of the ground-state qubit levels $|\downarrow\rangle$ and $|\uparrow\rangle$. The emitted photon can carry angular momentum of $\Delta m_Z = +1, 0, \text{or } -1$ quanta, and we will refer to these as σ^+, π, and σ^- decays respectively.

3.1.1 Photon Number Entanglement

The first protocol for generating remote entanglement in an ion-photon system is the single photon detection scheme, which uses weak entanglement between the atom's spin state and the photon number state [77]. In this protocol, the ion is first prepared in the $|\downarrow\rangle$ state. It is then weakly excited to $|e\rangle$ with probability $P_e \ll 1$. After a decay the atom-spin, photon-number state is $|\downarrow 0\rangle + \sqrt{P_e}\,|\psi_d\ 1\rangle$ where ψ_d is the state of the atom after a decay, and is in general a superposition of $|\downarrow\rangle$ and $|\uparrow\rangle$ determined by the Clebsch-Gordan coefficients.

This state exhibits only very weak entanglement, but the power of this protocol comes from its ability to probabilistically turn weak ion-photon entanglement into strong remote ion-ion entanglement, heralded by detection of a single photon. This is achieved by simultaneously exciting two atoms and collecting their decay photons. First, the polarization corresponding to the decays back to the $|0\rangle$ state must be filtered out (see Fig. 3.1(a)), producing the state

$$(|\downarrow 0\rangle + \sqrt{\epsilon}\,|\uparrow 1\rangle) \otimes (|\downarrow 0\rangle + \sqrt{\epsilon}\,|\uparrow 1\rangle) = |\downarrow\downarrow 00\rangle + \sqrt{\epsilon}\,|\downarrow\uparrow 01\rangle + \sqrt{\epsilon}\,|\uparrow\downarrow 10\rangle + \epsilon\,|\uparrow\uparrow 11\rangle \tag{3.1}$$

where $\epsilon \leq P_e$ accounts for the probability of a decay to the $|\uparrow\rangle$ state.

Next, photons from the two atoms must be combined on a beamsplitter to erase the information about which path they came from. A more quantitative description of the action of the beamsplitter on single photon states will be given in the next section. Detection of a single photon after the beamsplitter produces the state $|\uparrow\downarrow\rangle + e^{i\phi_p}\,|\downarrow\uparrow\rangle + \sqrt{\epsilon}e^{i\phi_2}\,|\uparrow\uparrow\rangle$ where ϕ_p is determined by the optical path length difference from the two atoms to the detector. For sufficiently small P_e, $\sqrt{\epsilon}$ can be neglected and this state approaches maximal entanglement, but since P_e also determines the entanglement generation rate, this protocol forces a trade-off between experimental rate and fidelity. Additionally, because the phase of the resultant state depends on the optical path lengths, this protocol requires that these paths be interferometrically stabilized during the experiment. Moreover, any recoil from the decay can betray which atom it was that emitted the photon and spoil the entanglement, meaning that the atoms need to be cooled to well within the Lamb-Dicke limit [78]. These factors make this protocol less than ideal for our system.

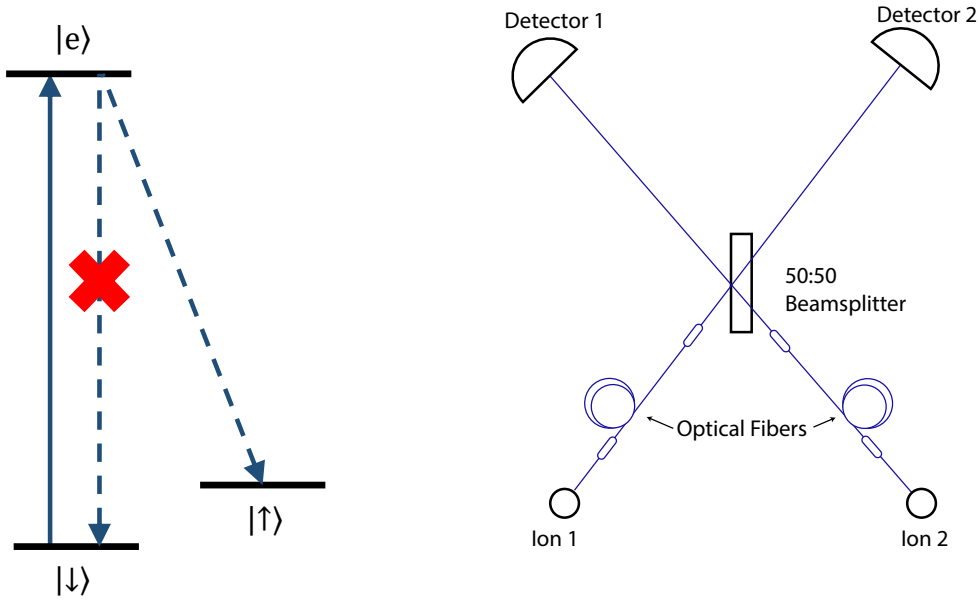

(a) (b)

Figure 3.1: (a) Energy level diagram for the photon number entanglement protocol. Each ion is prepared in $|\downarrow\rangle$, and then weakly excited to $|e\rangle$. The polarization corresponding to the decay back to $|\downarrow\rangle$ must be filtered out, ensuring that any collected photons correspond to population in the state $|\uparrow\rangle$. (b) Diagram of the detection setup for this protocol. Light is collected from both atoms and then coupled into optical fibers to clean up the spatial mode before combining the paths on a 50:50 beamsplitter to erase the path information. Detection of a single photon at one of the detectors heralds the creation of an entangled state between the two ions.

3.1.2 Frequency Qubits

Two photonic degrees of freedom that are more straightforward to entangle with a trapped ion's spin state are frequency and polarization. Protocols for these qubits generate strong ion-photon entanglement, and allow for high excitation probabilities without affecting experimental rate [79]. To have a well-defined frequency qubit, the $|\uparrow\rangle$ and $|\downarrow\rangle$ states must have a frequency splitting much larger than the linewidths of the decays used. The magnetic fields we tend to operate at produce the Zeeman splitting between different m_F levels that is typically similar to the decay linewidths, making hyperfine structure necessary for a frequency qubit.

The first step for both the frequency qubit and polarization qubit entanglement protocols is to prepare a pure state in the excited state manifold [76]. This is typically accomplished by preparing the ion to a ground state level and then applying a fast pulse of resonant light to excite population to $|e\rangle$. In chapter 5 we will explore how fast this pulse needs to be, and how slow pulses can introduce errors into the resultant entanglement. Unit excitation probability is ideal, but imperfect population transfer only affects the rate of the protocol and not the fidelity of the final state. Upon decay, either the frequency or polarization of the emitted photon from the multiple decay channels can become entangled with the resulting spin state of the atom. The unnormalized state of the ion-photon system after a decay is [80]:

$$\psi = \sum_{i,j,\Delta m} C_{i,j,\Delta m} \left|S_i\right\rangle \left|\nu_j\right\rangle \left|\Pi_{\Delta m}\right\rangle \tag{3.2}$$

where $C_{i,j,\Delta m}$ is the Clebsch-Gordan coefficient for the decay, ν_j is the photon fre-

quency, $\Pi_{\Delta m}$ is the photon polarization, and S_i is the resulting atomic state.

For a frequency qubit, light must be collected from two decays to different hyperfine levels $|\downarrow\rangle$ and $|\uparrow\rangle$ as shown in Fig. 3.2(a). It is critical that the polarization of these decays be the same, so decays with other polarizations are filtered out to ensure a pure entangled state is created [48]. Assuming equal CG coefficients, after the decay the atom-photon state will be $(|\downarrow b\rangle + |\uparrow r\rangle)/\sqrt{2}$ where $|b\rangle$ and $|r\rangle$ denote the higher (blue) and lower (red) photon frequency states respectively.

3.1.3 Polarization Qubits

A frequency qubit is very robust to propagation through fiber, but rotations and state detection are very difficult. Thus, for applications where photonic qubit manipulation is important [81], where the atoms being used lack hyperfine structure [82], or for implementation into a cavity [83], polarization may represent a superior qubit. Similar to the frequency qubit scheme, to generate ion-photon entanglement with a polarization qubit, the atom is first excited to a short-lived excited state $|e\rangle$ and then decays along one of two paths to either $|\downarrow\rangle$ or $|\uparrow\rangle$. Rather than a frequency difference, these decay paths must now have separate polarizations.

There is one additional piece of complexity for polarization qubits: The atomic decay polarizations ($\sigma^{\pm}$ and π) do not in general map onto the linear and circular polarizations that we can measure and manipulate easily in the lab. In order to ensure that the collected photons from different decays are distinguishable, one of two convenient geometries must be used. The first is to look at σ^+ and σ^- decays

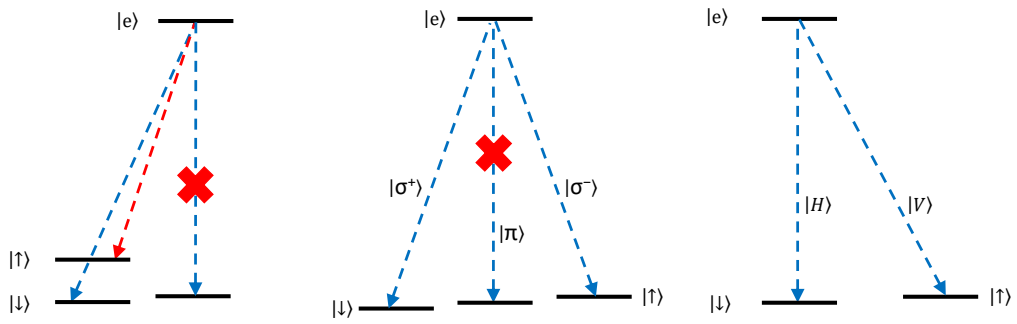

(a) (b) (c)

Figure 3.2: (a) Energy level diagram for ion-photon entanglement with frequency qubits. Decays from $|e\rangle$ to two different ground state hyperfine levels are collected. This scheme often requires polarization filtering of unwanted decay lines. (b) Energy level diagram for the $\sigma^{\pm}$ scheme for polarization qubits. For this scheme, photons must be collected along the magnetic field direction, and π decays must be filtered out. (c) Energy level diagram for the H-V scheme for polarization qubits. Here, light is collected about an axis perpendicular to the B field, and often energy levels do not require any filtering.

with collection optics parallel to the magnetic field (see Fig. 3.2(b)). Along this axis, σ^+ and σ^- polarized photons map onto right-handed (σ^R) and left-handed (σ^L) circularly polarized light respectively. Additionally, no π light is collected directly along this axis and even at larger collection angles, the π decays do not couple into a single-mode optical fiber, providing an easy method for filtering them out [84].

The other convenient geometry is to collect σ^+ (or σ^-) and π decays as shown in Fig. 3.2(c) about an axis perpendicular to the magnetic field. In this configuration, σ and π polarizations map onto orthogonal linear polarizations H and V respectively, corresponding to horizontal and vertical if the B-field is in the vertical direction.

For all of these schemes, it is important to consider both the Clebsch-Gordan coefficients and the radiation profile of the relevant polarizations when considering the final state created. Ideally, these would produce a maximally entangled state with equally weighted populations on each term. If the atomic level structure prevents this, perfect entanglement can still be achieved at the cost of experimental rate by introducing a polarization-dependent loss into the collection system [85].

It is also important to note that the mappings from atomic decay polarizations to lab-measurable polarizations is only exact directly along the specified axis. To perform experiments in the lab, light must be collected over some non-zero solid angle given by the collection optics, leading to errors in the resulting ion-photon entanglement. These errors, and ways to mitigate them are discussed in detail in Chapter 5.

3.2 Remote Ion-Ion Entanglement

We have already briefly discussed how weak ion-photon entanglement can be used to generate remote ion-ion entanglement in the single photon detection scheme, as well as some factors that limit this scheme's usefulness for our purposes. In this section, we will discuss the two-photon detection scheme which is compatible with strong ion-photon entanglement and is used to generate remote entanglement in this thesis. This scheme does not rely on cooling to the Lamb-Dicke limit, and it is not sensitive to optical path length fluctuations [79, 86]. Only polarization qubits are used in the experiments presented in this work, so we will focus on that implementation of the remote entanglement generation protocol, though the implementation for frequency qubits is very similar [87].

First, the scheme described in the previous section is used to create two identical ion-photon entangled systems. Next, if the σ scheme was used (as in Fig. 3.2(b)), we apply a quarter wave plate to rotate the photon into the $\{H, V\}$ basis. The combined ion-photon state from systems a and b can now be written as:

$$\psi = \frac{1}{2}(|\downarrow H\rangle + |\uparrow V\rangle)_a \otimes (|\downarrow H\rangle + |\uparrow V\rangle)_b. \tag{3.3}$$

This can be rewritten in the Bell basis of entangled states:

$$\begin{aligned}\psi =& \frac{1}{2}(\left|\Psi^+\right\rangle_{\text{atom}} \left|\Psi^+\right\rangle_{\text{photon}} + \left|\Psi^-\right\rangle_{\text{atom}} \left|\Psi^-\right\rangle_{\text{photon}} \\ &+ \left|\Phi^+\right\rangle_{\text{atom}} \left|\Phi^+\right\rangle_{\text{photon}} + \left|\Phi^-\right\rangle_{\text{atom}} \left|\Phi^-\right\rangle_{\text{photon}}),\end{aligned} \tag{3.4}$$

where $|\Psi^\pm\rangle_{\text{atom}} = |\uparrow_a\downarrow_b\rangle \pm |\downarrow_a\uparrow_b\rangle$, $|\Phi^\pm\rangle_{\text{atom}} = |\uparrow_a\uparrow_b\rangle \pm |\downarrow_a\downarrow_b\rangle$, $|\Psi^\pm\rangle_{\text{photon}} = |H_a V_b\rangle \pm$

$|V_aH_b\rangle$, and $|\Phi^{\pm}\rangle_{\text{photon}} = |H_aH_b\rangle \pm |V_aV_b\rangle$ are the maximally entangled Bell states.

These photons are then collected by optical fibers and directed onto a beamsplitter as shown in Fig. 3.3. For the components of the wavefunction with even parity ($|\Phi^{\pm}\rangle$), identical photons impinge on the beamsplitter, and their behavior is described by the Hong-Ou-Mandel effect [88, 89]. These photons will always exit from the same port of the beamsplitter, and because they are the same polarization they will also exit through the same port of the subsequent polarizing beamsplitter. Thus, the $|\Phi^{\pm}\rangle$ component of the wavefunction will never result in clicks on two different detectors.

The odd parity terms ($|\Psi^{\pm}\rangle$), however, correspond to photons of orthogonal polarizations. These photons do not interfere and behave as single photons incident on different modes of a beamsplitter as shown in Fig. 3.3(b). The action of the beamsplitter on single photons can be described in terms of the creation operators for these modes [90]. $\hat{a}_3^\dagger = \frac{1}{\sqrt{2}}(\hat{a}_1^\dagger - \hat{a}_2^\dagger)$ and $\hat{a}_4^\dagger = \frac{1}{\sqrt{2}}(\hat{a}_1^\dagger + \hat{a}_2^\dagger)$. We can rewrite these equations to see more clearly what affect the beamsplitter will have on the various input modes:

$$\begin{aligned} \hat{a}_1^\dagger &= \frac{1}{\sqrt{2}}(\hat{a}_3^\dagger + \hat{a}_4^\dagger) \\ \hat{a}_2^\dagger &= \frac{1}{\sqrt{2}}(-\hat{a}_3^\dagger + \hat{a}_4^\dagger). \end{aligned} \tag{3.5}$$

Now we can look at what effect the beamsplitter will have on the odd parity terms. Here we must consider both the horizontal and vertical light in each of the two input modes labeled 1 and 2, and the two output modes labeled 3 and 4 in Fig. 3.3(b), for a total of eight modes.

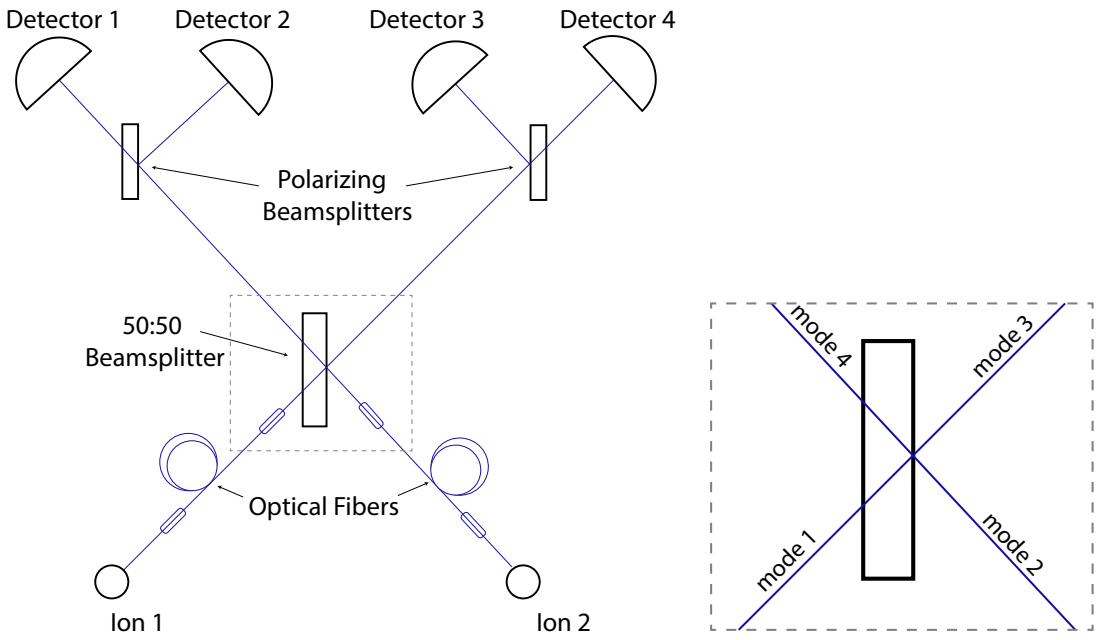

(a) (b)

Figure 3.3: (a) Hong-Ou-Mandel interferometer for two photon interference of polarization qubits. Photons from each ion are collected through optical fibers and interfered at the 50:50 beamsplitter. Based on the HOM effect, identical photons will bunch and only a single detector will fire. Non-identical photons, however, may either bunch or antibunch, and will always be separated at the polarizing beamsplitter, causing separate detectors to fire. Coincident clicks on certain detector pairs effects a destructive measurement of the polarization state of the photons in the Bell basis. The ions are not destroyed, and are projected into the same maximally entangled Bell state. (b) Inset of the beamsplitter from (a) showing the input and output modes.

$$\begin{aligned}\Psi^{+}_{\text{photon}} &= \frac{1}{2}(\hat{a}^{\dagger}_{1H}\hat{a}^{\dagger}_{2V} + \hat{a}^{\dagger}_{1V}\hat{a}^{\dagger}_{2H}) \\ &= \frac{1}{4}[(\hat{a}^{\dagger}_{3H} + \hat{a}^{\dagger}_{4H})(-\hat{a}^{\dagger}_{3V} + \hat{a}^{\dagger}_{4V}) + (\hat{a}^{\dagger}_{3V} + \hat{a}^{\dagger}_{4V})(-\hat{a}^{\dagger}_{3H} + \hat{a}^{\dagger}_{4H})] \\ &= \frac{1}{2}(-\hat{a}^{\dagger}_{3V}\hat{a}^{\dagger}_{3H} + \hat{a}^{\dagger}_{4V}\hat{a}^{\dagger}_{4H}).\end{aligned} \tag{3.6}$$

So just as with the even parity terms, photons corresponding to the $|\Psi^{+}\rangle$ will always exit the same port when exiting the beamsplitter. Unlike the $|\Phi^{+}\rangle$ terms, however, these bunched photons are of opposite polarizations, and so they will be split at the subsequent beamsplitter, leading to coincident clicks on either detectors 1 and 2 or on detectors 3 and 4.

Finally we can look at what the beamsplitter does to the $|\Psi^{-}\rangle$ term:

$$\begin{aligned}\Psi^{-}_{\text{photon}} &= \frac{1}{2}(\hat{a}^{\dagger}_{1H}\hat{a}^{\dagger}_{2V} - \hat{a}^{\dagger}_{1V}\hat{a}^{\dagger}_{2H}) \\ &= \frac{1}{4}[(\hat{a}^{\dagger}_{3H} + \hat{a}^{\dagger}_{4H})(-\hat{a}^{\dagger}_{3V} + \hat{a}^{\dagger}_{4V}) - (\hat{a}^{\dagger}_{3V} + \hat{a}^{\dagger}_{4V})(-\hat{a}^{\dagger}_{3H} + \hat{a}^{\dagger}_{4H})] \\ &= \frac{1}{2}(\hat{a}^{\dagger}_{3H}\hat{a}^{\dagger}_{4V} - \hat{a}^{\dagger}_{3V}\hat{a}^{\dagger}_{4H}).\end{aligned} \tag{3.7}$$

We see that for this term, the photons exit opposite ports of the beamsplitter, leading to coincident clicks on detectors 1 and 4 or detectors 2 and 3. This behavior of bunching and antibunching can also be understood in terms of the symmetry of the overall photonic wavefunction, where only the antisymmetric $|\Psi^{-}\rangle$ term leads to antibunching [88].

Coincident clicks on a pair of detectors, then, collapse the wavefunction from Equation 3.4 and project the atom state onto $|\Psi^{+}\rangle$ if the coincidence was on detector pairs 1-2 or 3-4, or onto $|\Psi^{-}\rangle$ if the coincidence was on detector pairs 1-4 or 2-3.

Ideally, there should never be coincident clicks on pairs 1-3 or 2-4. Because both of these are maximally entangled bell states, this completes the remote entanglement generation protocol.

From equation 3.4 we see that after the decays, half of the system's population is in the $|\Phi^{\pm}\rangle$ states. Because these states cannot be detected by this protocol, the rate of entanglement generation suffers by a factor 2 and the success is inherently probabilistic. In practice, the need to collect both photons, couple them into fibers, and register them on the detector limits the success probability much more severely than this factor of 0.5 from Bell state readout. The overall success probability for this scheme is given by [87]

$$P_s = P_{|\Psi\rangle}(p_e p_d \frac{\Delta\Omega}{4\pi} T_{\text{fiber}} T_{\text{optics}} Q_e)^2 \tag{3.8}$$

where $P_{|\Psi\rangle} = 0.5$ is the probability the system decays into one of the Bell states that we can measure, p_e is the probability that an atom is excited and should approach one, p_d is the probability that the decay photon is a polarization that we do not filter out. This value will typically vary from 0.5 to 1 based on the atomic structure of the ion and geometry of the system used. $\frac{\Delta\Omega}{4\pi}$ represents the fraction of the solid angle of emission from the ion that is collected by our lens. T_{fiber} and T_{optics} refer to the transmission through the fiber and other optics in the system including coupling losses into the fiber, and Q_e is the quantum efficiency of the detector.

The quadratic dependence on most of these terms comes from the need to collect a photon from both ions simultaneously for the protocol to work. In a

practical sense, this means that any improvements or sacrifices to photon collection have a strong impact on the final rate. Our best value for P_s is $\sim 10^{-5}$ [91], mainly limited by $T_{\text{fiber}} = 0.14$, $Q_e = 0.35$, and $\frac{\Delta\Omega}{4\pi} = 0.1$ [60]. In Chapter 5 we will discuss steps that have already been taken, and other possible options to improve these numbers. Additionally, because successful attempts are heralded by coincident clicks on a pair of detectors, this low probability does not prohibit its implementation into a larger network as it does not rely on post-selection of the data [87].

3.3 Integrating Remote and Local Entanglement

In Chapter 1 we discussed how the path from elementary demonstrations of quantum resources to implementation within a larger system can be a non-trivial exercise. Much of the rest of this thesis is dedicated to expanding these remote entanglement generation protocols for integration with local operations which were introduced in Chapter 2 and have been extensively studied and refined on trapped ion systems [10, 92–94]. In this section I will discuss the first step we took towards achieving this integration by first generating remote entanglement between two $^{171}Yb^+$ atoms in separate traps and then performing a local entangling gate on one of these ions and another co-trapped Yb atom [91]. Additionally, this section will introduce the experimental structure of using a "fast loop" and a "slow loop," which will be common to many future results.

This experiment was performed on ions in two traps labeled A and B, separated by about 1 m. Two $^{171}Yb^+$ ions were trapped in module A and a single Yb ion was

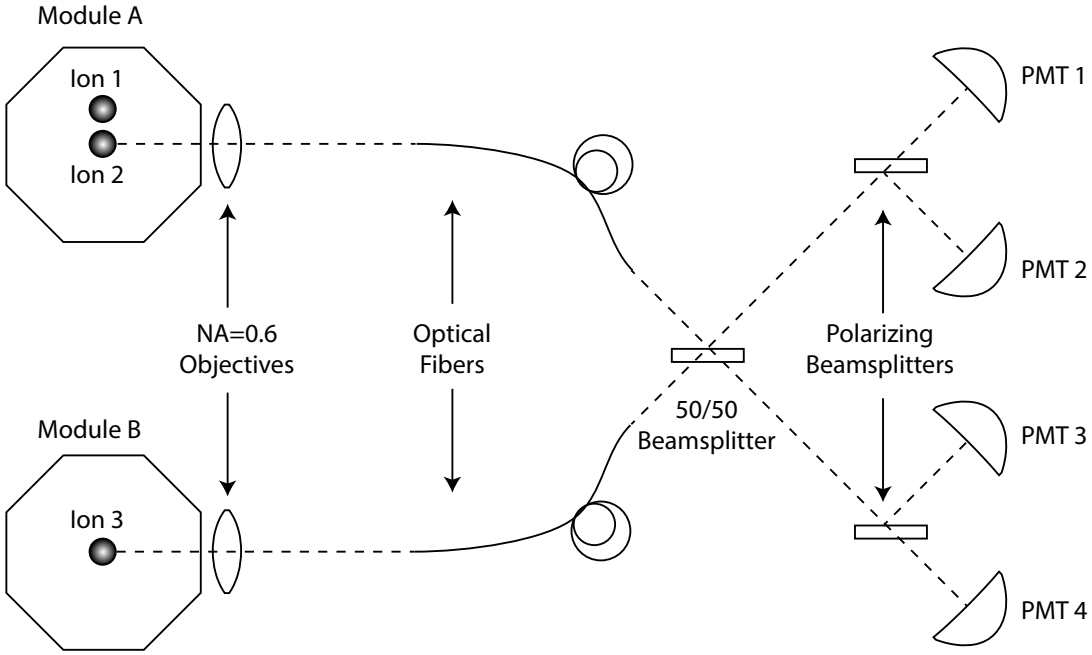

Figure 3.4: Setup for the so called "2x1 experiment." Two ion modules were used, with two ions in module A and a single ion in module B. Light from ions 2 and 3 was collected to be sent into a photonic Bell state analyzer similar to Fig. 3.3. Additionally, an individually focused pump beam can address only atom 1 and Raman beams are aligned to perform a Mølmer-Sørensen gate between atoms 1 and 2.

trapped in module B as shown in Fig. 3.4. First, the ions were all initialized into the state $|\Downarrow\rangle$. Next, an ultrafast ($\sim$ 1 ps) pulse of resonant 369 nm light was used to simultaneously excite population in atoms 2 and 3 to the short lived level $\left|^2P_{1/2}, F = 1, m_F = 0\right\rangle \equiv |e\rangle$. The σ^+/σ^- geometry was used in this experiment (see Fig. 3.2(b)) so an NA = 0.6 PhotonGear microscope objective was positioned to collect light along the magnetic field direction.

This light was sent through a quarter wave plate to rotate the polarization of the photons from $\sigma^+ \rightarrow H$, and $\sigma^- \rightarrow V$. This ensures that the polarizing beamsplitters in the Bell state analyzer behave as described in the previous section. The light is then coupled into single-mode optical fibers, which serve several purposes. First, it cleans up the spatial modes of the emitted photons, which is necessary to achieve good interference at the beamsplitter [95]. Second, as discussed above, they serve to filter π light out, since that spatial mode does not couple into the fiber. Third, the optical fiber provides sufficient spatial filtering to ensure that light from ion 1 does not make it to the interferometer. And forth, strain can be applied to the fibers by a set of fiber paddles to ensure that the same polarization comes out of the fibers as goes into them.

The output of these fibers are incident on a free space Bell state analyzer as shown in Fig. 3.3. Aligning the fibers for maximal overlap on the beamsplitter is very important [48], but difficult to set and maintain. Reference [60] gives a thorough discussion on how this was achieved, but going forward, a transition to visible photons should allow this interferometer to be implemented with in-fiber beamsplitters, ensuring perfect mode overlap.

At the output of the interferometer were four photomultiplier tubes (PMTs) used as single photon detectors with a quantum efficiency of 0.35. These PMTs are gated open for a window of 60 ns after the fast pulse, and coincident clicks on certain pairs of detectors heralds the creation of an entangled state between atoms 2 and 3.

This process of state preparation, fast pulse, and waiting for coincidence clicks constitutes the so called "fast loop" of the experiment. These steps are repeated over and over, stopping to Doppler cool for 100 μs every 200 cycles, until a pair of coincident clicks is actually registered. In practice, this fast loop was implemented with a repetition rate of 470 kHz. Once a coincidence has been measured, we break out of the fast loop and begin the slow loop. This would occur at a rate of 4.5 s^{-1}.

At the beginning of the slow loop, the state of ions 2 and 3 is:

$$\psi_{2,3} = |-\rangle\,|+\rangle + e^{i\phi_D}\,|+\rangle\,|-\rangle \tag{3.9}$$

where $|-\rangle \equiv \left|^2S_{1/2}, F=1, m_F=-1\right\rangle$ and $|+\rangle \equiv \left|^2S_{1/2}, F=1, m_F=+1\right\rangle$ are the Zeeman sublevels of the S manifold and ϕ_D is the phase acquired based on which pair of detectors fired. In order to go from these magnetically sensitive levels to the familiar clock basis, the first step of the slow loop is to apply microwave rotations. This consisted of a series of π pulses, first to drive population from $|+\rangle \rightarrow |\Downarrow\rangle$, then a second pulse drove $|\Downarrow\rangle \rightarrow |\Uparrow\rangle$, and finally, a third pulse performed $|-\rangle \rightarrow |\Downarrow\rangle$.

So far we have not been keeping track of the state of atom 1. Because we do not know whether it emitted a photon after the fast pulse of resonant light, it is

in a mixed state at this point in the experiment. In order for it to be useful for subsequent operations, then, it needs to be reinitialized into the $|\Downarrow\rangle$ state. To do this, a narrowly focused beam of pumping light is applied to only ion 1. After this, the three ion state is

$$\psi_{1,2,3} = |\Downarrow\rangle_1 (|\Downarrow\rangle_2 |\Uparrow\rangle_3 + e^{i(\phi_D+\phi_r)} |\Uparrow\rangle_2 |\Downarrow\rangle_3). \tag{3.10}$$

with the added phase ϕ_r accounting for the phase acquired by the microwave rotations.

Next, the MS interaction described in the previous chapter is applied to atoms 1 and 2. This creates the 3-particle entangled state:

$$\psi_{1,2,3} = (|\Downarrow\Downarrow\rangle_A - ie^{i\phi_A} |\Uparrow\Uparrow\rangle_A) |\Uparrow\rangle_B + e^{i\phi_{AB}} (|\Downarrow\Uparrow\rangle_A - i |\Uparrow\Downarrow\rangle_A) |\Downarrow\rangle_B . \tag{3.11}$$

Here, the intermodular phase $\psi_{AB} = (\psi_D + \psi_r)$, and the intramodular phase ψ_A is the phase acquired by the MS gate. We see that the parity of ions 1 and 2 is correlated with the spin state of ion 3. To verify this entanglement, a $\pi/2$ Raman rotation is performed on ions 1 and 2 with a varying phase. The state of all three atoms is then read out and the results are analyzed. When atom 3 is found to be in state $|\Downarrow\rangle$, the parity of atoms 1 and 2 should oscillate with the phase of this $\pi/2$ rotation. When the state of atom 3 is found to be $|\Uparrow\rangle$, though, the atoms in module A should have 0 average parity regardless of the phase of the final rotation [60].

Results with and without the final rotation are plotted in Fig. 3.5 [91], and confirm that the three particle entangled state was indeed created. The average

fidelity of the entangled state in module A, based on the measurement of the state of ion 3 was 0.63(3). This was limited primarily by polarization mixing on the photonic qubits, imperfect mode-matching at the beamsplitter, and poor MS gates (F=0.85) due to a imperfect cooling to the Lamb Dicke regime.

As already mentioned, the mode matching can be addressed by using an in-fiber beamsplitter with visible photons. The MS gate infidelity was due partially to an anomalously high heating rate in the segmented blade trap used for module A, which had $\dot{\bar{n}} \approx 1$ ms^{-1} on the mode that was used. This will hopefully be addressed by using new traps in the future. Part of the issue, however, also came from our inability to perform sub-Doppler cooling techniques such as resolved sideband cooling [96]. These techniques help get the ions deep into the Lamb Dicke regime [30], but they would have been prohibitively long to include in the experiment's fast cycle. Although we have since demonstrated a slightly faster method of ground state cooling which will be discussed next chapter, our need for high repetition rates in the fast loop will likely prevent us from attaining cutting edge local gate fidelities in experiments involving remote entanglement for years to come.

At the time of my writing this thesis, the polarization mixing is also still an ongoing limitation on our ion-photon entanglement fidelities. We attribute it to either polarization-dependent loss or spatially inhomogeneous birefringence in the vacuum window. These may be introduced by stresses during chamber construction and baking, and in the future it may be wise to inspect the optical properties of the vacuum window before building up so much structure around the trap to make a thorough inspection onerous. More so than these sources of error, though, the

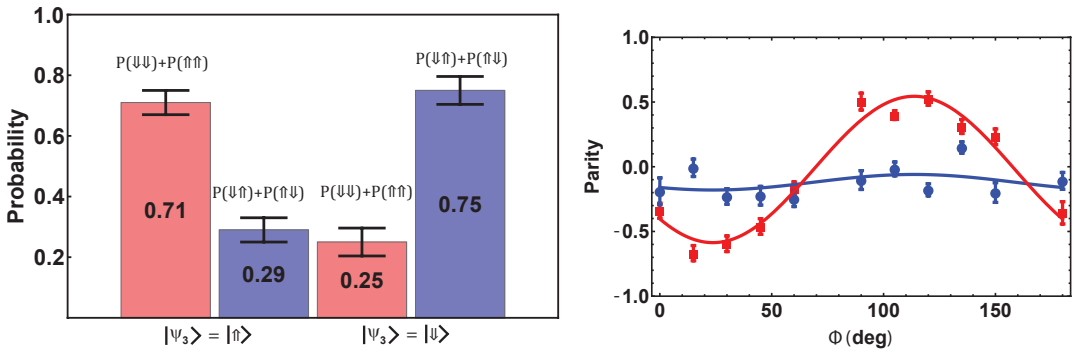

(a) (b)

Figure 3.5: (a) Populations are read out after performing both remote and local entangling operations. Here, no $\pi/2$ analysis pulse was performed. We see that atoms 1 and 2 are more likely to be in an even parity state when atom 3 is measured in state $|\Uparrow\rangle$ and they are more likely to have odd parity when $|\Psi_3\rangle = |\Downarrow\rangle$. (b) Coherences are shown by performing a $\pi/2$ rotation on atoms 1 and 2 after generating the three particle entangled state. As expected, the parity of atoms oscillates with the phase of the $\pi/2$ pulse in the case that $|\Psi_3\rangle = |\Uparrow\rangle$ (red points) and does not oscillate for $|\Psi_3\rangle = |\Downarrow\rangle$ (blue points).

need to reinitialize the state of ion 1 after breaking out of the fast loop is a much more fundamental limitation to the ability to expand on this protocol. The next section will discuss why this is such a problem and the steps that we have taken to overcome it.

3.4 Motivation for Dual Species

A fundamental issue with the ability to scale this system to larger networks is shown by the need to reinitialize the state of ion 1 in the middle of the experiment. For a quantum network to be useful for distributed quantum computing, it needs to be able to hold onto quantum information while the remote link is established [29]. Unfortunately, in this protocol, establishing that remote link involves shining resonant 369 nm light on an atom that is separated from the memory ion by as little as 5 μm. Focusing a pulsed beam well enough to avoid spoiling the memory qubit after one pulse would not be impossible, but because this is a probabilistic scheme, establishing that remote link requires an average of $\sim 10^5$ pulses.

Interestingly, this problem of disturbing local memories during the generation of a remote link is not unique to trapped ions. Another platform that is currently combining photonic and local operations is NV centers in diamond, and they are also plagued by a cross-talk between these processes [97].

One approach to isolate the memory qubits from the photon generating process would be to physically separate the atoms from each other as the remote connection is generated, and then shuttle them back together for local operations [45]. A more

straightforward approach, and the one that we have elected to pursue is to introduce a second atomic species to the trap [98] for use in generating the remote link. Using $^{171}Yb^{+}$ ions as memory qubits and $^{138}Ba^{+}$ ions as communication qubits allows us to excite the Ba ion with 493 nm or 650 nm light, which are off-resonant from any transitions in Yb. This completely divorces the remote entanglement generation from the qubit storage mechanism.

Moreover, many proposals have called for the addition of a separate atomic species into trapped ion chains to sympathetically cool the chain during longer computations [30,99]. There are several other factors that make $^{138}Ba^{+}$ a good choice for use as a communication ion. While most ions have their primary transitions in the UV wavelengths, barium has two strong lines in the visible range: a primary cooling transition from the $6^2S_{1/2}$ to $6^2P_{1/2}$ at 493 nm and a repump line with a 1:3 branching ratio from $5^2D_{3/2}$ to $6^2P_{1/2}$ at 650 nm. Compared to the UV transitions in most ions, these visible lines suffer less attenuation through optical fibers, permit access to a larger collection of supporting technologies, and can be converted to IR wavelengths for longer-distance networks [100].

Finally, we still intend to perform two-qubit gates on the hybrid chain by addressing their collective modes of motion in a trapping potential [98, 101]. To ensure that both ions contribute strongly to these normal modes, it is important that they be near each other in mass, so it was important to choose another heavy ion to match $^{171}Yb^{+}$.

Chapter 4: Building the Barium Toolkit

In Chapter 2, we discussed how the DiVincenzo criteria have been satisfied with $^{171}Yb^{+}$ ions, and much of my graduate work has involved rebuilding that toolkit for Ba ions. Barium has a long history in trapped ion quantum computing [102–104], and it has even been used before in ion-photon experiments [78,105]. The first novel challenge that we have sought to overcome, though, has been to reinvent these tools in such a way as to add minimal complexity when integrated with our existing Yb system. First, this has meant that we use the $^{138}Ba^{+}$ isotope of Ba, which has 0 nuclear spin, allowing us to avoid adding the sidebands necessary for addressing different hyperfine levels.

Also, while Ba ion trap experiments typically perform state readout by shelving the atom to its $^{2}D_{5/2}$ level, this requires a narrow-linewidth laser [106]. Because our ultimate architecture calls for Ba ions to be used only for generating a photonic link, and for all of the local processing and readout to be performed on Yb ions, we elected to forgo this complex equipment. Nonetheless, Ba state detection is important for many of the experiments presented in this work, and so alternative methods have been developed and implemented.

Though subject to these design constraints, many of the tools and techniques

we have developed that will be discussed in this chapter have unlocked new possibilities for the Ba ion, particularly with regards to the use of its low-lying $^2D_{3/2}$ level. Details on these new possibilities will be explored in the following sections. In parallel to Chapter 2, this chapter will be loosely organized in terms of how DiVincenzo's criteria have been realized on the Ba platform.

4.1 The $^{138}Ba^+$ Atom

With its long history in the field, $^{138}Ba^+$ has been well-characterized as a physical system [107, 108]. As with Yb, every $^{138}Ba^+$ ion is fundamentally identical, removing the need to calibrate every qubit. Our Ba qubit is defined in the two ground state levels of the $6^2S_{1/2}$ manifold: $|J = 1/2, m_J = -1/2\rangle \equiv |\downarrow\rangle$ and $|J = 1/2, m_J = +1/2\rangle \equiv |\uparrow\rangle$. These levels as well as other energy levels commonly addressed in $^{138}Ba^+$ are shown in Fig. 4.1. Unlike the $^{171}Yb^+$ qubit, these Zeeman levels are first-order magnetic field sensitive with an energy splitting of 2.8 MHz/G, resulting in shorter coherence times.

4.1.1 Ba Oven Tests

The first step to actually realizing Ba as a physical platform is to trap it. This is done in a process similar to Yb, by resistively heating an atomic source oven to direct a beam of neutral atoms towards the trapping region for photoionization. Constructing the atomic source oven, however, is significantly more difficult with Ba than Yb due to the fact that Ba oxidizes quickly when exposed to oxygen or

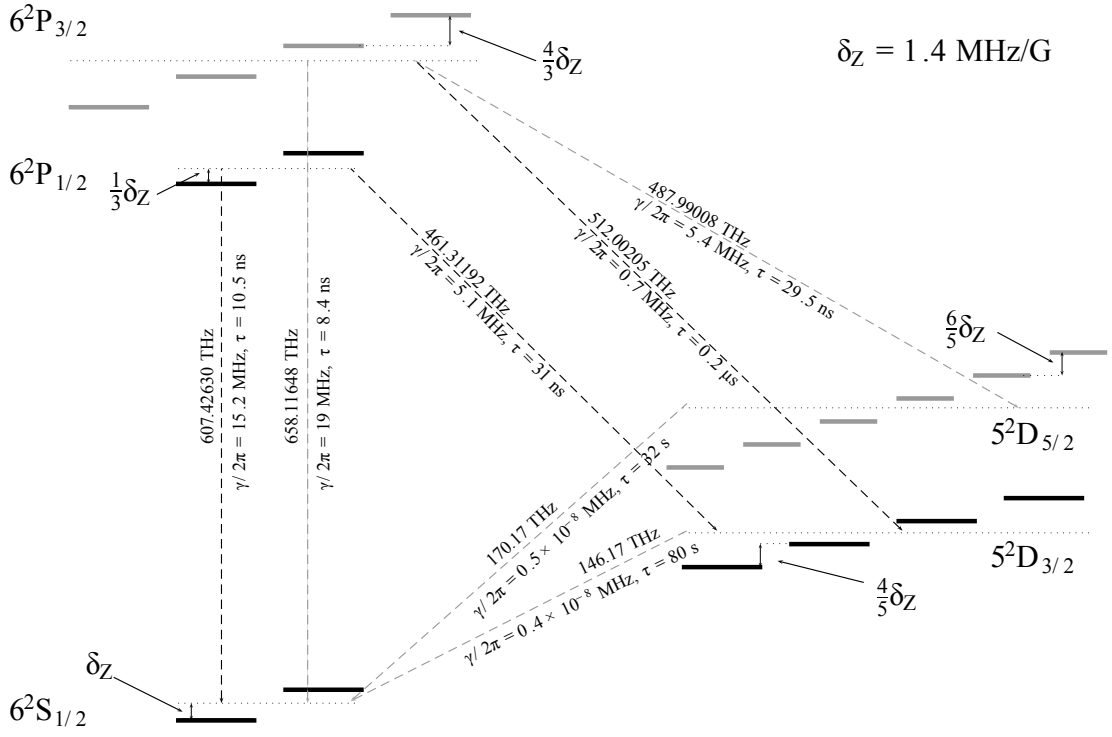

Figure 4.1: Energy level diagram for the $^{138}Ba^{+}$ ion. Lines that we directly apply are shown in black. Other common lines are included in gray.

water vapor in air. Our original solution for overcoming this was to use alvasource ovens from AlvaTec. These ovens contain atomic barium packed under a pure argon environment and capped with an indium seal. It is claimed that resistively heating this seal causes it to melt away and expose the atomic source underneath, and this behavior was observed for the first oven we used. Unfortunately, when a second alvasource oven was heated, the back pressure fired the indium seal outwards and onto the trap, shorting electrodes and ruining the trap.

To avoid another such disaster, a test chamber was built for evaluating Ba source ovens without risking an entire trap or having to wait for a long bake. This chamber consisted of a bell jar, electrical feedthroughs with thick gauge wire, and an attachment to a Pfeiffer HiCube pump station. These feedthroughs served both to run current through the oven and as mechanical support. The turbo pump could bring pressures to $\sim 10^{-7}$ Torr in less than an hour, allowing for quick iterations.

To test an oven, it was mounted in the test chamber as shown in Fig. 4.2, and a 791 nm beam was directed at the front of the opening. This light is resonant with the transition from the $^1S_0$ ground state to the $^3P_1$ excited state, and was aligned to be perpendicular to the atomic beam from the oven. The setup was imaged with a ZOSI ZG2116E digital camera, which has high sensitivity to IR light. Additionally, the frequency of the 791 nm beam was modulated around resonance by 1 GHz at a rate of 0.25 Hz. This would cause the laser to be on-resonance with different velocity classes of the atomic beams at different phases of the modulation. Thus, when the neutral barium was fluorescing, the bright spot would move across the atomic beam at the same rate as the modulation. Reflections of blackbody radiation from the

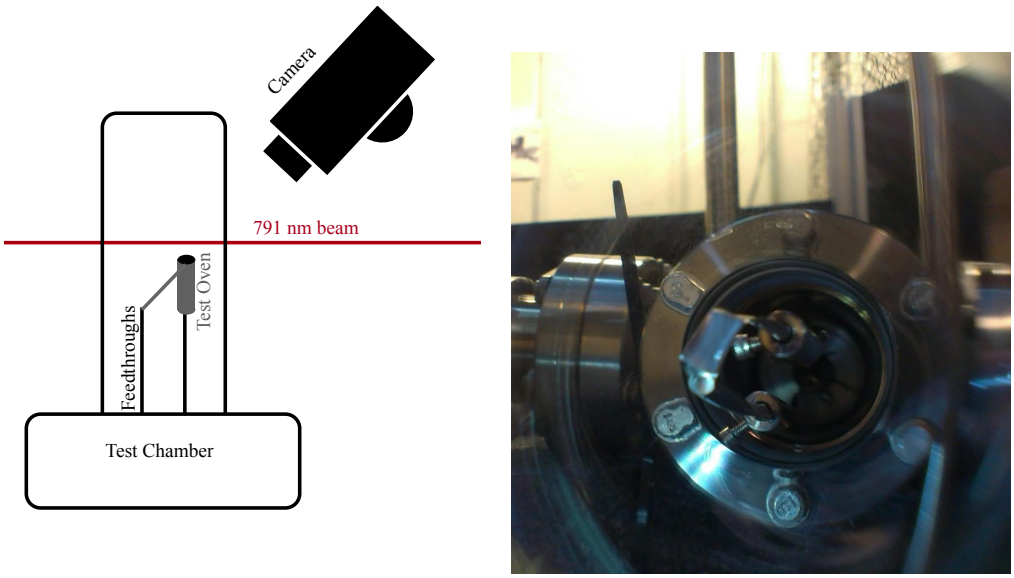

(a) (b)

Figure 4.2: (a) Diagram giving a side view of the oven test setup. (b) Photo of the setup from the top. This is before firing the oven and the indium seal is still intact.

nearby oven could sometimes look like a Ba signal, but this lock-in-style approach made it very clear when we were seeing actual barium fluorescence.

A more complex setup can calibrate the amount of light collected or atoms deposited on a nearby glass slide to characterize the operating temperatures of the ovens [52]. This can be highly dependent on mounting, though, and these tests sought only to see if the ovens would work at all.

First, a series of five additional Alvasource ovens were tested. Two shot their seals out just as in the ruined trap. These both produced a flux of neutral barium afterwards. The other three never shot out their indium seals and no neutral flux

was ever observed. Examination of the ovens after breaking vacuum revealed that the seal had migrated to the very end of the tube, but still blocked the barium.

These results indicated that we needed to find a replacement for the alvasource ovens. One proposed solution was BaAl4, which produce atomic Ba when heated under ideal conditions and is stable under atmosphere [109]. Three ovens were made from SAES getters and tested. An unmodified SAES getter did produce the fluorescence at 11 A of current. The other two tests were for ovens in which we had attempted to put the getter material into a tube for better directionality. Both of these failed to produce fluorescence. Additional tests on BaAl4 also failed to produce positive results, and we deemed the alloy unreliable for loading with a resistively heated oven. It is worth noting, however, that there has been considerable success in loading using similar alloys as an ablative source [110], and so they may remain useful candidates for air-stable atomic sources.

Next, we tested ovens made of pure atomic Ba, that had been assembled under a clean argon environment inside of a glove bag. These ovens reliably produced an atomic flux, but would often have to be initially "activated" by heating them orange-hot with 15 A of current. After this activation, we could see fluorescence at much lower currents. We attribute this activation behavior to a need to briefly melt the Ba to crack a thin oxide layer. At the time of these tests, the source of this oxide layer was a mystery, but we now believe it was caused by residual water vapor on the tools used to manipulate the barium and on the stainless steel tube used as the oven. This may be mitigated by prebaking the tools and tube before putting them in the glove bag.

More recent tests have also revealed that brief ($\sim$ 10 min) exposure to air does not build up enough of an oxide layer to prevent trapping, and so the glove bag may be foregone since it is difficult to use. These tests were all performed in collaboration with James Siverns in the lab of Qudsia Quraishi. Tests have also been performed in our lab using the 413 nm laser to drive $^1S_0 \rightarrow \ ^3D_1^o$ with collection of light on the stronger decay line at 660 nm [111]. This allows the excitation light to be filtered out and provides a stronger signal to noise.

4.1.2 Ba Photoionization

Once the neutral flux has been established, we generate ions by resonant two-photon photoionization. We use a 413 nm laser beam resonant with the transition from $^1S_0 \rightarrow \ ^3D_1^o$ to transfer population to an excited state, and then a second photon from the same beam has enough energy to excite the electron to the continuum, generating a Ba^+ ion. Many of the same considerations apply to this process as in Yb photoionization, and the geometry of the system must be considered to take Doppler shifts into account for the 413 nm frequency (see Chapter 2).

4.1.3 Doppler Cooling

Once ionized and trapped, we require that the Ba atoms be Doppler cooled before we can perform quantum operations. For background on the principle behind Doppler cooling, see Chapter 2. In this section we will discuss how Doppler cooling is implemented on the $^{138}Ba^+$ ion and how its atomic level structure forces additional

considerations beyond those present in $^{171}Yb^{+}$.

The primary cooling transition in Ba is on the $^2S_{1/2} \rightarrow {}^2P_{1/2}$ line at 493 nm. We apply light at this frequency with a CW direct diode laser. $^{138}Ba^{+}$ has no hyperfine structure, so we do not need to apply sidebands to this laser. The $^2P_{1/2}$ excited state has a strong branching ratio (27.1%) to the low-lying $^2D_{3/2}$ level, so we apply 650 nm light from another direct diode CW laser to directly excite population back to $^2P_{1/2}$. Unlike the 935 nm line in $^{171}Yb^{+}$, this repump beam addresses the same excited state as the main cooling line at 493 nm, causing interference between the two lines. We saw in Chapter 2 that the optimal detuning for a 2-level system is $\gamma/2$, but if we naively apply this to both the 493 and 650 beams, we produce a dark state in the S and D manifold, suppressing fluorescence and cooling. In order to find optimal cooling parameters, the lambda system from the S, P, and D states must be taken into account. Moreover, because the splitting between the Zeeman sublevels is of order γ, a full analysis must consider the entire 8-level system.

An in-depth discussion of the 3-level and 8-level system calculations is given in [65, 112], and the results show that optimal fluorescence is achieved by red detuning the 493 nm beam by about $\gamma/2$ and the 650 nm beam *blue* detuned by about the same amount. This allows for cooling on the stronger green line and repumping on the red line while avoiding dark states.

Finally, when 532 nm light is applied to the ions for Raman transitions (this will be discussed later this chapter), off-resonant coupling to the $^2P_{3/2}$ manifold can decay to the $^2D_{5/2}$ states. Population is trapped here for $\sim \gamma = 32$ s before it decays back to the S state. With the 532 nm light left on, this dark state pumping was

observed to happen about once per minute, resulting in ions being dark roughly 50% of the time, which was prohibitive for running experiments. To overcome this, we have implemented a Thorlabs M617F2 fiber coupled 617 nm LED into the optical setup. Light from this LED is collimated and then combined with the sigma beams in free space using a dichroic filter. This center frequency of this LED is 3 nm from the 614 nm $^2D_{5/2} \rightarrow^2 P_{3/2}$ transition, but due to its high intensity and large bandwidth we are still able to drive transitions at a Rabi rate of 30 ms. Though slow on experimental timescales, this is still 1000x faster than the rate of pumping into the dark state, leaving the ion bright for an acceptable 99.9% of the time.

4.1.4 EIT Cooling

While Doppler cooling is sufficient for most experiments we perform in this work, some operations like the Cirac-Zoller gate [4] require additional cooling to the vibrational ground state of motion. Moreover, for barium ions in our trap, the Doppler cooling limit of $\overline{n} = \frac{\gamma}{2\omega}$ where ω is the trap frequency gives $\overline{n} \approx 5$ for a trap frequency $\omega/2\pi = 1.5$ MHz and a transition linewidth $\gamma/2\pi = 15.1$ MHz. This does not put the ion deep within the Lamb-Dicke limit, and for higher fidelities, even the Molmer Sorensen gate may require sub-Doppler cooling [94].

Cooling to sub-Doppler temperatures is often accomplished by resolved sideband cooling [96], but the energy level structure of $^{138}Ba^+$ also allows for implementation of electromagnetically induced transparency (EIT) cooling [113]. This approach is technically simpler than sideband cooling and allows for multiple modes

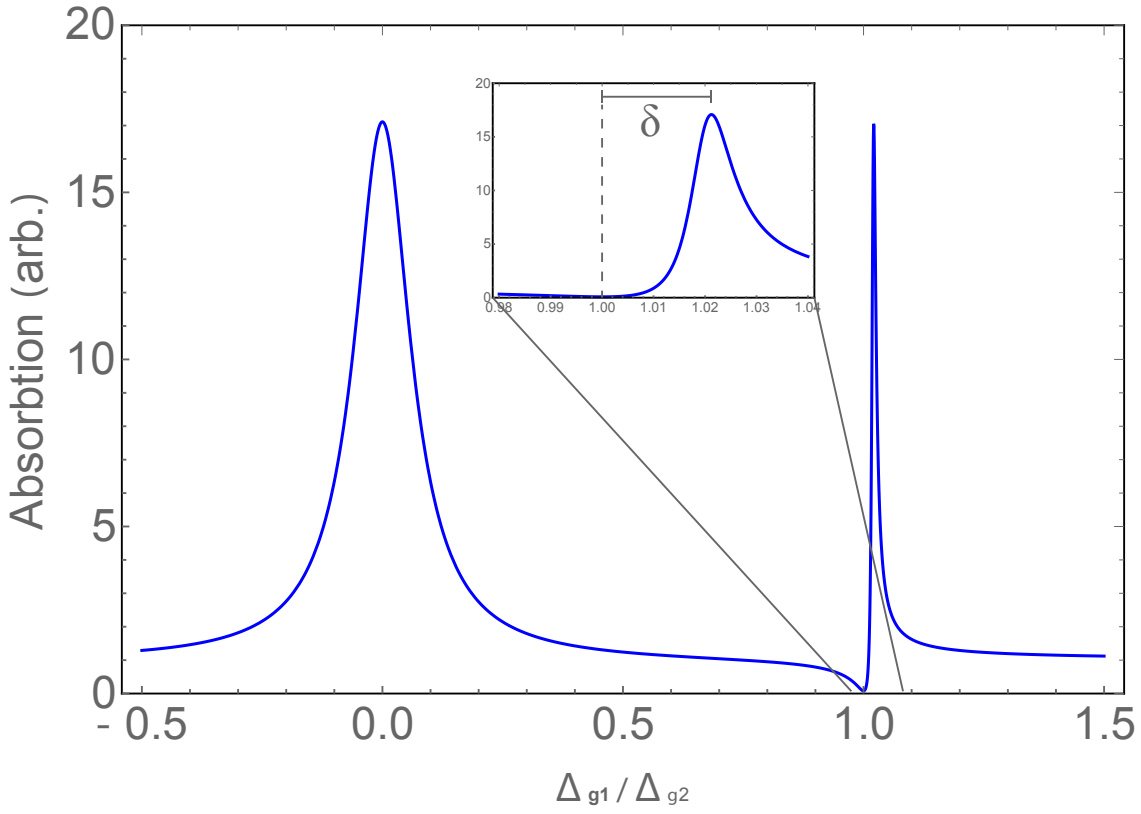

Figure 4.3: Absorption spectrum of the cooling beam in an EIT cooling setup. This beam is detuned from the raw atomic resonance by Δ_{g_1}, producing a broad resonance peak around 0. The zero absorption point at $\Delta_{g_1} = \Delta_{g_2}$ is caused by a dark resonance between the cooling and pumping beams. The narrow peak at $\Delta_{g_1} = \Delta_{g_2} + \delta$ is a bright resonance with the dressed state created by the pumping beam.

of motion to be cooled simultaneously, permitting faster cooling rates [114]. As discussed in Chapter 2, Doppler cooling is limited by atomic recoil. In the case of ions trapped in a harmonic potential, this takes the form of transitions on the line $|g\rangle \leftrightarrow |e\rangle$ that do not reduce the vibrational quantum number. EIT cooling relies on suppressing $|g, n\rangle \rightarrow |e, n\rangle$ and enhancing $|g, n\rangle \rightarrow |e, n-1\rangle$ transitions using a coherent dark state.

This is done in a Λ system with excited state $|e\rangle$ and ground states $|g_1\rangle$ and $|g_2\rangle$. First a strong beam drives the $|g_2\rangle \rightarrow |e\rangle$ transition ($\Omega_{g_2} \sim \gamma$). This "coupling" beam is detuned blue of the atomic transition by Δ_{g_2} and produces ac Stark shift on $|e\rangle$ and $|g_2\rangle$ of $\delta = (\sqrt{\Delta_{g_2}^2 + \Omega_{g_2}^2} - |\Delta_{g_2}|)/2$.

A second "cooling" beam is also applied, which has a broad absorption peak at frequencies near resonance, and also exhibits a narrow Fano-like absorption profile for detuning Δ_{g_1} around Δ_{g_2} (see Fig. 4.3). At $\Delta_{g_1} = \Delta_{g_2}$, an EIT dark resonance is created and this absorption goes to zero, suppressing $|g_1\rangle \rightarrow |e\rangle$ transitions. Conversely, at a detuning of $\Delta_{g_1} = \Delta_{g_2} + \delta$, there is a bright resonance corresponding with the narrow peak of the Fano like profile. If the Rabi rate Δ_{g_2} and detuning Δ_{g_2} are chosen such that δ is equal to the trap frequency ν, this serves to enhance transitions on the $|g_1, n\rangle \rightarrow |e, n-1\rangle$ line that contributes to cooling.

In our lab, we implement EIT cooling in $^{138}Ba^+$ using a σ^+ polarized 493 nm beam to drive transitions on $|\downarrow\rangle \rightarrow |e\rangle$ as the coupling beam and a weaker π polarized beam that drives $|\uparrow\rangle \rightarrow |e\rangle$ as the cooling beam. These beams are both detuned $\sim$ 120 MHz blue of resonance. First, we observe the Fano peak by varying the detuning of the π beam, and observing how much light is scattered by the ion. The

results of this experiment are plotted in Fig. 4.4(a), and produce the expected line shape.

Next we wish to measure the effects of the cooling. We adjust the intensity of the σ coupling beam until the spacing between the maximum and minimum on the Fano peak is equal to the trap frequency. To more easily read out the temperature, we co-trap one Ba and one Yb ion for this analysis. The temperature can then be measured by comparing the strengths of red and blue vibrational sideband transitions on the Yb ion [115]. As shown in Fig. 4.4(b), EIT cooling allows us to prepare the atoms in the vibrational ground state in < 200 μs. Furthermore, because there was no cooling light on the $^{171}Yb^{+}$ ion during this process, this experiment also demonstrates effective sympathetic cooling on the Yb ion.

4.2 $^{138}Ba^{+}$ S State Toolkit

In this section we will discuss how we have implemented state preparation, state readout, and single qubit rotations on the $^{2}S_{1/2}$ manifold of $^{138}Ba^{+}$. More details on these methods are given in [65], but it will serve as useful context for thinking about how many of the more recent D-state operations presented in the following section work. Moreover, these operations, combined with the two qubit entangling gates detailed later this chapter represent a complete gate set for Ba, and are integral to the networking experiments described in the next chapter.

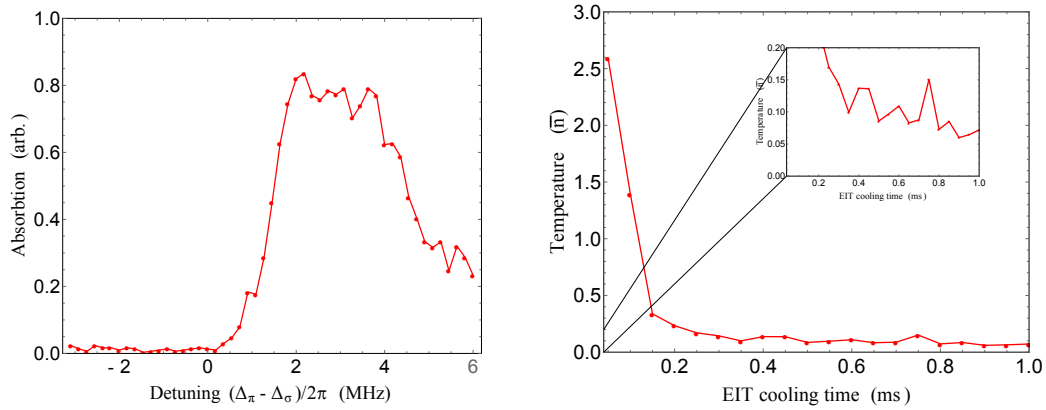

(a) (b)

Figure 4.4: (a) Experimental data on the absorption spectrum of the π beam. Compare to the inset in Fig. 4.3. To maximize cooling, the Fano peak should be at $(\Delta_\pi - \Delta_\sigma)/\nu = 1$, corresponding to the red vibrational sideband. To achieve this in the lab, the intensity of the σ (coupling) beam can be adjusted to change δ. (b) EIT cooling time plot for a Ba-Yb chain. First the chain is Doppler cooled for 300 μs and then EIT cooling is performed for a variable amount of time. Temperature is determined by examining red and blue vibrational sidebands on the Yb atom [115]. This shows that we can cool to $\overline{n} = 0.1$ in 500 μs. Additionally, this confirms that EIT cooling on the Ba atom can sympathetically cool a co-trapped Yb ion.

4.2.1 S State Initialization

In the $^{171}Yb^{+}$ ion, we are able to apply sidebands to the 369 nm light with an EO modulator to address different transitions based on frequency. Because the Zeeman splittings in barium are of order the transition linewidths, though, transitions between different qubit states are not well-resolved in frequency, and so we often rely on polarization selectivity instead to address different transitions. Specifically, we must be able to switch between σ^{+} and σ^{-} polarized light within an experimental cycle. As shown in Fig. 4.5(a), this is implemented using a dedicated polarization board that splits a single beam of 493 nm light into two orthogonal polarizations, puts each through an AOM for fast switching, and then recombines them into a single fiber. Wave plates after the fiber are used to rotate the orthogonal beams into left-handed and right-handed circular polarizations, and beams are sent through the trap along the magnetic field.

In the S manifold, the $|\downarrow\rangle$ state is dark to σ^{-} light and the $|\uparrow\rangle$ state is dark to σ^{+} light. We can therefore optically pump to either of these states by applying the correct polarization of 493 nm light along with all polarizations of 650 nm light.

4.2.2 S State Detection

We discussed in Chapter 2 how we are able to efficiently read out the state of $^{171}Yb^{+}$ by taking advantage of a closed cycling, where the bright state scatters thousands of photons and the dark state scatters none. Unfortunately, no such closed cycling transition exists for $^{138}Ba^{+}$. For either pure σ polarization of applied

493 nm light, the bright state population will be pumped into the dark state after scattering only a few photons. For instance, if σ^+ light is applied, population in the $|\downarrow\rangle$ state will scatter on average 2.8 photons before decaying back to the $|\uparrow\rangle$ dark state.

Nonetheless, we are able to do a probabilistic state readout by repeating the experiments many times and recording the average number of photons collected per experiment [82]. Normally, this method would be highly sensitive to the total efficiency of our detection system, which can drift slightly over the course of a day due to alignment or power fluctuations. To overcome this, we alternate between σ^+ and σ^- detection light on subsequent trials. This allows us to extract the populations by comparing the number of photons detected on σ^+ trials to σ^- trials, and the detection efficiency factors out of the equations. If we collect n_+ total photons on σ^+ detection cycles, and n_- total photons on σ^- detection cycles, the populations are:

$$P(|\downarrow\rangle) = \frac{n_-}{n_+ + n_-}, \qquad P(|\uparrow\rangle) = \frac{n_+}{n_+ + n_-} \tag{4.1}$$

where n_- (n_+) represents the average number of photons collected on σ_- (σ_+) trials.

These equations can be thought of as solutions to the following linear equation:

$$\begin{pmatrix} n_+ \\ n_- \end{pmatrix} = E_d \begin{pmatrix} M_{\downarrow+} & M_{\uparrow+} \\ M_{\downarrow-} & M_{\uparrow-} \end{pmatrix} \begin{pmatrix} P(|\downarrow\rangle) \\ P(|\uparrow\rangle) \end{pmatrix} \tag{4.2}$$

subject to the condition that $P(|\uparrow\rangle) + P(|\downarrow\rangle) = 1$. Here E_d refers to the (unknown) total single-photon detection efficiency for the system. M_{ij} gives the average number

of photons scattered from an atom in state $|i\rangle$ when illuminated by 493 nm light of polarization σ^j. By dark state arguments given earlier, we see that $M_{\uparrow+} = M_{\downarrow-} = 0$. As mentioned earlier $M_{\downarrow+} = M_{\uparrow-} = 2.8$ is the average number of photons scattered by an ion in the bright state before being pumped dark. Of course, the solution to this set of equations is trivial, and the linear algebra approach is not necessary for finding the result given in Eqn. 4.1. This approach will be useful later this chapter, however, in thinking about how state detection is performed in the D manifold.

We implement this state detection by applying alternating σ^+ or σ^- light for 1.5 μs after each experiment. Light is collected using a 0.6 NA microscope objective and sent to an APD with 70% quantum efficiency at 493 nm. As shown in Fig. 4.5(b), this allows us to read out the state of the atom with 98% fidelity. Although the probabilistic nature of the readout requires us to run more experiments per point than for Yb to get the same uncertainties, the actual detection cycle is 200x faster, allowing experiments to be run much more quickly. For fast experiments, where data collection is limited by state detection times, this does not result in a significant slowdown in data collection rate. For longer experiments or experiments that are inherently probabilistic, however, the probabilistic nature of this detection has a much harsher effect on how quickly scans can be run.

4.2.3 S State Qubit Rotations

The laser we use to generate 355 nm laser for Raman rotations in Yb is a Spectra Physics Vanguard laser that generates 355 nm light as the third harmonic

of a 1064 nm Nd:YVO4 source. This system also generates light as the second harmonic at 532 nm, which is a convenient wavelength for driving Raman transitions in Ba. The energy splitting of the Ba qubit is smaller than the bandwidth of many commercial AOMs, thus we do not need to exploit the large bandwidth of this mode locked laser to drive transitions. Rather, we can simply apply two RF frequencies with a beat note equal to the qubit splitting directly to the AOMs. As with Yb, copropagating beams from a single AOM can be used to drive carrier rotations, but a non-copropagating geometry must be used to address the vibrational sidebands.

As in Yb, the phase of this rotation can be controlled by setting the phase of the beat note. Most of the frequency sources in our lab are direct digital synthesizers, which are not phase referenced to the experiment in any way. If the Raman AOM RF is supplied by one of these free-running frequency sources, the phase of the rotation with respect to the experimental cycle will be random shot-to-shot. As long as the Raman beams are the only element in the experiment that reference the qubit phase, this is not a problem, since the DDS beat note effectively serves as the qubit clock to which all subsequent Raman operations will be phase referenced.

For the ion-photon experiments discussed in the next chapter, there is a phase written onto the atom that is referenced to the photon detection time. This requires the use of frequency sources whose beat note can be phase referenced to the experimental cycle (or better yet, to the photon detection signal from an APD). This can be accomplished by using an arbitrary waveform generator (AWG) that can put out a frequency timed to an external trigger as the RF source. Because AWGs have slow update times, we typically maintain the ability to switch between

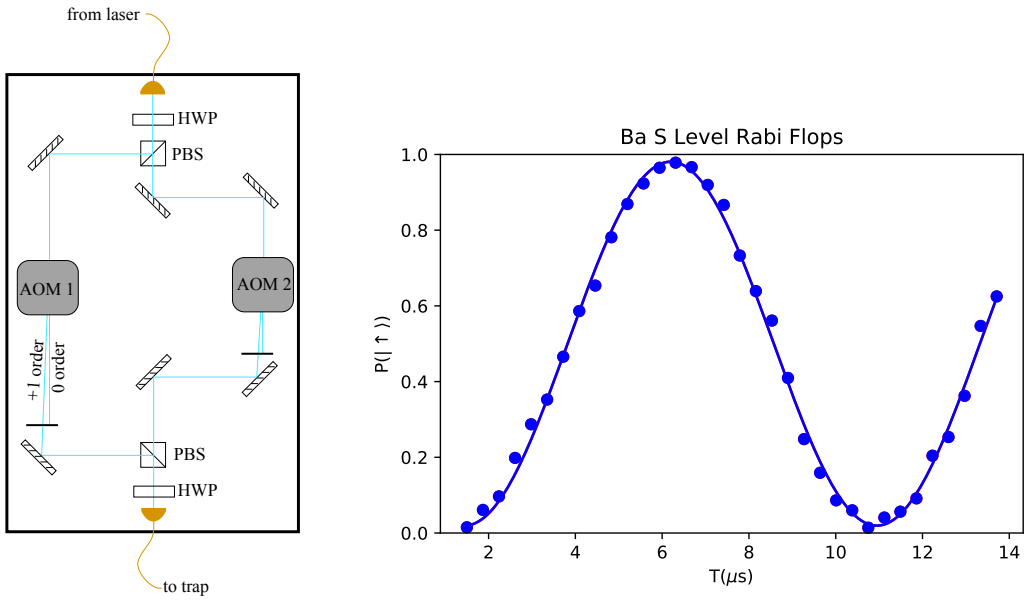

(a) (b)

Figure 4.5: (a) Schematic of the σ table used to switch σ^+ and σ^- beams on and off. At the top, light comes in from the 493 nm laser table. It is sent through a half wave plate (HWP) to control the division of power at the subsequent polarizing beamsplitting cube (PBS). This splits the beam into two orthogonal polarizations that are each sent through their own AOM. The first order outputs of these AOMs are recombined on another PBS and then recoupled to another fiber to be sent to the trap. At the output of that fiber is another set of wave plates to ensure the polarization at the ion is circular for each beam. (b) Rabi flops in the S-State manifold of Ba after driving Raman rotations for time T with co-propagating 532 nm beams.

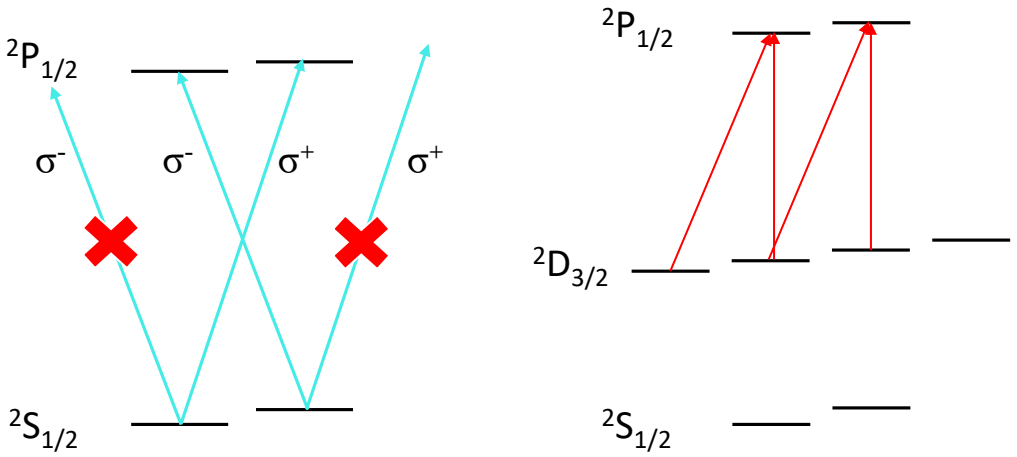

(a) (b)

Figure 4.6: (a) σ initialization and detection scheme for the S state in $^{138}Ba^+$. Note that each state is dark to one of the applied 493 nm polarizations. (b) State initialization into the $m_J = +3/2$ D state in $^{138}Ba^+$. σ^+ and π 650 nm light as well as all polarizations of 493 nm light are applied to the ion so that $m_J = +3/2$ is the only stable dark state.

the two types of frequency sources, using an AWG when the experiment requires it and a DDS otherwise.

4.3 $^{138}Ba^+$ D State Toolkit

There are several factors that make the $^2D_{3/2}$ level appealing for performing quantum operations. Its 80 s lifetime [116] is much longer than conceivable quantum

operations, and its 3:1 branching ratio from the $6P_{1/2}$ state is sizable, providing fast rates of pumping into or exciting out of this level. Additionally, the 650 nm line is spectrally distant from the 493 nm line that addresses the S state, allowing many D state operations to be performed without affecting population in the Ba qubit states. This will contribute to the purity of many of the photonic experiments seen in the next chapter.

4.3.1 D State Initialization

As shown in Fig. 4.1, the $5^2D_{3/2}$ state of $^{138}Ba^+$ consists of four Zeeman sublevels. Because these Zeeman levels are not well separated in frequency, we rely on applying different polarizations to address different lines, just as we do in the S state. σ^+ and σ^- polarizations are produced using a polarization table for 650 nm light similar to the one shown in Fig. 4.5(a). We also have a dedicated beam traveling perpendicular to the B field to apply π polarized light to the ion by sending in light polarized along the B field direction.

State initialization into the D manifold can be achieved by simply switching off the 650 nm light and leaving on all polarizations of 493 nm light [100]. We are able to further pump into the $m_J = +3/2$ stretch state by also applying σ^+ and π polarizations of 650 nm light as shown in Fig. 4.6(b).

4.3.2 D State Detection

While state preparation in the D manifold is very similar to the S state implementation, readout is much more difficult. This is because with four sublevels, there is not a single bright state for each applied polarization. Just as in the S state, we wish to perform state detection by applying some polarization of 650 nm light at the end of each experiment and recording how many photons we collect on average before the ion is pumped dark. We are still collecting 493 nm photons, and the 493 nm cooling beam is left on at all times to repump population out of the S levels. We can then compare the average number of photons collected from the different applied polarizations of 650 nm detect light to solve for the D state populations.

It may at first seem impossible to deduce our populations using this method given the fact that there are four states, and we only have three polarizations of light that we can apply. That is, by analogy to Equation 4.2, the equation

$$\begin{pmatrix} n_+ \\ n_- \\ n_\pi \end{pmatrix} = E_d \begin{pmatrix} M_{-3/2,+} & M_{-1/2,+} & M_{+1/2,+} & M_{+3/2,+} \\ M_{-3/2,-} & M_{-1/2,-} & M_{+1/2,-} & M_{+3/2,-} \\ M_{-3/2,\pi} & M_{-1/2,\pi} & M_{+1/2,\pi} & M_{+3/2,\pi} \end{pmatrix} \begin{pmatrix} P(|-3/2\rangle) \\ P(|-1/2\rangle) \\ P(|+1/2\rangle) \\ P(|+3/2\rangle) \end{pmatrix} \tag{4.3}$$

does not have a unique solution. Here, we assume that we do not know the detection efficiency E_d and we impose the condition $\sum P(|m_J\rangle) = 1$. As before, n_ϵ represents the average number of photons collected from trials with detection polarization ϵ, and $M_{i,\epsilon}$ gives the average number of photons an ion in the state $|m_J = i\rangle$ scatters

before being pumped dark by 650 nm light of polarization ϵ.

We resolve this by noting that applying $\sigma^{\pm}$ and π light at the same time produces an equation that is linearly independent from the individual polarizations. This is because for a $J = 3/2 \rightarrow J = 1/2$ transition, there are two dark states for any polarization of applied light. For σ^{+}, σ^{-}, and π light, both of these states are stationary states of the system even when a magnetic field is applied to impose a Zeeman splitting between the levels. For combinations of $\sigma^{\pm}$ and π light, however, only one dark state is a stationary state, and the other is a superposition of different Zeeman levels. If the detunings of the π and σ beams are not set to be the same, this superposition is not stable and quickly evolves to a bright state. Because this mechanism of pumping out of the dark state is not present in either $\sigma^{\pm}$ or π equations, the $\sigma^{\pm} - \pi$ combinations are linearly independent.

Thus, the populations can be found with the equation

$$\begin{pmatrix} n_{+} \\ n_{-} \\ n_{\pi} \\ n_{+\pi} \\ n_{-\pi} \end{pmatrix} = E_d \begin{pmatrix} M_{-3/2,+} & M_{-1/2,+} & M_{+1/2,+} & M_{+3/2,+} \\ M_{-3/2,-} & M_{-1/2,-} & M_{+1/2,-} & M_{+3/2,-} \\ M_{-3/2,\pi} & M_{-1/2,\pi} & M_{+1/2,\pi} & M_{+3/2,\pi} \\ M_{-3/2,+\pi} & M_{-1/2,+\pi} & M_{+1/2,+\pi} & M_{+3/2,+\pi} \\ M_{-3/2,-\pi} & M_{-1/2,-\pi} & M_{+1/2,-\pi} & M_{+3/2,-\pi} \end{pmatrix} \begin{pmatrix} P(|-3/2\rangle) \\ P(|-1/2\rangle) \\ P(|+1/2\rangle) \\ P(|+3/2\rangle) \end{pmatrix} \tag{4.4}$$

where $\pm\pi$ refers to the combination of $\sigma^{\pm}$ and π light. With the unknown E_d and the normalization condition, a solution for the populations is still under-constrained. This allows us to add an additional term: a static background count rate C_b.

$$\begin{pmatrix} n_+ \\ n_- \\ n_\pi \\ n_{+\pi} \\ n_{-\pi} \end{pmatrix} = E_d \begin{pmatrix} M_{-3/2,+} & M_{-1/2,+} & M_{+1/2,+} & M_{+3/2,+} & 1 \\ M_{-3/2,-} & M_{-1/2,-} & M_{+1/2,-} & M_{+3/2,-} & 1 \\ M_{-3/2,\pi} & M_{-1/2,\pi} & M_{+1/2,\pi} & M_{+3/2,\pi} & 1 \\ M_{-3/2,+\pi} & M_{-1/2,+\pi} & M_{+1/2,+\pi} & M_{+3/2,+\pi} & 1 \\ M_{-3/2,-\pi} & M_{-1/2,-\pi} & M_{+1/2,-\pi} & M_{+3/2,-\pi} & 1 \end{pmatrix} \begin{pmatrix} P(|-3/2\rangle) \\ P(|-1/2\rangle) \\ P(|+1/2\rangle) \\ P(|+3/2\rangle) \\ C_b \end{pmatrix} \tag{4.5}$$

This equation gives a unique solution for the populations as well as C_b and E_d. This solution, as well as a derivation of the values of the M matrix, is given in Appendix B. This allows us to perform readout on the state of the ion in the D manifold of Ba by performing the experiment many times and at the end of each experiment, applying one of the 5 possible detection polarizations, building statistics on the values of n_ϵ. Our solution stipulates that populations sum to one, but we do not have enough free parameters to also demand that each population fall into the range [0,1]. It is common, then, for our analysis of states near 0 or 1 to fluctuate outside this physical regime. Some results of this D state detection are shown in Fig. 4.7.

4.3.3 D State Rotations

The same 532 nm light that is used to drive Raman rotations in the S state of Ba can also be used to drive transitions between different D state levels. Whereas the 532 nm light is red detuned from both the $P_{1/2}$ and $P_{3/2}$ levels for transitions between S levels, it is blue detuned of both transitions from the D levels.

(a)

650 nm detection light polarization	Atomic State: -3/2	-1/2	1/2	3/2
σ^+	6.6	5.4	0	**0**
σ^-	0	0	5.4	**6.6**
π	0	6	6	**0**
σ^+ and π	13.3	12.6	11.4	**0**
σ^- and π	0	11.4	12.6	**13.3**

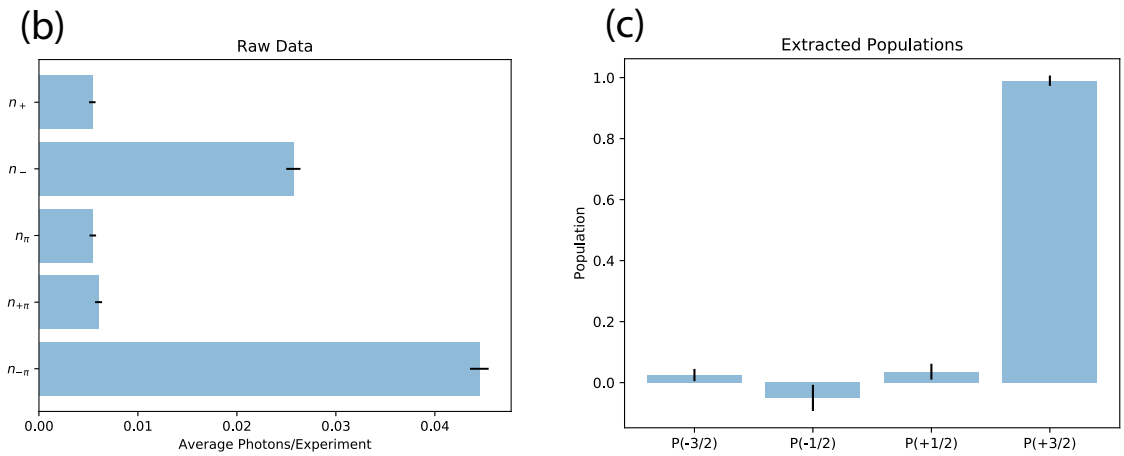

Figure 4.7: (a) Table giving the values of $M_{i,\epsilon}$. (b) Raw data from state detection after pumping to the $|-3/2\rangle$ edge state. These values should correspond to the highlighted last column of the table in (a), scaled by our detection efficiency, and with a background offset. (c) Populations calculated from the raw data presented in (b).

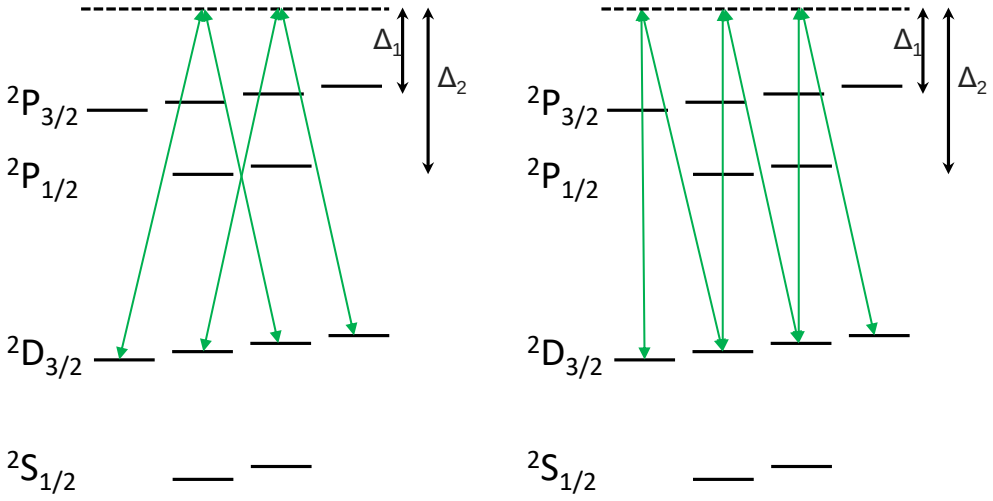

(a) (b)

Figure 4.8: Two types of Raman transitions that can be driven in the D manifold of Ba using 532 nm light. (a) Using only σ light we can drive transitions between the states as two disconnected 2-level systems. For these transitions the beat note on the Raman beams must be set to twice the splitting between adjacent Zeeman levels, or $\frac{8}{5}\mu_B B_z$ (b) Using σ and π light we can drive transitions between all 4 levels. Here the Raman beat note is set to the energy splitting between adjacent Zeeman levels: $\frac{4}{5}\mu_B B_z$. Both types of transitions involve coupling to the $P_{3/2}$ levels at detuning Δ_1 and to the $P_{1/2}$ levels at detuning Δ_2.

As shown in Fig. 4.8, there are two different types of transitions that can be driven with 532nm light. The first kind of transition can be driven with two σ lines with an energy splitting of $\frac{8}{5}\mu_B B_z/h$. Here μ_B is the Bohr magneton, B_z is the magnetic field in the z-direction, and h is Plank's constant. This drives transitions with $\Delta m_J = 2$ between $|-3/2\rangle \leftrightarrow |+1/2\rangle$ and $|-1/2\rangle \leftrightarrow |+3/2\rangle$. Fig. 4.9 shows Rabi flopping on this transition.

The second type of transition we can drive in the D manifold uses σ and π polarizations with a beat note splitting equal to $\frac{4}{5}\mu_B B_z/h$ to drive transitions between adjacent Zeeman states with $\Delta m_J = 1$. Unlike the simple Rabi flopping that occurs on driven 2-level systems, the dynamics of this 4-level system are more complicated. Theoretical curves and actual data of population over time for initialization into one of the edge states are shown in Fig. 4.9.

4.4 Multi-Species Gates on Ba-Yb chains

Critical to realizing a quantum network architecture with $^{138}Ba^+$ as communication qubits and $^{171}Yb^+$ qubits used for local storage and processing is the ability to reliably transfer information between these two species. The primary gate that we are interested in performing is a SWAP interaction to transfer the remote entanglement generated in a pair of Ba ions onto nearby Yb ions. This gate can be achieved either with concatenated Mølmer-Sørensen gates [101], or directly using a Cirac-Zoller gate [4].

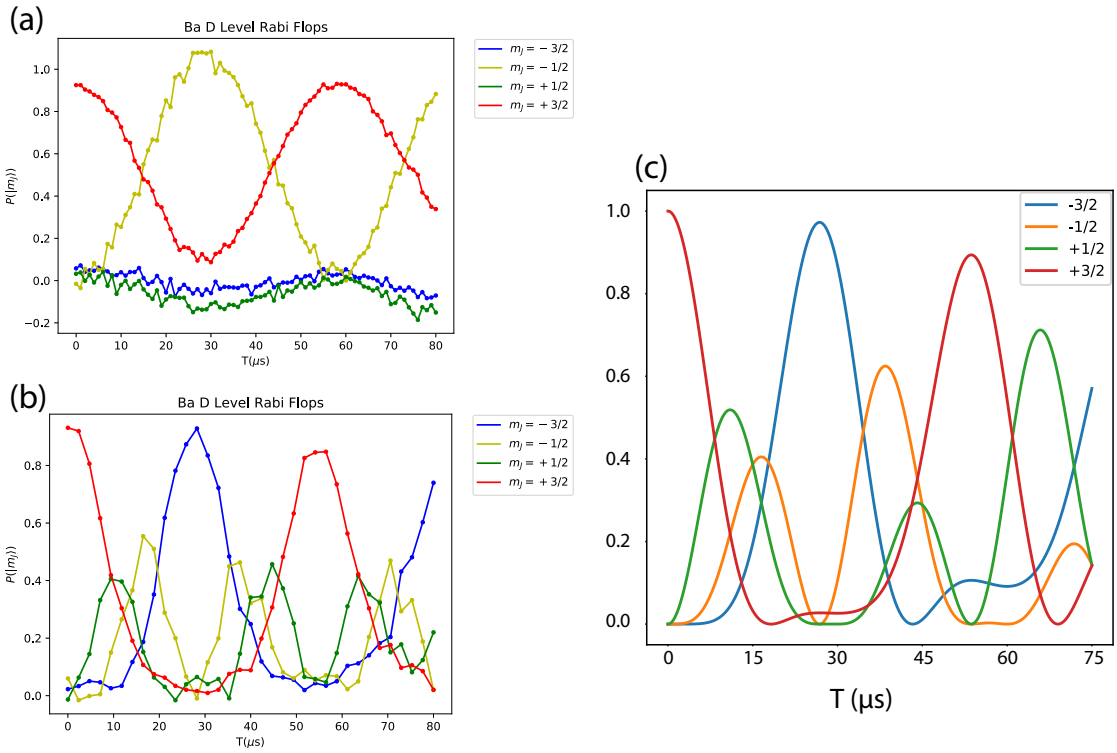

Figure 4.9: (a) Raman transitions driving Rabi flops between $|-1/2\rangle \leftrightarrow |+3/2\rangle$ states in the D manifold of $^{138}Ba^{+}$. Small oscillations on $|-3/2\rangle$ and $|+1/2\rangle$ populations are due to impure polarizations in the 650 nm detection light. (b) Raman transitions at $\frac{4}{5}\mu_B/h$ driving population between all Zeeman levels. Results from both (a) and (b) come from copropagating Raman beams. (c) QuTiP simulations of evolution shown in (b). Couplings have not been optimized to match our polarizations. Rabi rate was set to match experimental results.

4.4.1 Mølmer-Sørensen Gates on Ba-Yb chains

Because it does not require ground state cooling, the MS gate is a natural choice for performing this quantum state mapping. A multi-species MS gate has been demonstrated between Be^+ and Mg^+ ions [101] using two Raman lasers for the two elements. A similar configuration allows us to perform Mølmer-Sørensen gates on chains consisting of one $^{138}Ba^+$ and one $^{171}Yb^+$ ion [82]. We implement this gate by applying the MS interaction described in chapter 2 on $^{171}Yb^+$ using 355 nm light and on $^{138}Ba^+$ using 532 nm light These beams have equal, symmetric detunings from the red and blue vibrational sidebands. Extensive details on the experimental concerns for performing and calibrating this gate are provided in Ref. [65].

The results from these experiments are plotted in Fig. 4.10, and the fidelity of this gate was 0.60. We attribute this error to a high heating rate of $\dot{\bar{n}} = 5$ ms^{-1} in the blade trap that was used for this result. Recently we have been moving to 4-rod traps, whose simple design and large structure tend to result in heating rates $\dot{\bar{n}} \sim 0.1$ ms^{-1}.

4.4.2 Cirac Zoller Gate on Ba-Yb Chains

We would like to demonstrate a full SWAP operation between Ba and Yb, but an implementation of this operation with MS gates requires that two gates be performed sequentially. Our fidelity of F=0.6 is prohibitively low to meaningfully achieve this with MS gates, so instead we chose to use a Cirac Zoller interaction to perform the SWAP gate. This type of gate, also referred to as quantum logic

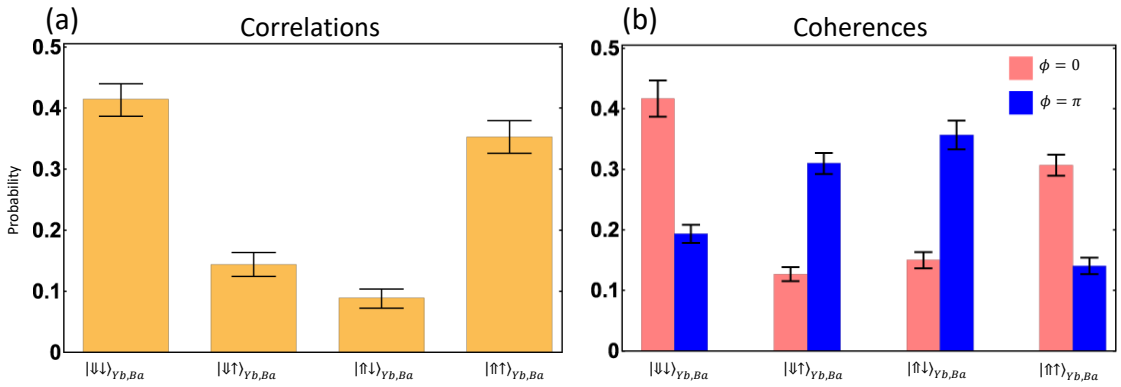

Figure 4.10: Experimental results for Mølmer-Sørensen gate on Ba-Yb chains. (a) Z-basis correlations between Ba and Yb spin states. (b) Coherences in x-basis obtained by performing a $\pi/2$ pulse on both qubits. Phase of the rotation on the Yb ion was scanned. We expect to see parity switch as we scan this phase.

spectroscopy, has also been demonstrated in mixed species chains [98].

We are interested in mapping the state of a Ba ion onto a nearby Yb ion. To implement this we trap one $^{138}Ba^{+}$ and one $^{171}Yb^{+}$ and use EIT cooling to put the atoms in their vibrational ground state. We then initialize the Yb ion into the state $|\Downarrow\rangle$ and we prepare Ba into some state $(\alpha|\downarrow\rangle + \beta|\uparrow\rangle)$. The full state of the Ba-Yb-phonon system can then be written as

$$\psi_{Ba}\psi_{Yb}\psi_n = (\alpha|\downarrow\rangle + \beta|\uparrow\rangle)(|\Downarrow\rangle)(|0\rangle). \tag{4.6}$$

Next we can use 532 nm light to apply a red sideband π pulse on the Ba ion. This pulse drives the transition $|\uparrow\rangle|0\rangle \rightarrow |\downarrow\rangle|1\rangle$ on the Ba-phonon state, but does not couple to the state $|\downarrow\rangle|0\rangle$. The effect of this pulse, then, is to take the quantum information from the Ba ion and write it onto the phonon number state:

$$\psi_{Ba}\psi_{Yb}\psi_n = (|\downarrow\rangle)(|\Downarrow\rangle)(\alpha|0\rangle + \beta|1\rangle). \tag{4.7}$$

Following this, a RSB π pulse can be applied on the Yb^{+} ion to drive population on $|\Downarrow\rangle|1\rangle \rightarrow |\Uparrow\rangle|0\rangle$ to write the quantum information onto the Yb qubit. The final state of the system after the second RSB pulse is

$$\psi_{Ba}\psi_{Yb}\psi_n = (|\downarrow\rangle)(\alpha|\Downarrow\rangle + \beta|\Uparrow\rangle)(|0\rangle), \tag{4.8}$$

completing the SWAP operations as desired. A graphical representation of this gate and results from the experiment are shown in Fig. 4.11 and demonstrate that we are able to transfer the state of the Ba atom onto the Yb qubit. The need for

lengthy EIT cooling before every experiment, however, may limit the usefulness of this protocol for integration with probabilistic photonic experiments.

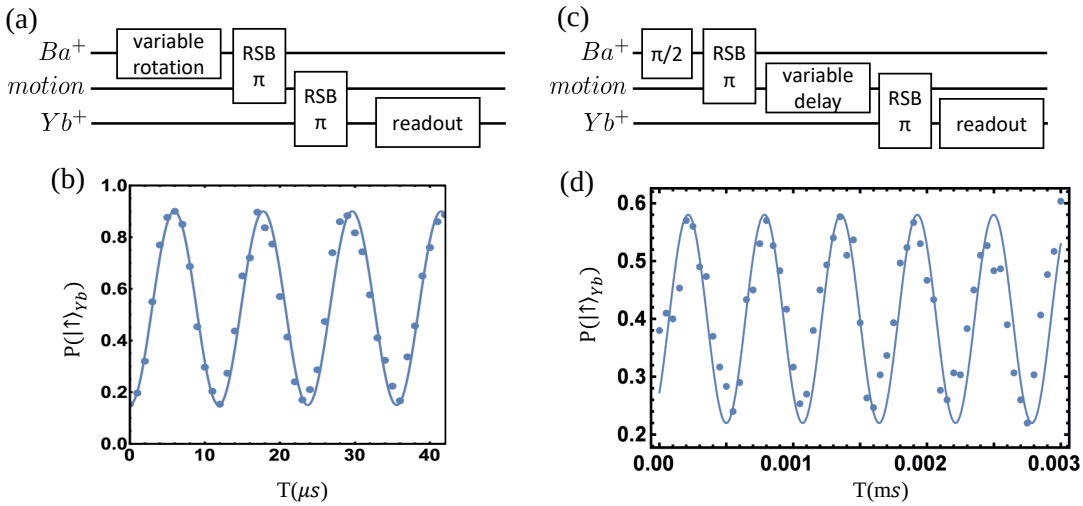

Figure 4.11: (a) Experimental sequence for the CZ SWAP gate. The RSB operations address both spin and motion as described in Chapter 2. We see here that the qubit is briefly written directly onto the phonon before being moved to Yb. This is in contrast with the MS gate which avoids writing quantum information onto phonons. (b) Experimental data for the experiment shown in (a) where the state of the Ba ion is read out on the Yb ion after performing the SWAP operation. The horizontal axis gives the time of the variable rotation applied to the Ba^+ ion. (c) In order to show phase control over this experiment, we apply a variable delay while the qubit is stored in the phonon mode. (d) Experimental results for experiment shown in (c). Ramsey fringes at 1.8 MHz agree well with the measured trap frequency.

Chapter 5: Networking Experiments with Ba

As discussed throughout this work, generating flying photons that are entangled with local memory qubits is an essential component of quantum networking and is of great interest for quantum communication and distributed quantum computing applications [23, 117, 118]. In the mixed species quantum information network architecture we have proposed [82], the primary role of the Ba ion is to generate these photons for distributing remote entanglement between separate ion traps. Now that we have shown a full toolkit for manipulating quantum information in the $^{138}Ba^{+}$ ion, we wish to demonstrate ion-photon entanglement on this platform.

Due to the level structure of $^{138}Ba^{+}$, the simplest method of generating ion-photon generation is to use a polarization qubit and collect 493 nm light about an axis perpendicular to the B-field. In previous works we have implemented this by first pumping a single Ba^{+} ion to the $|\downarrow\rangle$ state. Next, a weak pulse of σ^{+} polarized light was applied to excite $\sim 10\%$ of the population to the $^{2}P_{1/2}\,|m_J = +1/2\rangle \equiv |e\rangle$ state. This 5 ns pulse was generated using the same AOM that is used for state initialization and detection, and the low excitation probability was used to help prevent double excitations. From here, there are two possible decay paths back to the S manifold; the ion can decay back to the $|\downarrow\rangle$ state emitting a σ^{+} polarized

photon or to the $|\uparrow\rangle$ state producing a π polarized photon. This results in ion-photon entanglement as discussed in Chapter 2.

493 nm photons were collected through a 0.6 NA lens and their polarization was read out using a polarizing beamsplitter and a pair of single photon detectors as shown in Fig. 5.2(a). We additionally perform state readout on the Ba qubit using methods described in the previous chapter. Results from this experiment are plotted in Fig. 5.1, and show that we create an entangled Bell state with fidelity $F \geq 0.86$ [82]. In the next section, we go into detail to evaluate and eliminate some of the sources of error that limited this fidelity.

Much of my work has centered examining the sources of error that limit the fidelity of this entanglement and altering our ion-photon entanglement protocol to mitigate or eliminate these errors. For instance, all correlations between the local and flying qubits are destroyed if the atom is re-excited after a photon is collected, thus the purity of the atom as a single-photon source is critical for the fidelity of the ion-photon entanglement [119]. Moreover, for non-zero collection angles, the atomic decays do not perfectly map onto experimental polarizations, limiting the fidelity of ion-photon entanglement [120]. The following sections will discuss the effects of these sources of error in detail and demonstrate methods for reducing them by exciting with and collecting different colors of light, and by applying a custom aperture to maximize collected light while keeping polarization mixing errors low. Another source of error resulting from uncontrolled phase evolution during our detection window is examined and a method for eliminating it is demonstrated in Appendix C.

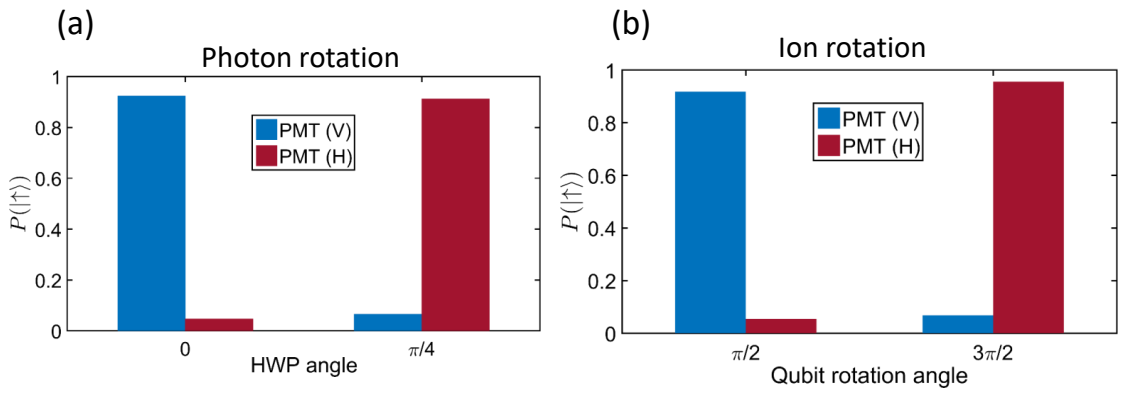

Figure 5.1: Results from the Ba entanglement experiment with 493 nm excitation. (a) No rotations performed on the state of the ion, correlations observed between the state of the ion and the photon in the Z basis. HWP angle of $\pi/4$ corresponds to a π rotation of the photon qubit, reversing the correlations. (b) Here the HWP was set to perform a $\pi/2$ rotation on the state of the photon and a $\pi/2$ Raman pulse was performed on the ion to demonstrate correlations in an orthogonal basis.

5.1 Double Excitations

First we will examine the effects of double excitations on the fidelity of ion-photon entanglement experiments. We assume that such an experiment is trying to produce a maximally entangled Bell state between the ion and the photon by collecting emitted photons from a specific excited state $|e\rangle$. For probabilistic photon collection, there are two mechanisms by which double excitations can introduce errors. In the first mechanism, the first photon emitted by the atom is collected, but the second photon is not collected. In this mechanism, the second excitation destroys the entanglement between the first photon and the state of the atom. The second mechanism describes a situation where the first photon is not collected but the second photon is collected. This situation still produces entanglement between the ion and the collected photon, but if the second excitation prepared the ion in the incorrect $6P_{1/2}$ Zeeman level, that entanglement will have correlations opposite of those intended, introducing errors into the fidelity of the desired Bell state. If the second excitation still prepares the atom in $|e\rangle$, the expected ion-photon entanglement is still produced.

In the previous section we showed ion-photon entanglement with $^{138}Ba^{+}$ by first pumping into $|\downarrow\rangle$ and exciting the atom to $|e\rangle$ with light at 493 nm [82]. Because this scheme uses the same line for excitation and collection light, it is susceptible to both types of double excitation errors. These can be mitigated with a fast pulse of excitation light $T_p << \tau_e$ where T_p is the excitation pulse time and τ_e is the excited state lifetime [91]. Alternatively, the atom can be weakly excited with

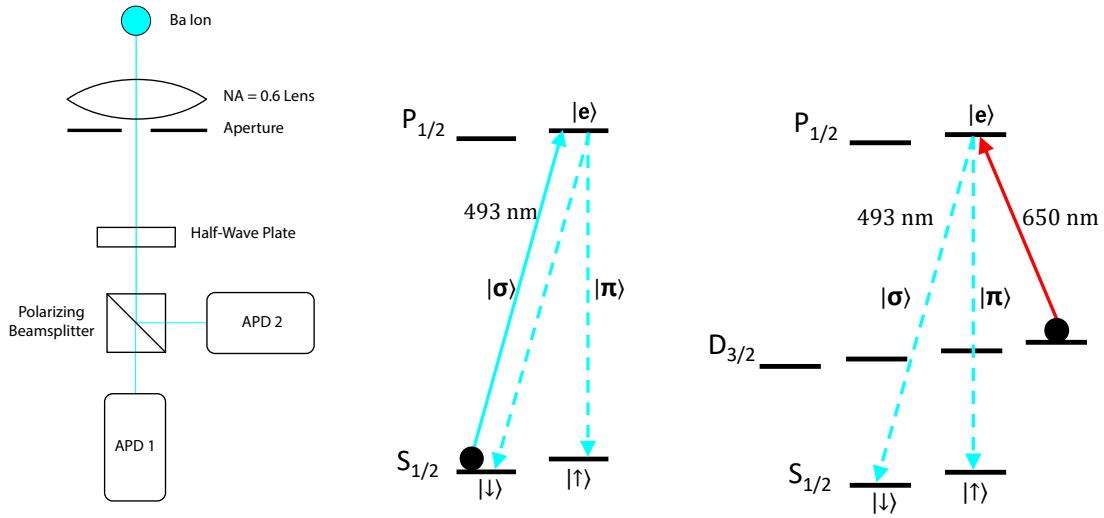

(a) (b) (c)

Figure 5.2: (a) Sketch of the setup used to collect light and analyze the polarization of photonic qubits. Light is collected by a NA = 0.6 lens and then directed through a half-wave plate that can perform x-rotations on the polarization of the qubit. Next is a polarizing, beam-splitting cube and a pair of APDs to detect the photon's polarization in the z-basis. (b) Energy level scheme for $^{138}Ba^{+}$ ion-photon entanglement with 493 nm excitation. (c) Energy levels for $^{138}Ba^{+}$ ion-photon entanglement with 650 nm excitation.

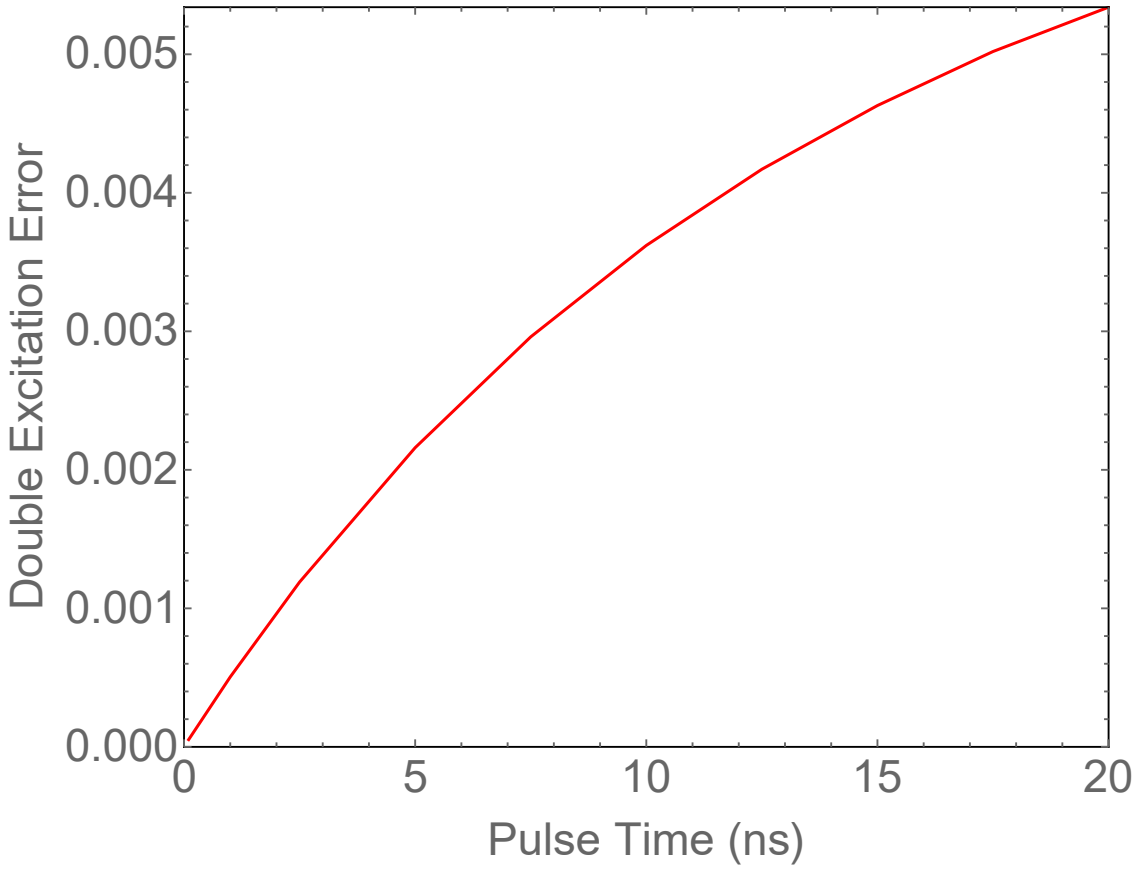

Figure 5.3: Double excitation errors when exciting from a stretch state in the D manifold of $^{138}Ba^{+}$, plotted as a function of pulse time assuming a Rabi rate of $\Omega = \pi/T_p$. Note that even for pulses of order $T_p \sim \tau_e$ the double excitation error is low.

probability P_e such that the probability of double excitations scales as ${P_e}^2$ [121]. This was the approach used in the previous chapter. Weak excitation also reduces the overall success rate of the experiment, however, and forces a harsh trade-off between entanglement generation rate and fidelity. In the limit of long pulses, the experimental repetition rate R_{we} and the maximum fidelity F_{max} are given by

$$R_{we} = R_b * P_e, \quad F_{max} = 1 - \frac{1}{2}P_e, \tag{5.1}$$

where R_b is the base rate of ion-photon entanglement for unit excitation probability.

To avoid the difficulties caused by weak excitation and to eliminate the second mechanism of double excitation errors by ensuring single 493 nm photon emission, it has been proposed [100,122] to prepare the Ba atom in the low-lying $5D_{3/2}$ manifold. A similar method of using seperate excitation and collection lines has been implemented for Ca^+ ions as well [71]. Barium's $5D_{3/2}$ level has several advantageous properties for photonic applications. It has a lifetime of 80 s [116], which is longer than conceivable quantum operations. Additionally, its 3:1 branching ratio from the $6P_{1/2}$ state is larger than in most ions, providing fast pumping times. Importantly, the 650 nm excitation line is off-resonant from the 493 nm collected photons, thus once a photon has been collected there can be no further excitation events, completely eliminating the first mechanism for double excitations. This scheme does not render the ion-photon entanglement immune to the second mechanism of double excitation errors, but favorable branching ratios and Clebsch-Gordan coefficients do serve to suppress these errors. It has been shown [100] that by pumping to one of

the edge states in the D manifold $m_J = \pm 3/2$, even in the limit of $T_p >> \tau_e$, double excitations only introduce an error of 11%.

To examine how the second mechanism of double excitation errors limits our fidelity in the regime where $T_p \sim \tau_e$, we perform a Bloch equation calculation on the evolution of the system's state during and after the pulse, keeping track of whether the resulting S-state population comes from decays from the correct P-state ($|e\rangle$). Our results are plotted in Fig. 5.3 and show that for 650 nm excitation, high fidelity entanglement does not require $T_p << \tau_e$. This significantly relaxes the technological requirements for the experiment, since pulses $T_p \sim \tau_e = 10.5$ ns can be created with a CW source and acousto-optic (AO) or electro-optic (EO) intensity modulators. The experiments presented in this paper are performed with 10 ns pulses generated by an AO modulator, contributing an error of 0.004.

5.2 Pure Single Photons from 650 nm Excitation

The ability to generate pure single photons is at the core of many quantum optics applications such as quantum cryptography [123], quantum repeaters [124], quantum random number generation [125], and distributed quantum computing [126]. In addition to fundamental interest in single photon production, we wish to demonstrate the efficiency of our system as a single photon source to verify that we do not suffer from the first type of double excitation errors [127].

To show this, a $^{138}Ba^{+}$ ion is pumped into the $m_J = +3/2$ edge state $5D_{3/2}$ by applying all polarizations of 493 nm light and σ^{+} and π polarizations of 650 nm

light. Next, a 10 ns pulse of σ^- polarized light is applied to excite the atom to $|e\rangle$ (see Fig. 5.2(c)). 493 nm decay photons are then collected by an $NA = 0.6$ microscope objective and directed to a Hanbury Brown-Twiss type setup as shown in Fig. 5.2(a). To avoid collecting light from the pumping cycle the APDs are gated closed except for a 200 ns window around the 650 nm pulse.

The normalized second-order autocorrelation function after integrating for 18 hours is plotted in Fig. 5.4(a). No background subtraction was applied. The strong suppression of the $\tau = 0$ peak demonstrates the effectiveness of our system as a single-photon source. In Fig. 5.4(b) we present our calculated $g^{(2)}(\tau = 0)$ as a function of the integration window. We report our value of $g^{(2)}(0) = (8.1 \pm 2.3) \times 10^{-5}$ using a 30 ns integration window. This window was chosen to provide sufficient photons to have a low uncertainty and is large enough to include 97% of our collected photons as shown in the red curve of Fig. 5.4(b). This gives 12 ± 3 coincidence events around $\tau = 0$ and 149145 ± 386 coincidence events in the side peaks. This result represents the lowest value ever recorded for a source of indistinguishable photons [122] and is consistent with the lowest value reported in any system of $g^{(2)}(0) = (7.5 \pm 1.6) \times 10^{-5}$ in a solid state experiment [128].

Dark counts on our detectors limit us to $g^{(2)}(0) \geq 4 \times 10^{-5}$. The mechanism by which dark counts limit our $g^{(2)}(0)$ involves registering a single dark count on one detector within the same window as we register a bright count on the other detector. For this experiment we used a 30 nm window and our detectors have a 10 s^{-1} dark count rate, thus the probability of registering a dark coincidence given a single bright click is $P_{bd} = 3 \times 10^{-7}$. This value is compared to the probability of

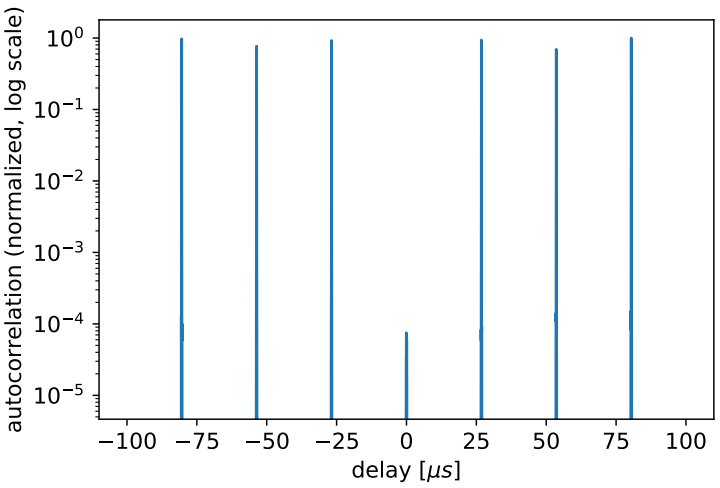

(a)

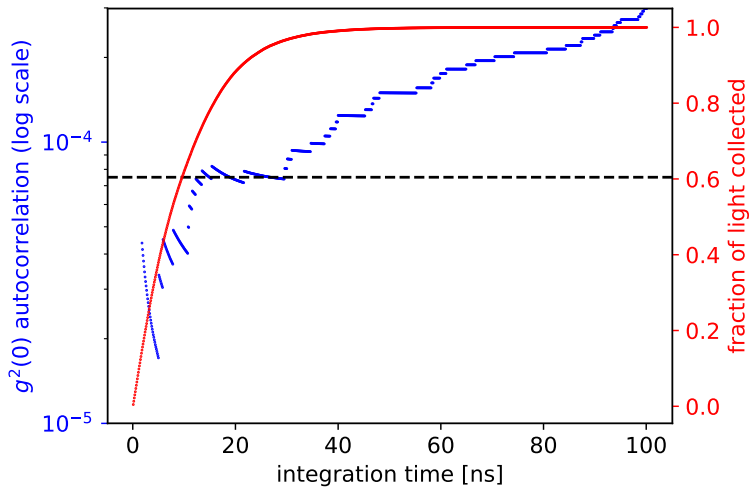

(b)

Figure 5.4: (a) Normalized second-order autocorrelation function. 26 μs peak spacing corresponds to experimental repetition rate. Strong suppression of $\tau = 0$ peak demonstrates purity of single photon source. (b) Calculated $g^{(2)}(0)$ value (blue) and fraction of light collected (red) plotted as functions of integration time. Dashed line represents the lowest reported $g^{(2)}(0)$ value [128].

registering a bright count on different detectors on subsequent trials. This is given by the probability of collecting a single photon on a given detector on a single trial:

$$P_t = 0.5 \cdot p_e \cdot p_{493} \cdot \Omega_o/4\pi \cdot p_c \cdot e_q = 0.007. \tag{5.2}$$

Here 0.5 accounts for the beamsplitter and must be included to account for the fact that we only accept coincidence events corresponding to clicks on two different detectors. p_e is the probability of exciting the atom to the $P_{3/2}$ level, $p_{493} = 0.76$ is the probability that an atom in the $P_{3/2}$ level emits a 493 nm photon, $\Omega_o/4\pi = 0.1$ gives the fraction of the solid angle that the objective collects, p_c gives the remaining collection efficiency of the system and is primarily limited by our coating which has 40% loss at 493 nm. $e_q = 0.7$ is the quantum efficiency of the detector. The limit on $g^{(2)}(0)$, then is given by $P_{bd}/P_t = 4 \times 10^{-5}$.

We attribute the remaining t=0 counts to observed transient light leakage through our 493 nm AO modulators. This source of error was mitigated in our experiment by adding a delay after initialization, decreasing the overall repetition rate of the experiment, but to eliminate it compleately it seemed that we would have to wait for ~ 1 ms, which would make the experiment prohibitively slow. This rate of multi-photon generation limits the contribution of the first mechanism of double excitation errors to a negligible value of $\leq 4 \times 10^{-5}$.

5.3 Atomic Decay Polarizations

As discussed in Chapter 3, trapped ions can be entangled with various degrees of freedom of an emitted photon including polarization, frequency, or photon number [46, 121]. While frequency qubits are generally more robust against propagation through fibers, a polarization qubit can be easily manipulated and detected, making it preferable for many applications [129]. Additionally, it has been shown [130] that polarization qubits can be converted to time-bin qubits for implementation into long-distance networks. There are two different schemes for generating entanglement between an ion's internal state and the polarization state of an emitted photon. One is to collect σ^+ and σ^- photons from atomic decays that subtract or add one quanta of angular momentum. When collected along the atom's quantization axis, these photons map to right and left handed circularly polarized light [91, 131]. This method generally requires filtering of any π polarized photons corresponding to $\Delta m_J = 0$ decays by coupling the collected light into an optical fiber [84]. Another method [83, 121] is to collect photons from π and σ^+ (σ^-) decays. For this scheme, photons are collected along an axis perpendicular to the atom's quantization axis, such that π and σ^+ (σ^-) photons map onto two orthogonal linear polarizations V and H. For both methods, however, the polarization mappings are only exact directly along the specified axis. To perform experiments in the lab, light must be collected over some non-zero solid angle given by the collection optics, leading to errors in the resulting ion-photon entanglement.

Consider a single atom with a quantization axis from an external magnetic field

pointing in the z-direction undergoing spontaneous emission. The emitted photon can carry angular momentum of $\Delta m_Z = +1, 0, \text{or } -1$ quanta, and we will refer to these as σ^+, π, and σ^- events respectively. The radiation patterns resulting from these decays are also referred to as $\boldsymbol{\sigma^+}$, $\boldsymbol{\pi}$, and $\boldsymbol{\sigma^-}$ radiation patterns and can be represented by [52]:

$$\boldsymbol{\pi} = \boldsymbol{\chi_{1,0}}(\theta, \phi) \times \hat{r} = i\sqrt{\frac{3}{8\pi}}\sin(\theta)\hat{\theta} \tag{5.3}$$

$$\boldsymbol{\sigma^+} = \boldsymbol{\chi_{1,1}}(\theta, \phi) \times \hat{r} = ie^{i\phi}\sqrt{\frac{3}{16\pi}}(\cos\theta\hat{\theta} + i\hat{\phi}) \tag{5.4}$$

$$\boldsymbol{\sigma^-} = \boldsymbol{\chi_{1,-1}}(\theta, \phi) \times \hat{r} = ie^{-i\phi}\sqrt{\frac{3}{16\pi}}(\cos\theta\hat{\theta} - i\hat{\phi}) \tag{5.5}$$

where $\boldsymbol{\chi_{lm}}(\theta, \phi)$ are the normalized spherical harmonic vectors.

Now we look at the case of light collected along the x-axis from a $P_{1/2} \rightarrow S_{1/2}$ decay such as the decay in $^{138}Ba^+$ shown in Fig. 5.2(c) where the atom's spin was initially aligned with the magnetic field direction. After a decay the resultant atom-photon state is given by $\Psi_r = \frac{1}{\sqrt{2}}(\sqrt{P_\sigma}\,|\downarrow \sigma\rangle + \sqrt{P_\pi}\,|\uparrow \pi\rangle)$ where P_σ and P_π are the probabilities of the collected photon coming from a σ or π decay. Here we are interested in mapping σ^+ (or σ^-) and π onto $\hat{H} = \hat{\phi}$ and $\hat{V} = \hat{\theta}$ photons to create the desired maximally entangled state $\Psi_d = \frac{1}{\sqrt{2}}(|\downarrow H\rangle + |\uparrow V\rangle)$. There are two potential sources of error. First, as implied in Fig. 5.5(a), for large collection angles $P_\sigma \neq P_\pi$. Second, as shown in Fig. 5.5(b), for $\theta \neq \pi/2$, we have $\sigma^+ \neq H$. We calculate these errors by first integrating the spatial distributions of σ and π decays to find P_σ and P_π as a function of the half-angle of our collection optics α_1. Next we numerically integrate the H and V components of the σ decays to find $P_{\sigma H}$ and $P_{\sigma V}$, the probabilities that a collected σ photon is detected as H or V. This gives

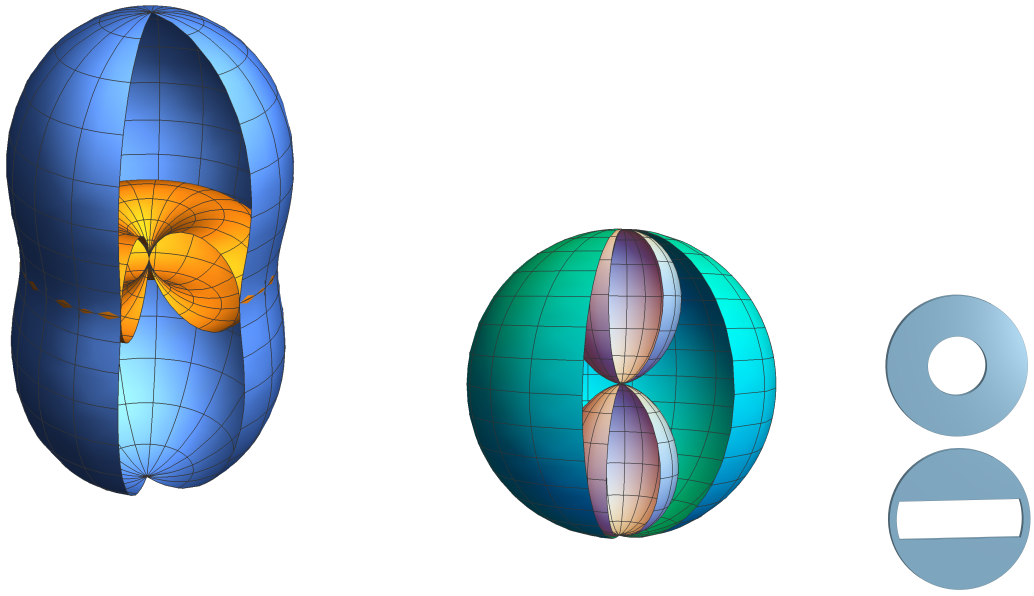

(a) (b) (c)

Figure 5.5: (a) Spatial distribution of light from a σ decay (blue) and π decay (yellow). The blue curve is normalized to have twice the total probability as the yellow curve. This satisfies the condition that decays into free space be isotropic. Note that at $\theta = \pi/2$ there are equal amounts of σ and π decays. (b) Decomposition of the σ decay radiation pattern from (a) into horizontal (cyan) and vertical (light blue) linear polarization components. At $\theta = \pi/2$ there is no vertical component, and at $\theta = 0$ or π, the vertical and horizontal components are equal as the light is circularly polarized. (c) Two types of apertures are analyzed in this experiment. Circular stop (top) used to restrict collection angle while maintaining a circular aperture. Horizontal stop (bottom) used to restrict collection in the θ (vertical) direction while allowing full collection in ϕ (horizontal) direction.

us our resultant state Ψ_r with the photon state in the $\{H, V\}$ basis:

$$\Psi_r(\alpha_1) = \sqrt{P_{\sigma H}}\,|\downarrow H\rangle + \sqrt{P_{\sigma V}}\,|\downarrow V\rangle + \sqrt{P_{\pi}}\,|\uparrow V\rangle\,. \tag{5.6}$$

We now define the error $\epsilon = 1 - F = 1 - |\,\langle\Psi_d|\Psi_r\rangle\,|^2$ where F is the fidelity of the ion-photon entanglement. This error is plotted as a function of solid angle collected in the blue curve of Fig. 5.6(a).

This result shows that as larger numerical apertures are used to improve entanglement generation rates, the fidelity of the ion-photon entanglement will suffer. Note that both types of errors increase for light farther from $\theta = \pi/2$, but are independent of ϕ. This suggests that it may be possible to achieve a more favorable trade-off between rate and fidelity by blocking light in the θ direction. To analyze this possibility, we consider light collected by a lens with collection half-angle α_1 with a set of stops that limit collection in the vertical direction to $\theta = \pi/2 \pm \alpha_2$ where $\alpha_2 \leq \alpha_1$ (Fig. 5.5(c)). The error calculations are then repeated and the results are plotted in Fig. 5.6(a) as a function of total solid angle collected for a variety of values of α_1. The results confirm that the horizontal stops provide a favorable trade-off between light collection and fidelity.

5.4 Ba Ion-Photon Entanglement with 650 nm Excitations

To experimentally examine the effects of polarization mixing described in the previous section, we perform ion-photon entanglement using a single trapped $^{138}Ba^{+}$ atom. First, we use 650 nm excitation to generate an entangled ion photon pair as

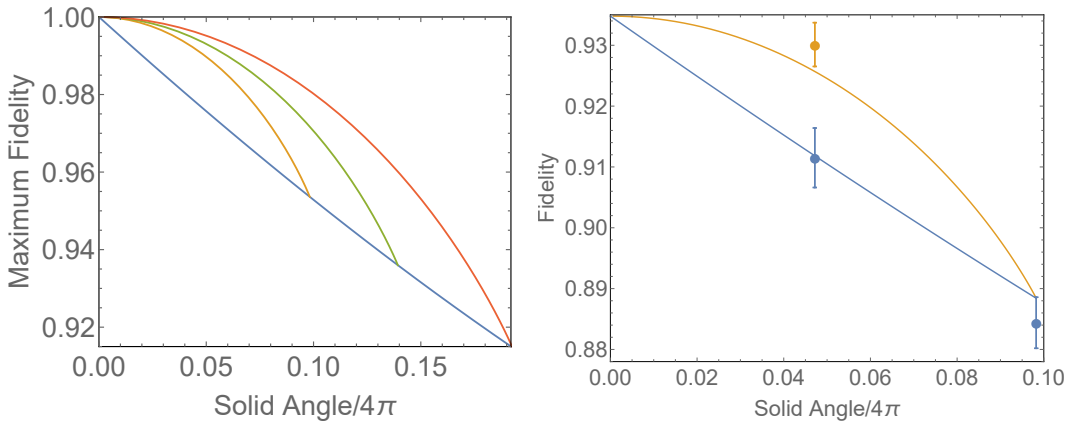

(a) (b)

Figure 5.6: (a) Theoretical scaling between solid angle of collection lens and polarization-mixing errors on ion-photon fidelity. The blue curve represents the scaling for a simple circular aperture. The yellow, green, and red curves give the scaling assuming a fixed circular aperture of NA = 0.6, 0.7, or 0.8 respectively that has light farthest from $\theta = \pi/2$ blocked as by a horizontal aperture. (b) The blue and yellow curves are the theoretical scaling curves from (a) applied to fidelity, including our other sources of error. The blue and yellow points show the data taken with the corresponding apertures applied. The error bars show 1σ uncertainties.

described in Section 5.2.2. For this experiment, we also make use of the half-wave plate that can rotate the photon's polarization before the polarization measurement. Additionally, ion S state rotations and readout are performed using the methods described in [82].

To demonstrate entanglement, we first show correlations between the state of the ion and the photon in the z-basis. This is done by performing no rotations on the ion and analyzing correlations between the ion and photon states as a function of photon rotation angle. Next, correlations in an orthogonal basis, the coherences, are demonstrated by fixing the wave plate angle to rotate the polarization by $\pi/2$ and performing a $\pi/2$ rotation on the atom with a variable phase. These results are plotted in Fig. 5.7 and show an ion-photon entanglement fidelity of $F = 0.884(4)$ when light is collected over the entire 0.6 NA of the lens. Intrinsic polarization mixing for this size of aperture accounts for a fidelity loss of 0.046; we attribute the remaining errors to imperfect state initialization and readout, intensity and phase noise on the Raman beams used to analyze the coherences, and polarization mixing in the collection optics [91]. The analysis from previous sections indicates that errors from double excitations are < 0.004.

To analyze the effects of spatial filtering on ion light, various optical stops were 3D printed to be inserted immediately after the last lens of the microscope objective (see Fig. 5.5(c)). These apertures were designed to block half of the solid angle either symmetrically (circular stops) or in only the θ direction (horizontal stops). After inserting the stops, the amount of light blocked was measured and the entanglement experiments were repeated. The circular stops produced a fidelity of

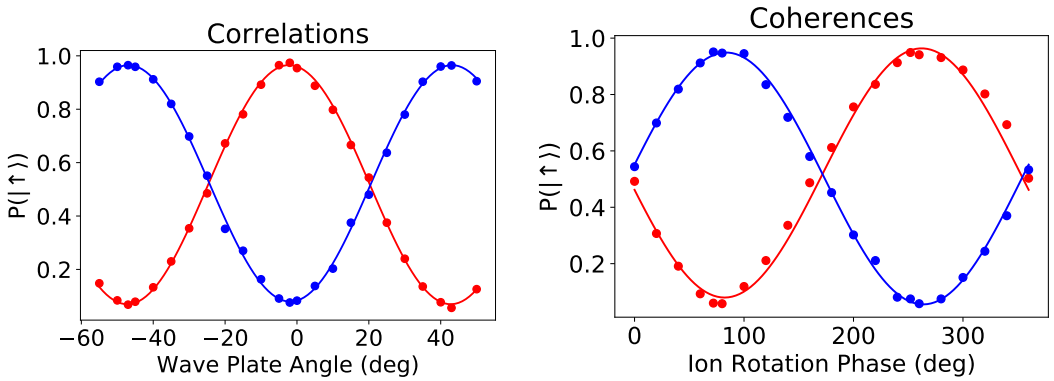

(a) z-basis correlations

(b) x-basis correlations

Figure 5.7: (a) Ion-photon correlation results as a function of wave plate rotation angle. A wave plate angle of θ rotates the qubit by 4θ, thus the 90 degree period. The red (blue) curve shows the probability of finding the ion in the $|\uparrow\rangle$ state when the photon is detected on APD1 (APD2). No stops were used for these experiments. (b) Coherences in the y-basis are taken by setting the half-wave plate to perform a $\pi/2$ rotation on the photon and then applying a $\pi/2$ pulse on the ion with a varying phase.

0.912(5) and the horizontal stops improved this further to 0.930(4). These results are plotted along with the theory curves in Fig. 5.6(b) and confirm that, by taking into consideration the spatial profile of the atomic decays, we can maximize fidelity gained by sacrificing rate.

It should be noted that the spatial mode of the $|\downarrow V\rangle$ term in Eqn. 5.6 is anti-symmetric about the X-Y plane and thus will not couple into the symmetric mode of a single mode optical fiber aligned perpendicular to the B-field [132]. Because fiber coupling is important for a networked architecture [133], this eliminates the largest fundamental source of error for this protocol and makes it an attractive option for generating ion-photon entanglement.

Chapter 6: Outlook

In this work, we have shown all of the necessary ingredients to construct a modular node consisting of a superior Yb memory qubit and visible photon flying qubits from a Ba ion. Going forward, an integrated demonstration of this node, where the state of the visible photon is entangled with the Yb qubit will be a major step. The lower heating rates in the Alice trap, in which the later works presented in this thesis were performed, as well as other small technical improvements related to moving to the new lab will hopefully facilitate the improved local operations that will be necessary for this. Additionally, as I write this we are working on getting a second trap with low heating rates up and running. This should allow for local gates to be performed with higher fidelities.

The total overhead in resources required as we scale our system towards two traps each with two species scales generally quite well. Most of the lasers and electronics can be shared between the two traps. Nonetheless, the requirements for separating, switching, and distributing each beam to the different traps is significant, and as we hope to eventually move beyond two traps we have given considerable thought to how our optics setup can be efficiently scaled. Just as we believe that a modular approach is critical for scaling a quantum computing system, we are also

moving towards a modular architecture for this classical hardware. Fig. 6.1 shows modules for combining and distributing 355/532 nm beams and 399/370 nm beams, with the intent that additional traps will require only that additional modules be added on, avoiding a need for major renovations with every upgrade.

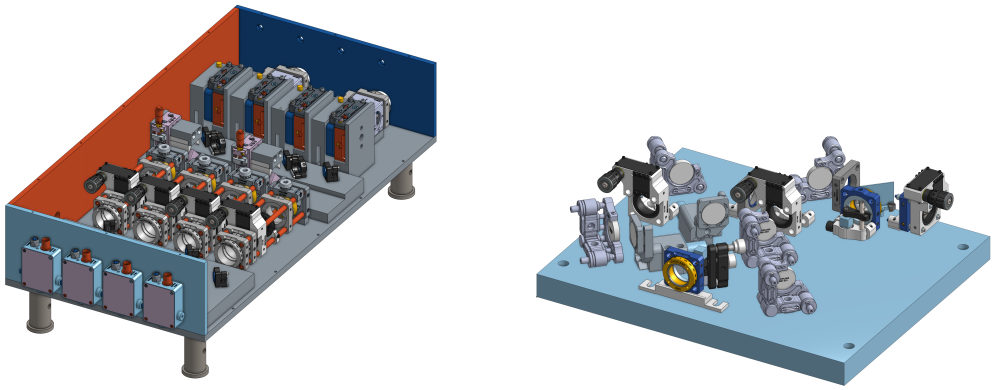

(a) (b)

Figure 6.1: Two types of modular optics boxes designed to allow for easier scaling to more traps. Multiple of these boards can be chained together for scaling to more traps. (a) Compact box for splitting 532 and 355 nm beams into four total beams with individual AOM control, and then combining one beam of each color for each of the two paths to the trap. Fine path length adjustments and wave plates are included in the setup. (b) Schematic of a 399 and 369 nm distribution box designed to combine Yb cooling and ionization light into a single fiber for delivery to a single trap.

Appendix A: Fast Remote Entanglement Without Weak Pulses or Optical Phases

A number of results from NV centers in diamond have been referenced in this thesis, and one method for generating remote entanglement that has been realized on that platform merits particular note. This technique uses an auxiliary memory qubit to generate remote entanglement using a two photon protocol that is insensitive to optical phases, but does not rely on weak excitation and has a rate that scales with the first power of the photon collection probability [134]. With our dual species networks giving us strong isolation between memory qubits and the photon generation process, this protocol might seem like a natural fit for our system. Unfortunately our energy level scheme makes this difficult to implement. Here, I will briefly describe the protocol, then I will show why there is no straightforward way to apply it to our system without a shelving laser, and finally I will discuss how this protocol could be performed with the inclusion of a shelving laser.

The energy level diagram for the NV centers used in the first experimental realization of this protocol [135] is shown in Fig. A.1(a). The photonic degree of freedom utilized in this experiment is photon number in the two channels coming from the individual NV centers. First both NV's are prepared state $\frac{1}{\sqrt{2}}(|\downarrow\rangle + |\uparrow\rangle)$,

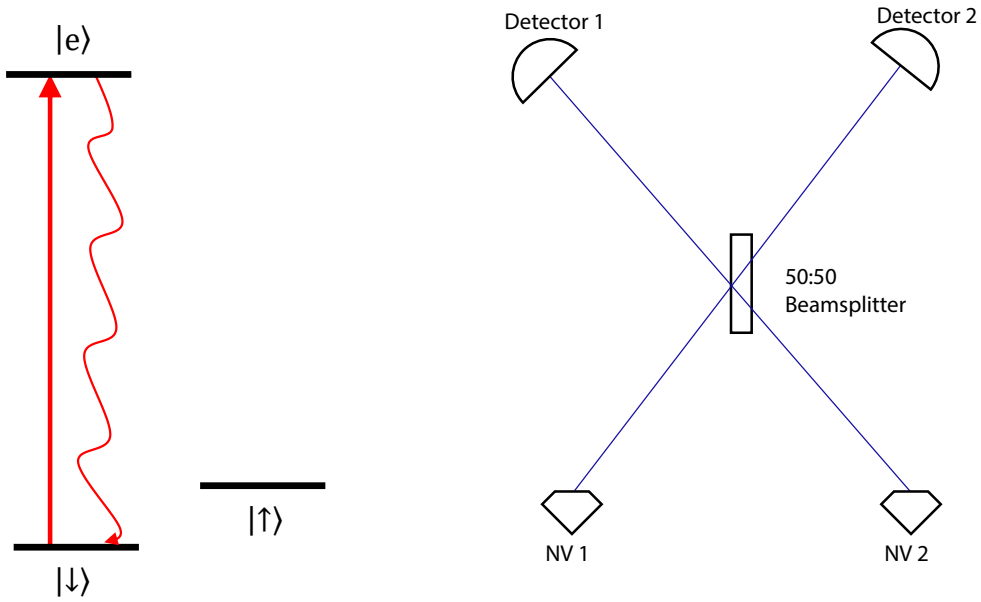

(a) (b)

Figure A.1: (a) Energy level diagram for NV-photon entanglement experiments. It is important for this protocol that the $|\uparrow\rangle$ state be completely disconnected from both the $|\downarrow\rangle \rightarrow |e\rangle$ excitation and decay processes. (b) Hong-Ou-Mandel interferometer used in these experiments. As with some ion experiments, no polarizing beam splitters are required after the 50:50 beam splitter.

and then each is strongly excited on the $|\downarrow\rangle \rightarrow |e\rangle$ line. After the decay this produces the state

$$\frac{1}{2}(|\downarrow\rangle|1\rangle + |\uparrow\rangle|0\rangle)(|\downarrow\rangle|1\rangle + |\uparrow\rangle|0\rangle)$$

$$= \frac{1}{2}(|\downarrow\downarrow\rangle|11\rangle + |\downarrow\uparrow\rangle|10\rangle + |\uparrow\downarrow\rangle|01\rangle + |\uparrow\uparrow\rangle|00\rangle)$$

where $|mn\rangle$ denotes m photons in the first NV's channel and n photons in the second NV's channel. The photons are combined on a Hong-Ou-Mandel interferometer as shown in Fig. 3.1(b). Detection of a single photon heralds the creation of state

$$\frac{1}{\sqrt{3}}(|\downarrow\downarrow\rangle + |\downarrow\uparrow\rangle + |\uparrow\downarrow\rangle) = \sqrt{\frac{2}{3}}\Psi^+ + \frac{1}{\sqrt{3}}|\downarrow\downarrow\rangle$$

where Ψ^+ is the maximally entangled bell state $\Psi^+ = \frac{1}{\sqrt{2}}(|\downarrow\uparrow\rangle + |\uparrow\downarrow\rangle)$. This state is then swapped onto a nearby spectator memory qubit (a nuclear spin in the case of the NV centers). Next these steps are repeated until a second copy of this state is created. Once this has been achieved, it is possible to use local operations within each node as well as classical communication between the nodes to distill these two imperfect bell pairs into a single maximally entangled state [136]. This is achieved in the NV experiment by performing a σ_y rotation on the electron spin, followed by a CNOT gate between the electron and nuclear spins, and then a final a σ_x rotation on the electron. The state of the NV is then read out and detection of $|\downarrow\downarrow\rangle$ heralds the creation of a maximally entangled bell pair on the nuclear spins [135]. This protocol is insensitive to slow optical path length fluctuations, but is sensitive to optical path length fluctuations within a single experiment.

Our system has many of the basic components required for performing this kind of experiment, including the optical link, the ability to perform local opera-

tions, and the local memory qubits that can store information, so it may seem like this would be a natural direction for our experiments to proceed. Unfortunately, this scheme also requires that the $|\uparrow\rangle$ state be entirely removed from the photon generation process. Even if we filter out σ polarized photons to ensure that any collected photons come from $|e\rangle \rightarrow |\downarrow\rangle$ decays, the $|\uparrow\rangle$ may still undergo excitation and decay, acquiring an uncontrolled phase in the process.

To perform this protocol with $^{138}Ba^{+}$, a narrow shelving laser to coherently transfer population to the $5D_{5/2}$ level would be required. Defining $\left|6S_{1/2}m_J = -1/2\right\rangle \equiv |\downarrow\rangle$, $\left|5S_{5/2}m_J = -3/2\right\rangle \equiv |\uparrow\rangle$, and $\left|6P_{1/2}m_J = -1/2\right\rangle \equiv |e\rangle$ would allow for a straightforward application of this protocol assuming that we are able to filter out σ or π polarized light.

Appendix B: $^{138}Ba^{+}$ D-State Detection

For performing state detection on the D manifold of $^{138}Ba^{+}$, it is critical that we know how many photons will be scattered from each state j by each polarization ϵ. These values are the elements $M_{j,\epsilon}$ of the matrix that is used in Equation 4.5.

$$\begin{pmatrix} n_{+} \\ n_{-} \\ n_{\pi} \\ n_{+\pi} \\ n_{-\pi} \end{pmatrix} = E_d \begin{pmatrix} M_{-3/2,+} & M_{-1/2,+} & M_{+1/2,+} & M_{+3/2,+} & 1 \\ M_{-3/2,-} & M_{-1/2,-} & M_{+1/2,-} & M_{+3/2,-} & 1 \\ M_{-3/2,\pi} & M_{-1/2,\pi} & M_{+1/2,\pi} & M_{+3/2,\pi} & 1 \\ M_{-3/2,+\pi} & M_{-1/2,+\pi} & M_{+1/2,+\pi} & M_{+3/2,+\pi} & 1 \\ M_{-3/2,-\pi} & M_{-1/2,-\pi} & M_{+1/2,-\pi} & M_{+3/2,-\pi} & 1 \end{pmatrix} \begin{pmatrix} P(|-3/2\rangle) \\ P(|-1/2\rangle) \\ P(|+1/2\rangle) \\ P(|+3/2\rangle) \\ C_b \end{pmatrix} \tag{B.1}$$

These matrix elements are evaluated by performing simulations on the 8-levels of the $^{138}Ba^{+}$ atom and a 9th state keeping track of the average number of 493 nm decays. As discussed in chapter 4, the Zeeman splittings quickly wash out any coherent effects between different levels, and so the simulation tracks only population in each state and no phase information.

The state of the system, then, is expressed as a 9d vector of real numbers where the first 8 terms are the populations in the 8 states in order of increasing energy. The 9th element of the vector is simply a counter for the average number

of 493 nm decays and is always initialized to zero. The effects of light of a given polarization ϵ could be written as a stochastic Markov matrix Q^ϵ whose elements in the top left 8x8 section $Q^\epsilon_{i,j}$ give the probability of atomic population in state i being excited to or decaying to state j. For example, for $\epsilon = \sigma^+$, if we assume all polarizations of 493 nm light are applied with equal intensity,

$$Q^+_{8\text{X}8} = \begin{pmatrix} 0 & 0 & 0 & 0 & 0 & 0 & \frac{1}{3} & \frac{2}{3} \\ 0 & 0 & 0 & 0 & 0 & 0 & \frac{2}{3} & \frac{1}{3} \\ 0 & 0 & 0 & 0 & 0 & 0 & 1 & 0 \\ 0 & 0 & 0 & 0 & 0 & 0 & 0 & 1 \\ 0 & 0 & 0 & 0 & 1 & 0 & 0 & 0 \\ 0 & 0 & 0 & 0 & 0 & 1 & 0 & 0 \\ 0.76\frac{2}{3} & 0.76\frac{1}{3} & 0.24\frac{1}{2} & 0.24\frac{1}{3} & 0.24\frac{1}{6} & 0 & 0 & 0 \\ 0.76\frac{2}{3} & 0.76\frac{1}{3} & 0 & 0.24\frac{1}{6} & 0.24\frac{1}{3} & 0.24\frac{1}{2} & 0 & 0 \end{pmatrix}. \tag{B.2}$$

where the fractions are given by the magnitude of the Clebsch-Gordan coefficients and the decimals are the branching ratios between 493 and 650 nm decays. Note that each row sums to one in order to preserve probability when applied to a normalized population vector. The Q^ϵ matrices are calculated similarly for other polarizations.

The 9th row and column are included to count the total number of 493 nm decays, and therefore do not need to preserve population:

$$Q^{\epsilon} = \begin{pmatrix} & & & \vdots & & & & & 1 \\ & & & \vdots & & & & & 1 \\ & & & \vdots & & & & & 0 \\ \cdots & \cdots & \cdots & Q^{\epsilon}_{8x8} & \cdots & \cdots & \cdots & \cdots & 0 \\ & & & \vdots & & & & & 0 \\ & & & \vdots & & & & & 0 \\ & & & \vdots & & & & & 0 \\ & & & \vdots & & & & & 0 \\ 0 & 0 & 0 & 0 & 0 & 0 & 0 & 0 & 1 \end{pmatrix}. \tag{B.3}$$

The last column is 0 for rows corresponding to P and D state population and 1 for rows corresponding to S state population.

Applying Q^{ϵ} to a state vector represents the evolution of the system by one "step" of decay or excitation. Because these steps may take different amounts of time, there is not a simple analogue to time for this simulation, but because we know that the ion will be quickly pumped into a dark state we are only concerned with the long-time limit of the simulation. This is done by raising Q^{ϵ} to some large power N and applying that to an initial state vector. For N=100 we verify that over 99% of the population is in a dark state regardless of initial state, and the number of photons emitted is given by the last element of the resultant vector.

This allows us to calculate the matrix M:

$$M_{j,\epsilon} = (Q^{\epsilon})^{N} \boldsymbol{\psi_j} \cdot \begin{pmatrix} 0 \\ \vdots \\ 0 \\ 1 \end{pmatrix} \tag{B.4}$$

where $\boldsymbol{\psi_j}$ is the initial state unit vector corresponding to all of the population starting in state j.

These simulations were performed for each polarization, each time with the assumption that the 493 nm intensities were the same for each polarization. In cases where there are two 650 nm polarizations, it was assumed that their intensities were the same as well. The resulting M matrix is:

$$M = \begin{pmatrix} M_{-3/2,+} & M_{-1/2,+} & M_{+1/2,+} & M_{+3/2,+} \\ M_{-3/2,-} & M_{-1/2,-} & M_{+1/2,-} & M_{+3/2,-} \\ M_{-3/2,\pi} & M_{-1/2,\pi} & M_{+1/2,\pi} & M_{+3/2,\pi} \\ M_{-3/2,+\pi} & M_{-1/2,+\pi} & M_{+1/2,+\pi} & M_{+3/2,+\pi} \\ M_{-3/2,-\pi} & M_{-1/2,-\pi} & M_{+1/2,-\pi} & M_{+3/2,-\pi} \end{pmatrix} = \begin{pmatrix} 6.57 & 5.43 & 0 & 0 \\ 0 & 0 & 5.43 & 6.57 \\ 0 & 6.00 & 6.00 & 0 \\ 13.25 & 12.63 & 11.38 & 0 \\ 0 & 11.38 & 12.63 & 13.25 \end{pmatrix}. \tag{B.5}$$

These values can be used with Eqn. B.1 to solve for the populations given the average number of photons collected from each polarization of detection light.

$$P(|-3/2\rangle) = 0.780 + \frac{0.224n_{+} + 0.361n_{-} + 0.004n_{+\pi} - 0.590n_{-\pi}}{-0.052n_{+} - 0.052n_{-} - 1.00n_{\pi} + 0.552n_{+\pi} + 0.552n_{-\pi}} \tag{B.6}$$

$$P(|-1/2\rangle) = -0.280 + \frac{0.433n_+ - 1.018n_- - 0.067n_{+\pi} - 0.652n_{-\pi}}{-0.052n_+ - 0.052n_- - 1.00n_\pi + 0.552n_{+\pi} + 0.552n_{-\pi}} \tag{B.7}$$

$$P(|+1/2\rangle) = -0.280 + \frac{0.433n_- - 1.018n_+ - 0.067n_{-\pi} - 0.652n_{+\pi}}{-0.052n_+ - 0.052n_- - 1.00n_\pi + 0.552n_{+\pi} + 0.552n_{-\pi}} \tag{B.8}$$

$$P(|-3/2\rangle) = 0.780 + \frac{0.224n_- + 0.361n_+ + 0.004n_{-\pi} - 0.590n_{+\pi}}{-0.052n_+ - 0.052n_- - 1.00n_\pi + 0.552n_{+\pi} + 0.552n_{-\pi}} \tag{B.9}$$

These equations all rely on the assumption that population is trapped in the dark state, but the added term for a background offset can somewhat account for impure polarizations. Additionally, in deriving the M matrices, it was assumed that all polarizations had equal intensities. Our sensitivity to this assumption was examined, and it was found that intensity fluctuations of 50% cause populations to change by 1-5 percentage points. In practice, it should be easy to set our intensity with better accuracy than this, and matching the intensities to within 10% causes errors to be $< 1\%$.

Appendix C: Ion Photon Entanglement Phases

In order to demonstrate entanglement between the state of an ion and an emitted photon, it is critical that we keep track of the phase of the entangled state. In Chapter 4, we briefly discussed the different kinds of frequency sources that we can use to drive the AOMs we use for ion rotations in the lab. The most common source we use is a free-running source such as a DDS. The absolute phase of these sources will be random shot-to-shot with respect to both the experimental cycle and to other frequency sources in the lab. As long as all operations are referenced to the frequency source, this is not a problem, and we have even demonstrated how a "master clock" frequency source could be used to perform coherent operations across distant nodes in a large network [137].

For experiments involving a phase that is not controlled by this master clock, however, these free-running frequency sources present a problem. To see an example of this, let us consider the phases during an ion-photon entanglement experiment. For the sake of concreteness, we will consider the protocol used in Ba in Chapter 5, but these results are general enough to be applied to most schemes.

Immediately after the decay, the unnormalized atom-photon state is

$$\Psi(t) = e^{-iE_{|\downarrow\rangle}t/\hbar}\,|\downarrow\rangle\, e^{-i\omega_\sigma t}\,|\sigma\rangle + e^{-iE_{|\uparrow\rangle}t/\hbar}\,|\uparrow\rangle\, e^{-i\omega_\pi t}\,|\pi\rangle \tag{C.1}$$

where $E_{|\downarrow\rangle}$ ($E_{|\uparrow\rangle}$) is the energy of the $|\downarrow\rangle$ ($|\uparrow\rangle$) state, and $\omega_{\sigma/\pi}$ is the frequency of the corresponding decay. Noting that by energy conservation, $E_{|\downarrow\rangle} + \hbar\omega_\sigma = E_{|\uparrow\rangle} + \hbar\omega_\pi$, we see that the relative phase does not evolve while the photon is in flight.

If we are attempting to measure the coherences of this system by looking at correlations in an alternative basis, however, we see a relative phase evolution. For instance, if the photon is found to be in the state $(|\sigma\rangle + |\pi\rangle)$, this projects the ion into the state

$$\Psi(t) = |\downarrow\rangle + e^{-i\Delta\omega t}\,|\uparrow\rangle \tag{C.2}$$

where t=0 is at the time that the photon is detected.

Thus we see that for coherence experiments, the clock starts once the photon is detected. This timing will be random with respect to any free-running oscillator, and so these experiments will require a frequency source that can be externally triggered.

The excitation pulse is timed to the experimental cycle, but this photon detection will occur at some subsequent time given by a convolution of the (typically Gaussian) excitation pulse and the (exponentially decaying) decay profile. For small energy splittings $\Delta\omega \ll \Gamma$, the amount of phase evolution over the spread of photon arrival times is small, and the AWG can be triggered on the experimental cycle. If $\Delta\omega \not\ll \Gamma$, a random phase will be written onto the ion shot-to-shot based on the

photon arrival time. One way to address this would be to timestamp each photon and correct for the phase of the subsequent rotation in post-processing as done in Ref. [138]. Another solution is to trigger the AWG not on the experimental cycle, but rather on the photon arrival time, effectively feeding forward onto the phase of the AWG. This feed-forward technique was implemented for the results discussed in Section 5.2.4.

I will also mention that for Raman rotations, it is the phase of the beatnote, rather than the individual phase from either beam that gets written onto the ion. The disadvantage of this is that in a straightforward application, both AOMs must be driven by AWG channels, increasing the overhead in resources required. The advantage is that it opens up the possibility to use a high frequency DDS around the AOM frequency and to mix in a signal from a single lower frequency AWG at the qubit splitting.

Our results in Section 5.2.4 rely on this method where a 190 MHz DDS signal was split and one arm was mixed with a 5 MHz AWG signal to give the two beams a beatnote with phase controlled by the AWG. The signals were then recombined and sent to a single AOM for the copropagating Raman rotations as shown in Fig. C.1.

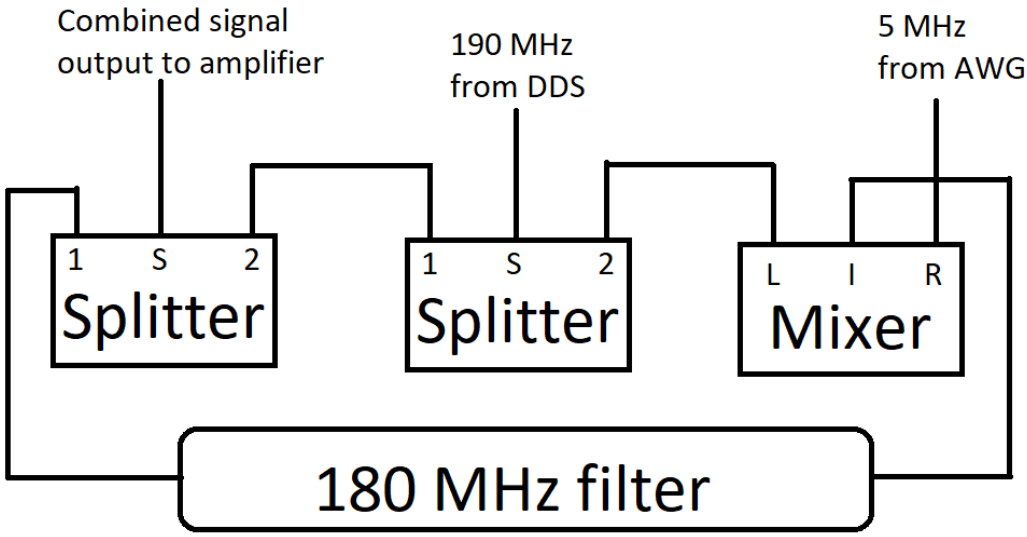

Figure C.1: Setup used to produce the RF drive for the 200 MHZ AOM on the 532 nm Raman beam used for the analysis pulse in Section 5.2.4. This signal should have two tones separated by the qubit splitting $\omega \approx 5$ MHz. It is critical that the phase of this beatnote is controlled by an AWG. We implement this with a DDS at 190 MHz that is split into two arms. The right arm is mixed with the 5 MHz signal from an Agilent 33250A AWG producing outputs at 185 MHz and 195 MHz. This signal is then put through a narrow band filter to remove the sum frequency component. The output of this mixer is combined with the left arm of the original splitter to produce a signal with the desired two tones. The AWG is triggered on a signal from the photon detection. This design allows us to control the beatnote on two ~ 200 MHz beams using only a single channel of a 25 MHz AWG and a DDS.

Bibliography

[1] Richard P. Feynman. Simulating physics with computers. *International Journal of Theoretical Physics*, 21(6):467–488, Jun 1982.

[2] P. W. Shor. Algorithms for quantum computation: discrete logarithms and factoring. In *Proceedings 35th Annual Symposium on Foundations of Computer Science*, pages 124–134, Nov 1994.

[3] Daniel R. Simon. On the power of quantum computation. *SIAM J. Comput.*, 26(5):1474–1483, October 1997.

[4] J. I. Cirac and P. Zoller. Quantum computations with cold trapped ions. *Phys. Rev. Lett.*, 74:4091–4094, May 1995.

[5] C. Monroe, D. M. Meekhof, B. E. King, W. M. Itano, and D. J. Wineland. Demonstration of a fundamental quantum logic gate. *Phys. Rev. Lett.*, 75:4714–4717, Dec 1995.

[6] Serge Haroche and Jean-Michel Raimond. Quantum computing: Dream or nightmare? *Physics Today*, 49:51, Aug 1996.

[7] Peter W. Shor. Scheme for reducing decoherence in quantum computer memory. *Phys. Rev. A*, 52:R2493–R2496, Oct 1995.

[8] A. M. Steane. Error correcting codes in quantum theory. *Phys. Rev. Lett.*, 77:793–797, Jul 1996.

[9] A. D. Córcoles, Easwar Magesan, Srikanth J. Srinivasan, Andrew W. Cross, M. Steffen, Jay M. Gambetta, and Jerry M. Chow. Demonstration of a quantum error detection code using a square lattice of four superconducting qubits. *Nature Communications*, 6:6979 EP –, Apr 2015. Article.

[10] S. Debnath, N. M. Linke, C. Figgatt, K. A. Landsman, K. Wright, and C. Monroe. Demonstration of a small programmable quantum computer with atomic qubits. *Nature*, 536:63, Aug 2016.

[11] Sergio Boixo, Sergei Isakov, Vadim Smelyanskiy, Ryan Babbush, Nan Ding, Zhang Jiang, Michael J. Bremner, John Martinis, and Hartmut Neven. Characterizing quantum supremacy in near-term devices. *Nature Physics*, 14:595–600, 2018.

[12] C. H. Bennett and G. Brassard. Quantum cryptography: Public key distribution and coin tossing. In *Proceedings of IEEE International Conference on Computers, Systems, and Signal Processing*, page 175, 1984.

[13] Artur K. Ekert. Quantum cryptography based on bell's theorem. *Phys. Rev. Lett.*, 67:661–663, Aug 1991.

[14] W. K. Wootters and W. H. Zurek. A single quantum cannot be cloned. *Nature*, 299:802, Oct 1982.

[15] H.-J. Briegel, W. Dür, J. I. Cirac, and P. Zoller. Quantum repeaters: The role of imperfect local operations in quantum communication. *Phys. Rev. Lett.*, 81:5932–5935, Dec 1998.

[16] Chip Elliott. Building the quantum network. *New Journal of Physics*, 4(1):46, 2002.

[17] M Peev, C Pacher, R Alléaume, C Barreiro, J Bouda, W Boxleitner, T Debuisschert, E Diamanti, M Dianati, J F Dynes, S Fasel, S Fossier, M Fürst, J-D Gautier, O Gay, N Gisin, P Grangier, A Happe, Y Hasani, M Hentschel, H Hübel, G Humer, T Länger, M Legré, R Lieger, J Lodewyck, T Lorünser, N Lütkenhaus, A Marhold, T Matyus, O Maurhart, L Monat, S Nauerth, J-B Page, A Poppe, E Querasser, G Ribordy, S Robyr, L Salvail, A W Sharpe, A J Shields, D Stucki, M Suda, C Tamas, T Themel, R T Thew, Y Thoma, A Treiber, P Trinkler, R Tualle-Brouri, F Vannel, N Walenta, H Weier, H Weinfurter, I Wimberger, Z L Yuan, H Zbinden, and A Zeilinger. The secoqc quantum key distribution network in vienna. *New Journal of Physics*, 11(7):075001, 2009.

[18] FangXing Xu, Wei Chen, Shuang Wang, ZhenQiang Yin, Yang Zhang, Yun Liu, Zheng Zhou, YiBo Zhao, HongWei Li, Dong Liu, ZhengFu Han, and GuangCan Guo. Field experiment on a robust hierarchical metropolitan quantum cryptography network. *Chinese Science Bulletin*, 54(17):2991–2997, Sep 2009.

[19] M. Sasaki, M. Fujiwara, H. Ishizuka, W. Klaus, K. Wakui, M. Takeoka, S. Miki, T. Yamashita, Z. Wang, A. Tanaka, K. Yoshino, Y. Nambu, S. Takahashi, A. Tajima, A. Tomita, T. Domeki, T. Hasegawa, Y. Sakai, H. Kobayashi, T. Asai, K. Shimizu, T. Tokura, T. Tsurumaru, M. Matsui, T. Honjo, K. Tamaki, H. Takesue, Y. Tokura, J. F. Dynes, A. R. Dixon, A. W. Sharpe, Z. L. Yuan, A. J. Shields, S. Uchikoga, M. Legré, S. Robyr, P. Trinkler, L. Monat, J.-B. Page, G. Ribordy, A. Poppe, A. Allacher, O. Maurhart,

T. Länger, M. Peev, and A. Zeilinger. Field test of quantum key distribution in the tokyo qkd network. *Opt. Express*, 19(11):10387–10409, May 2011.

[20] Juan Yin, Yuan Cao, Yu-Huai Li, Sheng-Kai Liao, Liang Zhang, Ji-Gang Ren, Wen-Qi Cai, Wei-Yue Liu, Bo Li, Hui Dai, Guang-Bing Li, Qi-Ming Lu, Yun-Hong Gong, Yu Xu, Shuang-Lin Li, Feng-Zhi Li, Ya-Yun Yin, Zi-Qing Jiang, Ming Li, Jian-Jun Jia, Ge Ren, Dong He, Yi-Lin Zhou, Xiao-Xiang Zhang, Na Wang, Xiang Chang, Zhen-Cai Zhu, Nai-Le Liu, Yu-Ao Chen, Chao-Yang Lu, Rong Shu, Cheng-Zhi Peng, Jian-Yu Wang, and Jian-Wei Pan. Satellite-based entanglement distribution over 1200 kilometers. *Science*, 356(6343):1140–1144, 2017.

[21] Timothy J. Proctor, Paul A. Knott, and Jacob A. Dunningham. Multiparameter estimation in networked quantum sensors. *Phys. Rev. Lett.*, 120:080501, Feb 2018.

[22] Charles H. Bennett and David P. DiVincenzo. Quantum information and computation. *Nature*, 404:247, Mar 2000. Review Article.

[23] H. J. Kimble. The quantum internet. *Nature*, 453:1023 EP –, Jun 2008.

[24] L.-M. Duan, M. D. Lukin, J. I. Cirac, and P. Zoller. Long-distance quantum communication with atomic ensembles and linear optics. *Nature*, 414:413, Nov 2001. Article.

[25] C. Monroe and J. Kim. Scaling the ion trap quantum processor. *Science*, 339(6124):1164–1169, 2013.

[26] Liang Jiang, Jacob M. Taylor, Anders S. Sørensen, and Mikhail D. Lukin. Distributed quantum computation based on small quantum registers. *Phys. Rev. A*, 76:062323, Dec 2007.

[27] Yuan Liang Lim, Sean D. Barrett, Almut Beige, Pieter Kok, and Leong Chuan Kwek. Repeat-until-success quantum computing using stationary and flying qubits. *Phys. Rev. A*, 73:012304, Jan 2006.

[28] Alexandre Blais, Ren-Shou Huang, Andreas Wallraff, S. M. Girvin, and R. J. Schoelkopf. Cavity quantum electrodynamics for superconducting electrical circuits: An architecture for quantum computation. *Phys. Rev. A*, 69:062320, Jun 2004.

[29] Kenneth R. Brown, Jungsang Kim, and Christopher Monroe. Co-designing a scalable quantum computer with trapped atomic ions. *Npj Quantum Information*, 2:16034, Nov 2016. Review Article.

[30] C. Monroe, R. Raussendorf, A. Ruthven, K. R. Brown, P. Maunz, L.-M. Duan, and J. Kim. Large-scale modular quantum-computer architecture with atomic memory and photonic interconnects. *Phys. Rev. A*, 89:022317, Feb 2014.

[31] Norbert M. Linke, Dmitri Maslov, Martin Roetteler, Shantanu Debnath, Caroline Figgatt, Kevin A. Landsman, Kenneth Wright, and Christopher Monroe. Experimental comparison of two quantum computing architectures. *Proceedings of the National Academy of Sciences*, 114(13):3305–3310, 2017.

[32] Vladimir Aksyuk, S Arney, Nagesh Basavanhally, D.J. Bishop, C.A. Bolle, C.C. Chang, R Frahm, A Gasparyan, J.V. Gates, Rejomon George, C.R. Giles, Jungsang Kim, Paul Kolodner, T.M. Lee, David T. Neilson, C Nijander, Carl Nuzman, Mark Paczkowski, A.R. Papazian, and M.E. Simon. 238 x 238 micromechanical optical cross connect. 15:587 – 589, 05 2003.

[33] David P. DiVincenzo. The physical implementation of quantum computation. *Fortschritte der Physik*, 48(9-11):771–783, 2000.

[34] J. I. Cirac and P. Zoller. A scalable quantum computer with ions in an array of microtraps. *Nature*, 404:579, Apr 2000.

[35] J. Q. You, J. S. Tsai, and Franco Nori. Scalable quantum computing with josephson charge qubits. *Phys. Rev. Lett.*, 89:197902, Oct 2002.

[36] L.-M. Duan and H. J. Kimble. Scalable photonic quantum computation through cavity-assisted interactions. *Phys. Rev. Lett.*, 92:127902, Mar 2004.

[37] Janus H. Wesenberg, Klaus Mølmer, Lars Rippe, and Stefan Kröll. Scalable designs for quantum computing with rare-earth-ion-doped crystals. *Phys. Rev. A*, 75:012304, Jan 2007.

[38] D. Copsey, M. Oskin, F. Impens, T. Metodiev, A. Cross, F. T. Chong, I. L. Chuang, and J. Kubiatowicz. Toward a scalable, silicon-based quantum computing architecture. *IEEE Journal of Selected Topics in Quantum Electronics*, 9(6):1552–1569, Nov 2003.

[39] W. M. Kaminsky and S. Lloyd. *Scalable Architecture for Adiabatic Quantum Computing of Np-Hard Problems*, pages 229–236. Springer US, Boston, MA, 2004.

[40] D.E. Chang, L.M.K. Vandersypen, and M. Steffen. Nmr implementation of a building block for scalable quantum computation. *Chemical Physics Letters*, 338(4):337 – 344, 2001.

[41] Hai-Rui Wei and Fu-Guo Deng. Scalable photonic quantum computing assisted by quantum-dot spin in double-sided optical microcavity. *Opt. Express*, 21(15):17671–17685, Jul 2013.

[42] V. Giovannetti, D. Vitali, P. Tombesi, and A. Ekert. Scalable quantum computation with cavity qed systems. *Phys. Rev. A*, 62:032306, Aug 2000.

[43] R. Versluis, S. Poletto, N. Khammassi, B. Tarasinski, N. Haider, D. J. Michalak, A. Bruno, K. Bertels, and L. DiCarlo. Scalable quantum circuit and control for a superconducting surface code. *Phys. Rev. Applied*, 8:034021, Sep 2017.

[44] Robin Blume-Kohout, Carlton M. Caves, and Ivan H. Deutsch. Climbing mount scalable: Physical resource requirements for a scalable quantum computer. *Foundations of Physics*, 32(11):1641–1670, Nov 2002.

[45] D. Kielpinski, C. Monroe, and D. J. Wineland. Architecture for a large-scale ion-trap quantum computer. *Nature*, 417:709, Jun 2002.

[46] L. Luo, D. Hayes, T.A. Manning, D.N. Matsukevich, P. Maunz, S. Olmschenk, J.D. Sterk, and C. Monroe. Protocols and techniques for a scalable atom–photon quantum network. *Fortschritte der Physik*, 57(11-12):1133–1152, 2009.

[47] P. T. H. Fisk, M. J. Sellars, M. A. Lawn, and G. Coles. Accurate measurement of the 12.6 ghz "clock" transition in trapped /sup 171/yb/sup +/ ions. *IEEE Transactions on Ultrasonics, Ferroelectrics, and Frequency Control*, 44(2):344–354, March 1997.

[48] S. Olmschenk, D. N. Matsukevich, P. Maunz, D. Hayes, L.-M. Duan, and C. Monroe. Quantum teleportation between distant matter qubits. *Science*, 323(5913):486–489, 2009.

[49] M. Roberts, P. Taylor, S. V. Gateva-Kostova, R. B. M. Clarke, W. R. C. Rowley, and P. Gill. Measurement of the $^2S_{1/2}$−$^2D_{5/2}$ clock transition in a single $^{171}\mathrm{yb}^+$ ion. *Phys. Rev. A*, 60:2867–2872, Oct 1999.

[50] N. Huntemann, C. Sanner, B. Lipphardt, Chr. Tamm, and E. Peik. Single-ion atomic clock with 3×10^{-18} systematic uncertainty. *Phys. Rev. Lett.*, 116:063001, Feb 2016.

[51] C. Langer, R. Ozeri, J. D. Jost, J. Chiaverini, B. DeMarco, A. Ben-Kish, R. B. Blakestad, J. Britton, D. B. Hume, W. M. Itano, D. Leibfried, R. Reichle, T. Rosenband, T. Schaetz, P. O. Schmidt, and D. J. Wineland. Long-lived qubit memory using atomic ions. *Phys. Rev. Lett.*, 95:060502, Aug 2005.

[52] Steven Matthew Olmschenk. *Quantum Teleportation Between Distant Matter Qubits.* PhD thesis, University of Michigan, 2009.

[53] Christopher J. Foot. *Atomic Physics.* Oxford University Press, 2005.

[54] J. J. Curry. Compilation of wavelengths, energy levels, and transition probabilities for ba i and ba ii. *Journal of Physical and Chemical Reference Data*, 33(3):725–746, 2004.

[55] David Lee Hayes. *Remote and Local Entanglement of Ions using Photons and Phonons*. PhD thesis, University of Maryland, 2012.

[56] David J. Jones, Scott A. Diddams, Jinendra K. Ranka, Andrew Stentz, Robert S. Windeler, John L. Hall, and Steven T. Cundiff. Carrier-envelope phase control of femtosecond mode-locked lasers and direct optical frequency synthesis. *Science*, 288(5466):635–639, 2000.

[57] Takunori Taira, Akira Mukai, Yukihiro Nozawa, and Takao Kobayashi. Single-mode oscillation of laser-diode-pumped nd:yvo4 microchip lasers. *Opt. Lett.*, 16(24):1955–1957, Dec 1991.

[58] R. Islam, W. C. Campbell, T. Choi, S. M. Clark, C. W. S. Conover, S. Debnath, E. E. Edwards, B. Fields, D. Hayes, D. Hucul, I. V. Inlek, K. G. Johnson, S. Korenblit, A. Lee, K. W. Lee, T. A. Manning, D. N. Matsukevich, J. Mizrahi, Q. Quraishi, C. Senko, J. Smith, and C. Monroe. Beat note stabilization of mode-locked lasers for quantum information processing. *Opt. Lett.*, 39(11):3238–3241, Jun 2014.

[59] D. Hayes, D. N. Matsukevich, P. Maunz, D. Hucul, Q. Quraishi, S. Olmschenk, W. Campbell, J. Mizrahi, C. Senko, and C. Monroe. Entanglement of atomic qubits using an optical frequency comb. *Phys. Rev. Lett.*, 104:140501, Apr 2010.

[60] David Hucul. *A Modular Quantum System of Trapped Atomic Ions*. PhD thesis, University of Maryland, 2015.

[61] S. R. Jefferts, C. Monroe, A. S. Barton, and D. J. Wineland. Paul trap for optical frequency standards. *IEEE Transactions on Instrumentation and Measurement*, 44(2):148–150, April 1995.

[62] Patricia J. Lee. *Quantum Information Processing with Two Trapped Cadmium Ions*. PhD thesis, University of Michigan, 2006.

[63] D.J. Wineland, C. Monroe, W. M. Itano, D. Leibfried, B. E. King, and D. M. Meekhof. Experimental issues in coherent quantum-state manipulation of trapped atomic ions, 1998.

[64] Anders Sørensen and Klaus Mølmer. Quantum computation with ions in thermal motion. *Phys. Rev. Lett.*, 82:1971–1974, Mar 1999.

[65] Ismail Volkan Inlek. *Multi-Species Trapped Atomic Ion Modules for Quantum Networks*. PhD thesis, University of Maryland, 2016.

[66] Klaus Mølmer and Anders Sørensen. Multiparticle entanglement of hot trapped ions. *Phys. Rev. Lett.*, 82:1835–1838, Mar 1999.

[67] Kazi Rajibul Islam. *Quantum Simulations of Interacting Spin Models with Trapped Ions*. PhD thesis, University of Maryland, 2012.

[68] P. Kómár, E. M. Kessler, M. Bishof, L. Jiang, A. S. Sørensen, J. Ye, and M. D. Lukin. A quantum network of clocks. *Nature Physics*, 10:582, Jun 2014. Article.

[69] Fritz Riehle. Optical clock networks. *Nature Photonics*, 11:25, Jan 2017. Review Article.

[70] B. Tabakov, J. Bell, D. F. Bogorin, B. Bonenfant, P. Cook, L. Disney, T. Dolezal, J. P. O'Reilly, J. Phillips, K. Poole, L. Wessing, and K.-A. Brickman-Soderberg. Towards using trapped ions as memory nodes in a photon-mediated quantum network. volume 10660, pages 10660 – 10660 – 7, 2018.

[71] Matthias Bock, Pascal Eich, Stephan Kucera, Matthias Kreis, Andreas Lenhard, Christoph Becher, and Jürgen Eschner. High-fidelity entanglement between a trapped ion and a telecom photon via quantum frequency conversion. *Nature Communications*, 9(1):1998, 2018.

[72] T. Chanelière, D. N. Matsukevich, S. D. Jenkins, S.-Y. Lan, T. A. B. Kennedy, and A. Kuzmich. Storage and retrieval of single photons transmitted between remote quantum memories. *Nature*, 438:833, Dec 2005.

[73] E. Togan, Y. Chu, A. S. Trifonov, L. Jiang, J. Maze, L. Childress, M. V. G. Dutt, A. S. Sørensen, P. R. Hemmer, A. S. Zibrov, and M. D. Lukin. Quantum entanglement between an optical photon and a solid-state spin qubit. *Nature*, 466:730, Aug 2010.

[74] Kristiaan De Greve, Leo Yu, Peter L. McMahon, Jason S. Pelc, Chandra M. Natarajan, Na Young Kim, Eisuke Abe, Sebastian Maier, Christian Schneider, Martin Kamp, Sven Höfling, Robert H. Hadfield, Alfred Forchel, M. M. Fejer, and Yoshihisa Yamamoto. Quantum-dot spin-photon entanglement via frequency downconversion to telecom wavelength. *Nature*, 491:421, Nov 2012.

[75] Lilian Childress and Ronald Hanson. Diamond nv centers for quantum computing and quantum networks. *MRS Bulletin*, 38(2):134–138, 2013.

[76] D. L. Moehring, P. Maunz, S. Olmschenk, K. C. Younge, D. N. Matsukevich, L.-M. Duan, and C. Monroe. Entanglement of single-atom quantum bits at a distance. *Nature*, 449:68, Sep 2007.

[77] C. Cabrillo, J. I. Cirac, P. García-Fernández, and P. Zoller. Creation of entangled states of distant atoms by interference. *Phys. Rev. A*, 59:1025–1033, Feb 1999.

[78] L. Slodička, G. Hétet, N. Röck, P. Schindler, M. Hennrich, and R. Blatt. Atom-atom entanglement by single-photon detection. *Phys. Rev. Lett.*, 110:083603, Feb 2013.

[79] L.-M. Duan and H. J. Kimble. Efficient engineering of multiatom entanglement through single-photon detections. *Phys. Rev. Lett.*, 90:253601, Jun 2003.

[80] David Lynn Moehring. *Remote Entanglement of Trapped Atomic Ions*. PhD thesis, University of Michigan, 2007.

[81] Shuai Chen, Yu-Ao Chen, Bo Zhao, Zhen-Sheng Yuan, Jörg Schmiedmayer, and Jian-Wei Pan. Demonstration of a stable atom-photon entanglement source for quantum repeaters. *Phys. Rev. Lett.*, 99:180505, Nov 2007.

[82] I. V. Inlek, C. Crocker, M. Lichtman, K. Sosnova, and C. Monroe. Multispecies trapped-ion node for quantum networking. *Phys. Rev. Lett.*, 118:250502, Jun 2017.

[83] A. Stute, B. Casabone, P. Schindler, T. Monz, P. O. Schmidt, B. Brandstätter, T. E. Northup, and R. Blatt. Tunable ion-photon entanglement in an optical cavity. *Nature*, 485:482, May 2012.

[84] Taehyun Kim, Peter Maunz, and Jungsang Kim. Efficient collection of single photons emitted from a trapped ion into a single-mode fiber for scalable quantum-information processing. *Phys. Rev. A*, 84:063423, Dec 2011.

[85] Piotr Badziąg, Michał Horodecki, Paweł Horodecki, and Ryszard Horodecki. Local environment can enhance fidelity of quantum teleportation. *Phys. Rev. A*, 62:012311, Jun 2000.

[86] Christoph Simon and William T. M. Irvine. Robust long-distance entanglement and a loophole-free bell test with ions and photons. *Phys. Rev. Lett.*, 91:110405, Sep 2003.

[87] P. Maunz, S. Olmschenk, D. Hayes, D. N. Matsukevich, L.-M. Duan, and C. Monroe. Heralded quantum gate between remote quantum memories. *Phys. Rev. Lett.*, 102:250502, Jun 2009.

[88] C. K. Hong, Z. Y. Ou, and L. Mandel. Measurement of subpicosecond time intervals between two photons by interference. *Phys. Rev. Lett.*, 59:2044–2046, Nov 1987.

[89] Y. H. Shih and C. O. Alley. New type of einstein-podolsky-rosen-bohm experiment using pairs of light quanta produced by optical parametric down conversion. *Phys. Rev. Lett.*, 61:2921–2924, Dec 1988.

[90] T. Legero, T. Wilk, A. Kuhn, and G. Rempe. Time-resolved two-photon quantum interference. *Applied Physics B*, 77(8):797–802, Dec 2003.

[91] D. Hucul, I. V. Inlek, G. Vittorini, C. Crocker, S. Debnath, S. M. Clark, and C. Monroe. Modular entanglement of atomic qubits using photons and phonons. *Nature Physics*, 11:37 EP –, Nov 2014.

[92] Rainer Blatt and David Wineland. Entangled states of trapped atomic ions. *Nature*, 453:1008, Jun 2008.

[93] J. P. Gaebler, A. M. Meier, T. R. Tan, R. Bowler, Y. Lin, D. Hanneke, J. D. Jost, J. P. Home, E. Knill, D. Leibfried, and D. J. Wineland. Randomized benchmarking of multiqubit gates. *Phys. Rev. Lett.*, 108:260503, Jun 2012.

[94] C. J. Ballance, T. P. Harty, N. M. Linke, M. A. Sepiol, and D. M. Lucas. High-fidelity quantum logic gates using trapped-ion hyperfine qubits. *Phys. Rev. Lett.*, 117:060504, Aug 2016.

[95] P. Maunz, D. L. Moehring, S. Olmschenk, K. C. Younge, D. N. Matsukevich, and C. Monroe. Quantum interference of photon pairs from two remote trapped atomic ions. *Nature Physics*, 3:538, Jun 2007.

[96] C. Monroe, D. M. Meekhof, B. E. King, S. R. Jefferts, W. M. Itano, D. J. Wineland, and P. Gould. Resolved-sideband raman cooling of a bound atom to the 3d zero-point energy. *Phys. Rev. Lett.*, 75:4011–4014, Nov 1995.

[97] Peter C. Humphreys, Norbert Kalb, Jaco P. J. Morits, Raymond N. Schouten, Raymond F. L. Vermeulen, Daniel J. Twitchen, Matthew Markham, and Ronald Hanson. Deterministic delivery of remote entanglement on a quantum network. *Nature*, 558(7709):268–273, 2018.

[98] P. O. Schmidt, T. Rosenband, C. Langer, W. M. Itano, J. C. Bergquist, and D. J. Wineland. Spectroscopy using quantum logic. *Science*, 309(5735):749–752, 2005.

[99] Y. Lin, J. P. Gaebler, T. R. Tan, R. Bowler, J. D. Jost, D. Leibfried, and D. J. Wineland. Sympathetic electromagnetically-induced-transparency laser cooling of motional modes in an ion chain. *Phys. Rev. Lett.*, 110:153002, Apr 2013.

[100] J. D. Siverns, X. Li, and Q. Quraishi. Ion–photon entanglement and quantum frequency conversion with trapped ba+ ions. *Appl. Opt.*, 56(3):B222–B230, Jan 2017.

[101] T. R. Tan, J. P. Gaebler, Y. Lin, Y. Wan, R. Bowler, D. Leibfried, and D. J. Wineland. Multi-element logic gates for trapped-ion qubits. *Nature*, 528:380, Dec 2015.

[102] C. Raab, J. Bolle, H. Oberst, J. Eschner, F. Schmidt-Kaler, and R. Blatt. Diode laser spectrometer at 493 nm for single trapped ba+ ions. *Applied Physics B*, 67(6):683–688, Dec 1998.

[103] A. V. Steele, L. R. Churchill, P. F. Griffin, and M. S. Chapman. Photoionization and photoelectric loading of barium ion traps. *Phys. Rev. A*, 75:053404, May 2007.

[104] M. R. Dietrich, N. Kurz, T. Noel, G. Shu, and B. B. Blinov. Hyperfine and optical barium ion qubits. *Phys. Rev. A*, 81:052328, May 2010.

[105] Carolyn Auchter, Chen-Kuan Chou, Thomas W. Noel, and Boris B. Blinov. Ion photon entanglement and bell inequality violation with 138ba+. *J. Opt. Soc. Am. B*, 31(7):1568–1572, Jul 2014.

[106] M. R. Dietrich, A. Avril, R. Bowler, N. Kurz, J. S. Salacka, G. Shu, and B. B. Blinov. Barium ions for quantum computation. *AIP Conference Proceedings*, 1114(1):25–30, 2009.

[107] L. Slodička, G. Hétet, S. Gerber, M. Hennrich, and R. Blatt. Electromagnetically induced transparency from a single atom in free space. *Phys. Rev. Lett.*, 105:153604, Oct 2010.

[108] K. Beloy, A. Derevianko, V. A. Dzuba, G. T. Howell, B. B. Blinov, and E. N. Fortson. Nuclear magnetic octupole moment and the hyperfine structure of the $5D_{3/2,5/2}$ states of the ba^+ ion. *Phys. Rev. A*, 77:052503, May 2008.

[109] Antonio Schiabel and Claudio Boffito. Process for the sorption of residual gas by means by a non-evaporated barium getter alloy, 1991. US Patent 5,312,607.

[110] David Hucul, Justin E. Christensen, Eric R. Hudson, and Wesley C. Campbell. Spectroscopy of a synthetic trapped ion qubit. *Phys. Rev. Lett.*, 119:100501, Sep 2017.

[111] S. De, U. Dammalapati, K. Jungmann, and L. Willmann. Magneto-optical trapping of barium. *Phys. Rev. A*, 79:041402, Apr 2009.

[112] Sebastian Gerber. *Quantum Correlation Experiments with Resonance Fluorescence Photons of single Barium Ions.* PhD thesis, Leopold-Franzens-Universitat Innsbruck, 2010.

[113] Giovanna Morigi, Jürgen Eschner, and Christoph H. Keitel. Ground state laser cooling using electromagnetically induced transparency. *Phys. Rev. Lett.*, 85:4458–4461, Nov 2000.

[114] C. F. Roos, D. Leibfried, A. Mundt, F. Schmidt-Kaler, J. Eschner, and R. Blatt. Experimental demonstration of ground state laser cooling with electromagnetically induced transparency. *Phys. Rev. Lett.*, 85:5547–5550, Dec 2000.

[115] L. Slodička, G. Hétet, N. Röck, S. Gerber, P. Schindler, M. Kumph, M. Hennrich, and R. Blatt. Interferometric thermometry of a single sub-doppler-cooled atom. *Phys. Rev. A*, 85:043401, Apr 2012.

[116] N. Yu, W. Nagourney, and H. Dehmelt. Radiative lifetime measurement of the ba^+ metastable $d_{3/2}$ state. *Phys. Rev. Lett.*, 78:4898–4901, Jun 1997.

[117] J. I. Cirac, P. Zoller, H. J. Kimble, and H. Mabuchi. Quantum state transfer and entanglement distribution among distant nodes in a quantum network. *Phys. Rev. Lett.*, 78:3221–3224, Apr 1997.

[118] Stephan Ritter, Christian Nölleke, Carolin Hahn, Andreas Reiserer, Andreas Neuzner, Manuel Uphoff, Martin Mücke, Eden Figueroa, Joerg Bochmann, and Gerhard Rempe. An elementary quantum network of single atoms in optical cavities. *Nature*, 484:195 EP –, Apr 2012. Article.

[119] M. J. Madsen, D. L. Moehring, P. Maunz, R. N. Kohn, L.-M. Duan, and C. Monroe. Ultrafast coherent excitation of a trapped ion qubit for fast gates and photon frequency qubits. *Phys. Rev. Lett.*, 97:040505, Jul 2006.

[120] B. B. Blinov, D. L. Moehring, L.-M. Duan, and C. Monroe. Observation of entanglement between a single trapped atom and a single photon. *Nature*, 428:153 EP –, Mar 2004.

[121] D. L. Moehring, M. J. Madsen, K. C. Younge, Jr. R. N. Kohn, P. Maunz, L.-M. Duan, C. Monroe, and B. B. Blinov. Quantum networking with photons and trapped atoms (invited). *J. Opt. Soc. Am. B*, 24(2):300–315, Feb 2007.

[122] D B Higginbottom, L Slodička, G Araneda, L Lachman, R Filip, M Hennrich, and R Blatt. Pure single photons from a trapped atom source. *New Journal of Physics*, 18(9):093038, 2016.

[123] H. Inamori, N. Lütkenhaus, and D. Mayers. Unconditional security of practical quantum key distribution. *The European Physical Journal D*, 41(3):599, Jan 2007.

[124] Nicolas Sangouard, Christoph Simon, Hugues de Riedmatten, and Nicolas Gisin. Quantum repeaters based on atomic ensembles and linear optics. *Rev. Mod. Phys.*, 83:33–80, Mar 2011.

[125] André Stefanov, Nicolas Gisin, Olivier Guinnard, Laurent Guinnard, and Hugo Zbinden. Optical quantum random number generator. *Journal of Modern Optics*, 47(4):595–598, 2000.

[126] C. Monroe. Quantum information processing with atoms and photons. *Nature*, 416:238 EP –, Mar 2002.

[127] K. Sosnova, C. Crocker, M. Lichtman, A. Carter, S. Scarano, and C. Monroe. Trapped ion single-photon emitter for quantum networking. In *Frontiers in Optics / Laser Science*, page FW7A.5. Optical Society of America, 2018.

[128] Lucas Schweickert, Klaus D. Jöns, Katharina D. Zeuner, Saimon Filipe Covre da Silva, Huiying Huang, Thomas Lettner, Marcus Reindl, Julien Zichi, Rinaldo Trotta, Armando Rastelli, and Val Zwiller. On-demand generation of background-free single photons from a solid-state source. *Applied Physics Letters*, 112(9):093106, 2018.

[129] T. D. Ladd, F. Jelezko, R. Laflamme, Y. Nakamura, C. Monroe, and J. L. O'Brien. Quantum computers. *Nature*, 464:45, Mar 2010. Review Article.

[130] Connor Kupchak, Philip J. Bustard, Khabat Heshami, Jennifer Erskine, Michael Spanner, Duncan G. England, and Benjamin J. Sussman. Time-bin-to-polarization conversion of ultrafast photonic qubits. *Phys. Rev. A*, 96:053812, Nov 2017.

[131] Xun-Li Feng, Zhi-Ming Zhang, Xiang-Dong Li, Shang-Qing Gong, and Zhi-Zhan Xu. Entangling distant atoms by interference of polarized photons. *Phys. Rev. Lett.*, 90:217902, May 2003.

[132] David Lucas. (private communication).

[133] L. Luo, D. Hayes, T.A. Manning, D.N. Matsukevich, P. Maunz, S. Olmschenk, J.D. Sterk, and C. Monroe. Protocols and techniques for a scalable atom–photon quantum network. *Fortschritte der Physik*, 57(11-12):1133–1152.

[134] Earl T. Campbell and Simon C. Benjamin. Measurement-based entanglement under conditions of extreme photon loss. *Phys. Rev. Lett.*, 101:130502, Sep 2008.

[135] N. Kalb, A. A. Reiserer, P. C. Humphreys, J. J. W. Bakermans, S. J. Kamerling, N. H. Nickerson, S. C. Benjamin, D. J. Twitchen, M. Markham, and R. Hanson. Entanglement distillation between solid-state quantum network nodes. *Science*, 356(6341):928–932, 2017.

[136] Charles H. Bennett, David P. DiVincenzo, John A. Smolin, and William K. Wootters. Mixed-state entanglement and quantum error correction. *Phys. Rev. A*, 54:3824–3851, Nov 1996.

[137] I. V. Inlek, G. Vittorini, D. Hucul, C. Crocker, and C. Monroe. Quantum gates with phase stability over space and time. *Phys. Rev. A*, 90:042316, Oct 2014.

[138] G. Vittorini, D. Hucul, I. V. Inlek, C. Crocker, and C. Monroe. Entanglement of distinguishable quantum memories. *Phys. Rev. A*, 90:040302, Oct 2014.